PH.D. IN ASTRONOMY, ASTROPHYSICS AND SPACE SCIENCE

CYCLE XXXII

Dynamics of Stars and Planets in the Super Dense Central Galactic Region

Nazanin Davari
A.Y. 2018/2019

Supervisor: **Prof. Roberto Capuzzo Dolcetta**

Coordinator: **Prof. Paolo De Bernardis**

Deputy Coordinator: **Prof. Nicola Vittorio**

Abstract

There is observational evidence that a compact massive object (CMO) of about four million solar masses cloaks at the heart of the Milky Way (MW), known as Sgr A*. The gravitational tidal field of this CMO (probably a Supermassive black hole, SMBH) is extremely strong so that binary star passing in its vicinity are likely stripped apart. One component of the binary can be hurled swiftly out of the Galactic Centre, or even the MW, as Hypervelocity Star (HVS) and its twin could be seized on an eccentric orbit revolving around the central massive object, similar to the observed S-stars (Hills mechanism).

Given that many binary star systems are acknowledged to host planets, we intend in this thesis deepening the study of the violent dynamics of binary stars and their planetary systems with the Sgr A* massive object, highlighting the resulting fraction of HVS hosting planet.

In the first part of this thesis, we focus on tight binary stars with one planet for each component of the binary, and investigate the fate of the four-body system after the interaction with the SMBH. Results are achieved by means of a high precision, regularized, numerical integrator suitable for those large mass ratios which are involved in the interaction of SMBH and stars/planets. Furthermore, in order to develop the investigation of dynamics in the proximity of Sgr A*, we model the environment of the Galactic Centre (GC) by applying the local distribution of stars in the form of a regular external potential which also generates dynamical friction on the approaching objects. The Galaxy density profile, is represented in spherical symmetry as the sum of a Dehnen and a Plummer distribution for the galactic background and the nuclear star cluster (NSC) around the GC, respectively. After setting proper initial conditions for our chosen set of binary stars hosting one planet each, we carried out integrations taking into account the gravity field of the massive object in the post-Newtonian approximation up to 2.5 order.

This allows us to evaluate the likelihood of ejection and capture of the four-body system in its interaction with Sgr A* emphasizing mainly on the fate of the planets initially bound to the binary star.

Our simulations show that after the interplay between four-body system and the SMBH, the result is that of giving rise to lonely hypervelocity stars (HVSs) or S-stars and, also, to HVSs or S-stars that

would keep their planets. Furthermore, it is possible to spectate rogue hypervelocity planets (HVP) thrown out of the Galaxy or starless planets (S-planets) revolving around the SMBH in independent eccentric orbits similar to those of S-stars. Stars and/or planets can be, also, devoured by the SMBH. Here, "devoured" means that a star or planet enters inside $3R_s$ i.e. within the innermost stable circular orbit (ISCO) of the non-rotating SMBH. We show that both starless S-planets and S-stars with planets can exist around the SMBH on high eccentric ($e \sim 0.97$) orbits similar to the G2 cloud orbital eccentricity.

Eventually, in this thesis we focus on the dynamical evolution and stability of populous planetary systems in the vicinity of Sgr A*. The S-star cluster, which is a dynamically relaxed dense cluster of stars and consists of roughly 40 stars, inhabits in the centre of the Galaxy. Spectroscopic analysis of the S-stars reveals the existence of both a population of early- and late-type stars on tightly eccentric orbits, with different orientations and semi-major axes. These stars are believed to be the captured companions of the HVSs in the binary-SMBH disruption. Accordingly, they might have formed elsewhere and migrated to the GC, probably hosting planetary systems. The existence of planets or planetary systems in the vicinity of Sgr A* is still an open argument. Our aim is to investigate the destiny of their putative planetary systems after close interaction with the central black hole of our Galaxy.

We run simulations for the 40 stars of this cluster for which the orbital parameters are known from the literature. For the sake of simplicity, the planetary systems assigned to each of the stars of this cluster are similar to our Solar planetary system in mass, eccentricity and semi-major axis. Our simulations show that the innermost planets are more likely to remain bound to their host stars until the end of the simulation. However, we show that starless Jupiter-like planets can be found in orbits similar to the G1 cloud as semi-major axis and eccentricity. In addition, a small fraction of starless Uranus-like planets can revolve Sgr A* in a way consistent with the G1 cloud as semi-major axis and inclination.

Acknowledgements

This thesis would not have been possible without continuous and unparalleled love, help and encouragement of my family. I am especially grateful to my parents, who supported me emotionally and encouraging me in all of my pursuits to explore new directions in life and seek my own destiny. I am forever thankful to my beloved brother for always being there for me as a friend and inspiring me to follow my dreams.

I owe my deepest gratitude to my supervisor Professor Roberto Capuzzo Dolcetta for his tolerance, kindness and support. Without his positive encouragement and motivation, this thesis could not have been achieved. I express my warmest gratitude to my associate supervisor Professor Rainer Spurzem for his hospitality and guidance during my visit to Heidelberg. I had the opportunity to work with him only for four months, but I have been influenced significantly by his advice and optimistic counselling style.

I am deeply thankful to Fernanda Lupinacci for her help and warm welcoming when I arrived in Rome. I am grateful to my friends and colleagues Sara, Diego, Stefano, Riccardo and all my friends in the Pi room for their friendship and for creating a cordial working environment and for making my stay in Italy memorable. I would like to show my appreciation to my friend and colleague Dr Manuel Arca-Sedda and his lovely wife, Martina, for their advice and help both when I started my PhD in Rome and during my stay in Heidelberg and to all my friends and colleagues in the Astronomisches Rechen-Institut in Heidelberg.

Contents

List of Figures

List of Tables

Chapter 1

Structure of galactic nuclei

1.1 Compact massive objects in galactic nuclei

Detection of distant, high luminous, extragalactic radio sources coming from extremely compact dimensions in the early 1960s, was the beginning of supermassive black holes (SMBHs) story (Schmidt, 1963). These radio sources had been known as quasi-stellar objects or quasars and in fact, represented the existence of enormous masses in relatively small volume (Greenstein & Schmidt, 1964). These tremendous emissions from such remote objects were believed to be related to infall of matter towards the centre and growth of a massive object and subsequent conversion of gravitational energy into radiation (Salpeter, 1964; Rees, 1984). It is now determined that quasars are the Active Galactic Nuclei (AGN) and many, if not all, massive galaxies could undergo these phenomena in their centres or at least have experienced a violently AGN phase during their lifetime.

Lynden-Bell (1969); Lynden-Bell & Rees (1971) hypothesised that a quasar-like object dwells at the centre of the local group of galaxies, associated with the total energy output, identifies as a "dead" quasar or a central massive black hole like the one in the centre of the Milky Way (MW) which may once have been the site of energetic processes.

A striking number of high-resolution observations brought forth improvements in enlightenment of galactic nuclei including indirect pieces of evidence for inhabitance of high masses of dark and very compact objects, i.e. most likely SMBHs, whose masses are between 10^6 and 10^9 $\mathrm{M}_\odot$, in the centres of many, if not all, bright galaxies (Ferrarese et al., 2006; Kormendy & Bender, 2009; Nayakshin et al., 2012). AGN statistics present the existence of SMBHs in all galaxy types (Kauffmann et al., 2003) even very massive ones with $M_{SMBH} \geq 10^9$ $\mathrm{M}_\odot$ at high redshifts ($z \geq 7$) when the universe was at its infancy only $\leq 5\%$ of its present age (e.g. Mortlock et al. (2011)). The study of X-ray variability in AGNs probes the structure and physical processes that occur in the innermost regions of the accretion flow and can be turned to account for verifying the spin of black holes (e.g. Reynolds (2014)).

Discoveries yield to a tight connection between the galaxy evolution and the SMBH growth which lurks at its core (Ferrarese et al., 2006; Kormendy & Ho, 2013). The correlation between SMBH mass and the velocity dispersion (σ) of its host spheroid, referred to the so-called "$M_\bullet - \sigma$ relation" ($M_\bullet$ indicates M_{SMBH}), has been studied by many authors. There are strong empirical correlations between the masses of SMBHs and the bulge (M_b) in the case of spirals, or the entire galaxy in the case of ellipticals (Alexander, 2017). The stellar velocity dispersion σ in the bulge (outside the region influenced by the SMBH) correlates with the SMBH mass as $M_{SMBH} = M_0(\sigma/\sigma_0)^\beta$, with $\beta \sim 4 - 5$ (Ferrarese & Merritt, 2000; Gebhardt et al., 2000). The SMBH's mass scales with the bulge's mass M_b as $M_{SMBH} = \epsilon_\bullet M_b$, with $\epsilon_\bullet \sim (1-2) \times 10^{-3}$ (Magorrian et al., 1998; Häring & Rix, 2004; Alexander, 2017). The distinction between classical and pseudo-bulges[1] is important. Kormendy & Ho (2013) argue that classical bulges and ellipticals correlate closely with $M_\bullet$, but SMBHs do not correlate tightly enough with pseudo-bulges to imply close coevolution. Pseudo-bulge SMBHs generally deviate by having smaller masses than the scatter of points in the correlations for classical bulges and ellipticals (see Figure 1.1). This motivates the suggestion that there are two different modes of SMBH feeding for classical and pseudo-bulges.

After all, even if a perfect correlation were set up between SMBH mass and spheroid mass in the early universe, it is hard to see how it could survive galaxy mergers, which convert discs to bulges and may also channel gas into the nucleus, producing (presumably) uncorrelated changes in M_{SMBH} and M_b (Merritt, 2013). In order to preserve a close connection between M_{SMBH} and σ or M_{SMBH} and M_b (with properties on scales much larger than SMBH's direct dynamical influence), some sort of "negative feedback" by the powerful outflows in the SMBH's AGN phase would seem to be required, allowing the SMBH to regulate its own growth (King & Pounds, 2015). Since SMBHs acquired most of their mass via accretion of gas, the radiation field from an accreting quasar must drive a wind from the vicinity of the SMBH, which would collide with the ambient gas in the galaxy and produce shocks. Perhaps an outflow driven by the accretion could be the source of the feedback. In this picture, the SMBH would eventually reach a mass such that further accretion is prevented because the outflow sweeps away the ambient gas (Merritt, 2013).

Over the last decades, Hubble Space Telescope (HST) observations have revealed that massive, yet compact, stellar clusters, often referred to as "Nuclear star clusters" (NSCs), exist at the centres of many, maybe even most, galaxies across the Hubble sequence. These NSCs have been detected in $\sim 75\%$ of all galaxies and appear as compact clusters at the photometric and dynamical centres of their host galaxies (Carollo et al., 1998; Böker, 2002; Côté et al., 2006; Neumayer et al., 2011). A

---

[1] Kormendy & Kennicutt (2004) review observations which show that some central galaxy components that are used to identify as classical bulges have properties that are more disc than those of classical bulges and are, made not by galaxy mergers but by slow ("secular") evolution internal to isolated galaxy discs. Pseudo-bulges may be augmented by minor mergers (Kormendy & Ho, 2013).

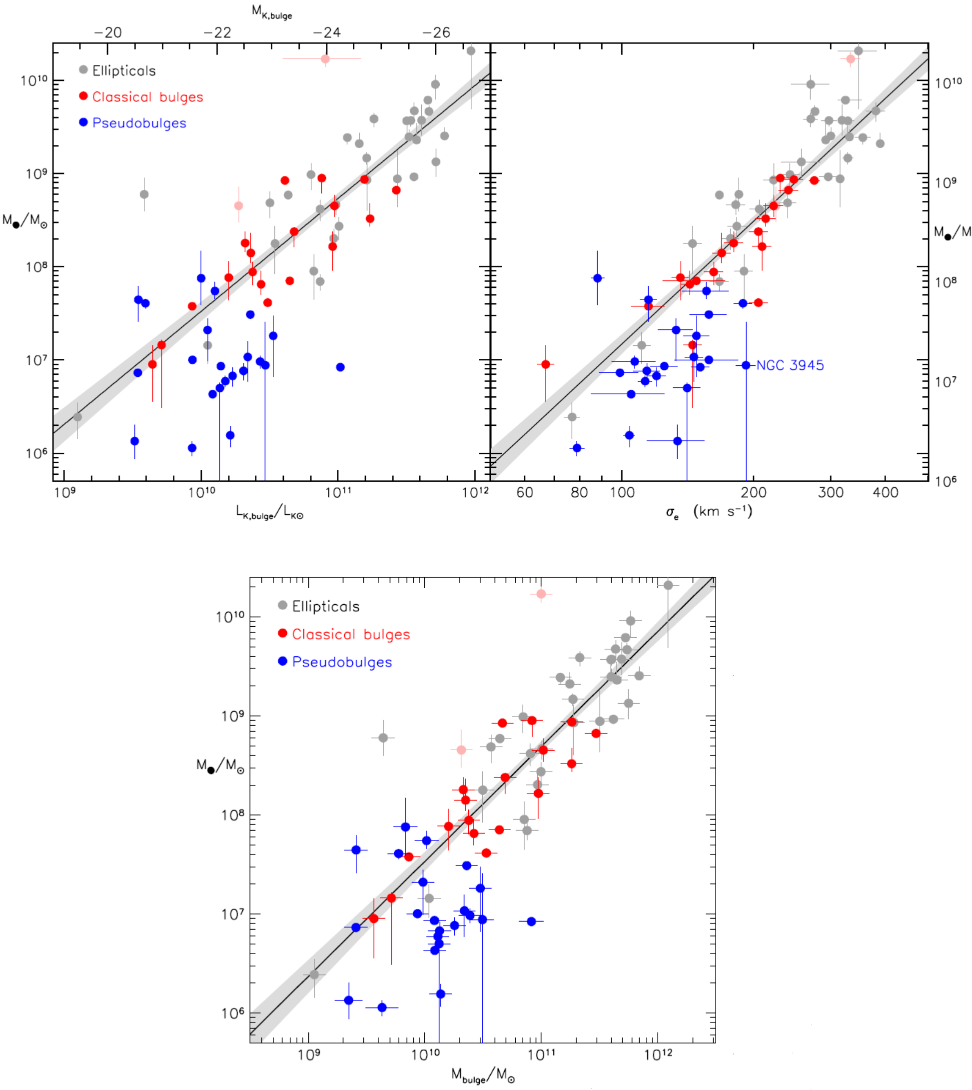

Figure 1.1: SMBH correlations including (blue points) pseudo-bulges with dynamical SMBH masses. Ellipticals are plotted in gray because the emphasis is on the contrast between classical and pseudo-bulges. In all panels, pseudo-bulge SMBHs are offset toward smaller $M_\bullet$ from the correlations for classical bulges and ellipticals (from Fig. 21 Kormendy & Ho (2013)).

collection of recent data indicates that NSCs are present in 75% of late-type spirals (Scd-Sm), 50% of earlier type sp (Sa-Sc), and 70% of spheroidal (E and S0) galaxies (Capuzzo-Dolcetta, 2016). NSCs are massive and compact stellar systems, with masses in the $10^6 - 10^7$ $M_\odot$ range and half-light radii of 1-5 parsecs (Böker et al., 2004; Côté et al., 2006; Arca-Sedda & Capuzzo-Dolcetta, 2019), about four magnitudes brighter than globular clusters. Their small sizes and large masses make them the densest stellar systems in the Universe (Neumayer, 2012).

Ferrarese et al. (2006) discovered that the correlation between NSC mass (M_{NSC}) and velocity dispersion of the host galaxy ($M_{NSC}-\sigma$) is analogous to the $M_\bullet-\sigma$ relation (middle panel of Figure 1.2) suggesting a single mechanism responsible for the growth and perhaps the formation of both NSCs and SMBHs. Ferrarese et al. (2006) suggested that SMBHs and NSCs should be grouped together under the terminology, "Central Massive Object" (CMO), and constrained the slope of the $M_{CMO} - M_{gal}$ relation to be unity leads to a constant ratio between CMO and galaxy mass $M_{CMO} - M_{gal} \approx 0.18\%$ a conclusion also reached, based on photometric data only, by Côté et al. (2006); Wehner & Harris (2006).

Although NSCs scaling relations differ significantly from those of SMBHs (Scott & Graham, 2013; Erwin & Gadotti, 2012; Capuzzo-Dolcetta & Tosta e Melo, 2017), nevertheless these determinations suggest that NSCs and SMBHs likely form following different path (Arca Sedda et al., 2019).The presence of an NSC in the heart of a galaxy is not an inevitable obligation for the occupancy of an SMBH; NSCs with no detectable SMBHs are observed in lower mass galaxies ($\leq 10^{10}$ $M_\odot$), while the nucleus of very massive galaxies ($\geq 10^{12}$ $M_\odot$) is completely dominated by the SMBH (Arca-Sedda & Capuzzo-Dolcetta, 2014a; Alexander, 2017). In an intermadiate mass range ($10^8 - 10^{10}$ $M_\odot$), some nuclei (including our Milky Way, see 1.2.2) host both an SMBH and an NSC (Seth et al., 2008; Graham, 2012; Georgiev et al., 2016).

The NSCs contain both an old ($\geq$ 1 Gyr) and a young ($\leq$ 100 Myr) stellar population (Capuzzo-Dolcetta, 2016). This indicates that NSCs did not form in a single event, but that instead, they had additional star formation long after the oldest stars formed (Rossa et al., 2006). One scenario refers to the so-called (dissipational) "in-situ" model which signify an injection of gas in the central region of a galaxy hosting a "seed" BH that results in the formation of an NSC if the typical crossing time of the parental galaxy is shorter than the so-called Salpeter time, which is the time-scale over which the central BH can grow by accretion (Nayakshin et al., 2009). The other mechanism, the "dry-merger" model (dissipationless), implements the dynamical friction (df) procedure involving massive globular clusters sink towards the centre of the host galaxy (Tremaine et al., 1975; Pesce et al., 1992; Capuzzo-Dolcetta, 1993). Their subsequent merging leads to a superstar cluster with characteristics indistinguishable from those of an NSC (Capuzzo-Dolcetta & Miocchi, 2008a,b). To distinguish which mechanism is responsible for the NSCs formation is a complicated task; some studies are in agreement

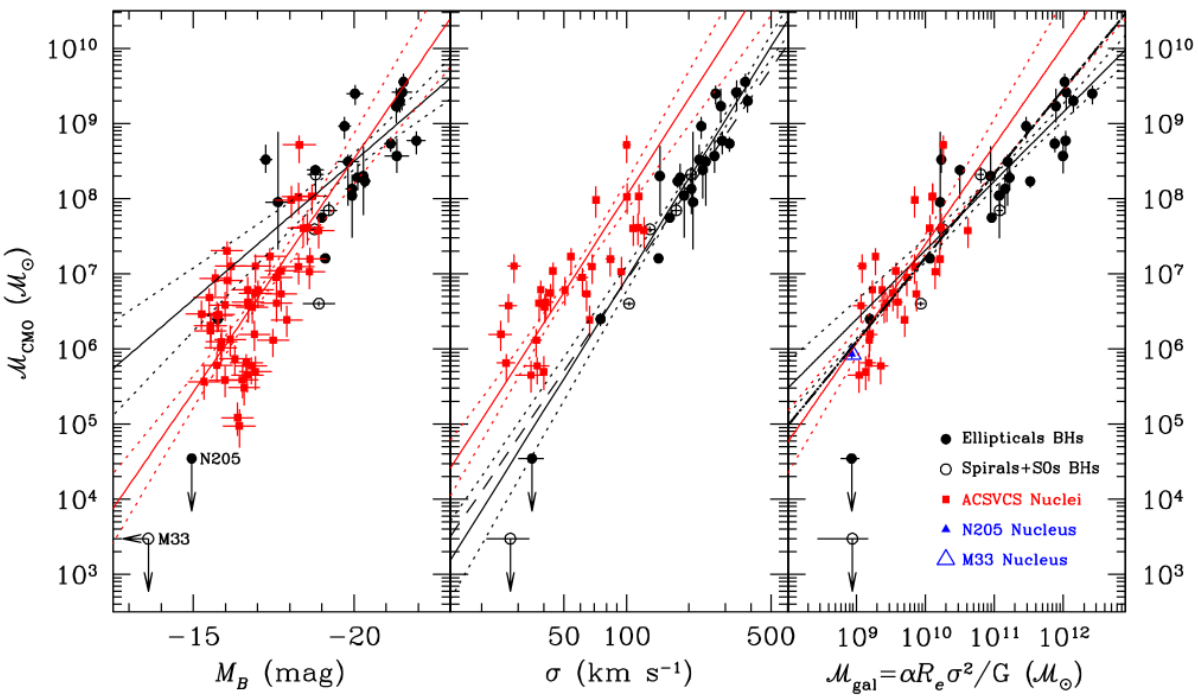

Figure 1.2: Left panel: Mass of the central massive object (CMO) plotted against absolute blue magnitude of the host galaxy (or bulge for spiral galaxies). Middle Panel: CMO mass as a function of velocity dispersion of the host galaxy measured within the effective radius R_e. Right Panel: CMO mass plotted against galaxy mass, defined as $M_{gal} \equiv \alpha R_e \sigma^2/G$ with $\alpha = 5$. Red squares show nuclei from the Virgo Cluster (ACSVCS), solid red and black lines are the best fits to the nuclei and early-type SMBH samples respectively, with $1-\sigma$ confidence levels shown by the dotted lines. The dashed line, in the middle panel, is the best fit $M_\bullet - \sigma$ relation of Tremaine et al. (2002). The dashed line, in the right panel, is the fit obtained for the combined nuclei+SMBH sample (from Fig. 2 of Ferrarese et al. (2006)).

with the "in-situ" model while others fulfill the "dry-merger" process. Ferrarese et al. (2006) found a power law relation between the NSC mass (M_{NSC}), and the host velocity dispersion, σ, that is $M_{NSC} \propto \sigma^4$ (Arca-Sedda et al., 2016) which is reproduced fairly well by the in- situ model (Antonini, 2013) whereas the "dry-merger" scenario, has been successfully investigated both on a theoretical and numerical side (Capuzzo-Dolcetta & Miocchi, 2008a,b; Antonini et al., 2012; Antonini, 2013; Arca-Sedda & Capuzzo-Dolcetta, 2014a), and explains satisfactorily the observed correlations among NSCs properties and those of their host galaxies (Arca-Sedda & Capuzzo-Dolcetta, 2014b; Leigh et al., 2012; Scott & Graham, 2013).

In addition, the absence of a dense central stellar cusp [2] in the galactic nuclei does not necessarily indicate the absence of an SMBH (Alexander, 2017). One explanation is that stellar mass was removed from a previously existing cusp due to former galaxy mergers resulted in a tight SMBH binary. Eventually, creation of the present SMBH required the merger of SMBH binary by ejecting the stellar mass, vacating galactic nucleus and leaving behind a lower-density stellar core (Begelman et al., 1980; Milosavljević et al., 2002; Alexander, 2017).

1.2 The Galactic Center

The Galactic centre (GC) is a unique environment to explore the extreme processes that occur near a supermassive black hole (SMBH). In fact, the GC hosts the only concentration of mass ($\sim 4 \times 10^6$ $M_\odot$) that can be determined with an SMBH beyond reasonable doubt (Schödel et al., 2002; Ghez et al., 2003). Additionally, its distance from our Sun ($\approx$ 8 kpc) is several orders of magnitude smaller than the distance from the other SMBH candidates which, despite its hostility, makes it an ideal laboratory to investigate physical processes. In this section, I concisely discuss the main constituents of the GC: Sgr A*, the nuclear star cluster (NSC), the inner disc(s), the S-star cluster and the mysterious G-clouds (see Genzel et al. (2010); Mapelli & Gualandris (2016) for a review).

1.2.1 Sgr A* compact object

Sagittarius A* (Sgr A*) exposed itself first time as a compact radio source, coming from the innermost parsec, using radio interferometry method (Balick & Brown, 1974). The existence of a compact, massive object (CMO) in the GC was already detected by early infrared observations (e.g. Sanders & Lowinger (1972)). However, the first dynamical evidence for existence of a concentrated mass at the Galactic nucleus was the discovery of an ionized gas orbiting the central parsec of the MW when

---

[2] A cusp is a density distribution that formally diverges at $r \to 0$ e.g. a power-law $\rho(r) \propto r^{-\alpha}$ with $\alpha > 0$. A cored density distribution flattens to a finite central density inside the core radius (Alexander, 2017).

its motion has been revealed to be dominated by the gravitational potential of a massive core at the Galactic Centre (Wollman et al., 1977). The first attempts to estimate the mass enclosed in the central parsec are radial velocity measurements of the ionized gas (Lacy et al., 1980) although the radial velocity of ionized gas may be affected by a superabundance of processes besides gravity (Mapelli & Gualandris, 2016). Thus, radial velocity measurements of stars achieved via near-infrared spectra of the stellar population in the central parsecs in the early 90's were the first strong assertion for a dark mass in the centre of the MW (e.g. McGinn et al. (1989); Sellgren et al. (1990)). Specifically, for the star S2 a complete orbit, with a period of only 16 yr, is available and the measurement of its orbit is the conclusive testimony behind the SMBH hypothesis (e.g. Schödel et al. (2002); Gillessen et al. (2017)) (see section 1.2.4). From uninterrupted monitoring of stellar orbits in the Galactic Center, Gillessen et al. (2017) determined the central mass and the distance to it as $4.28 \pm 0.10|_{stat} \pm 0.21|_{sys} \times 10^6$ $M_\odot$ and $8.32 \pm 0.07|_{stat} \pm 0.14|_{sys}$ kpc. This value comes from a joint fit of New Technology Telescope (NTT), Very Large Telescope (VLT) and Keck astrometric data ranging from 1992 to 2017 (Mapelli & Gualandris, 2016).

On the other hand, the possible past activity of the SMBH in our GC is still an enigma. One may wonder whether Sgr A* has always been so underluminous or if it experienced, in the past, long periods of high energy activity, that would make the SMBH of our Galaxy more similar, than it appears today, to typical low-luminosity active galactic nuclei (AGNs) (Ponti et al., 2010). The GC black hole is most of the time in a "quasi-steady" state, mainly emitting flux of $\sim 10^{36} erg/s$ at radio to submillimeter wavelengths (e.g. Falcke et al. (1998); Yusef-Zadeh et al. (2006)). The steady emission is well described by synchrotron radiation from a thermal distribution of relativistic electrons (Genzel et al., 2010).

The other powerful trace for a past activity is exhibition of "variable" emission in the X-ray and infrared bands (e.g. Sunyaev et al. (1993)). One plausible explanation is that this lines are emitted by various molecular clouds in the GC (e.g. Ponti et al. (2010)). If the lines radiated from different clouds, they might be triggered by several separate sources (e.g. different X-ray binaries), but this possibility is not supported by observations of currently active X-ray sources (Mapelli & Gualandris, 2016). Some of this variable emission, especially at X-rays, appears as "flares", typically a few times per day and lasting for about 10^2 minutes. Flares release an additional luminosity of up to another $10^{36} erg/s$ and the "variable" emission and the flares might have been originated from transiently heated electrons (Genzel et al., 2010). Due to the fact that a single source must have been strong enough to generate such radiation, one possible origin of this X-ray emission could be the "echo" of an energetic flaring event of Sgr A* that happened several hundreds years ago (Mapelli & Gualandris, 2016), such as the tidal disruption of a star or of a smaller body (e.g. Koyama et al. (1996); Yu et al. (2011)). The "echo" scenario suggests that Sgr A*'s luminosity must have been a few 10^5 times higher a few hundred years ago (e.g. Muno et al. (2007); Ponti et al. (2010); Genzel et al. (2010)).

Another potential alternative for the Sgr A*'s past flare could be the recently reported young magnetar SGR J1745-2900 (Rea et al., 2013) which is on a bound orbit around the SMBH (Mapelli & Gualandris, 2016).

1.2.2 The Nuclear Star Cluster

The concentration of the (both young and old) stars in the central few parsecs is often referred to as the nuclear star cluster (NSC) of the MW. NSCs are located at the photometric and dynamical centre of almost all spiral galaxies (e.g. Côté et al. (2006); Mapelli & Gualandris (2016)), but the NSC of the MW is the only object of this class that can be resolved into individual stars (Genzel et al., 2003; Schödel et al., 2007, 2009, 2010). Due to the extreme interstellar extinction towards the GC, which also weaken the infrared fluxes, the GC is not detectable in the visible band but the radio, sub-millimeter, mid-infrared, near-infrared, and X-ray light can all penetrate through the dust and uncover incidents occurring at this fascinating part of our Galaxy. However, the near-infrared regime is a sweet spot for studying the gravitational potential in the GC (Gillessen et al., 2017).

On the early observations of the GC, using near-infrared wavelengths, Becklin & Neugebauer (1968) and Becklin et al. (1982) detected a quite large number of bright stars, environed the radio source Sgr A*. Afterwards, from higher-resolution imaging spectroscopy of the entire central core of the MW, Eckart et al. (1993) and Genzel et al. (1996) found out the stellar surface density is very well fitted by an isothermal cluster model, scales as $\rho(r) \propto r^{-2}$, with a core radius of 0.3-0.5 pc and is close to $\sim 10^7 - 10^8$ M$_\odot$ pc^{-3}. The first estimation for the mass of the NSC was $\sim 3 \pm 1.5 \times 10^7$ M$_\odot$ (Launhardt et al., 2002) with the half light radius of 3-5 pc (Schödel, 2011). Using data from *Spitzer*/IRAC at 3.6 and 4.5 μm, where interstellar extinction is at a minimum but the overall emission is still dominated by stars, Schödel et al. (2014) derived a total mass of $\sim 2.5 \pm 0.4 \times 10^7$ M$_\odot$ and a half light radius of 4.2 ± 0.4 pc.

Even though observations of the GC needed to be performed in the near-infrared band, to achieve an accurate evaluating of the observational evidence, a high angular resolution was also needed to overcome the extreme source crowding which is a result of the high stellar density of the NSC.

Surprisingly, no observational evidence could clarify whether the NSC of the MW displays a core or a cusp density profile around the central black hole (Gallego-Cano et al., 2018). The presence of a central massive black hole within an NSC should lead to the formation of a cusp surrounding the massive black hole with an approximately $\rho(r) \propto r^{-7/4}$ density profile in single–mass models (Bahcall & Wolf, 1976). Combining the high-resolution stellar number counts from NACO[3] H- and K- band

---

[3] The adaptive optics module NAOS and the NIR camera CONICA (abbreviated as NACO) are mounted at the ESO 8m-class VLT unit telescope 4 on Cerro Paranal, Chile (Mapelli & Gualandris, 2016).

imaging data of the very central region (0.004–0.4 pc), with lower resolution number counts from speckle imaging observations at $0.4 \leq r/pc \leq 4$ (where r is the projected distance from Sgr A*), Genzel et al. (2003) indicated the existence of a stellar cusp which is best-fitted by a broken power-law

$$\rho(r) = 1.2 \times 10^6 M_\odot pc^{-3} \left(\frac{r}{0.4pc}\right)^{-\alpha} \tag{1.1}$$

with $\alpha = 1.4 \pm 0.1$ and 2.0 ± 0.1 for $r < 0.4$ pc and $r > 0.4$ pc, respectively. This result was later updated by Schödel et al. (2007) with a power-law of

$$\rho(r) = 2.8 \pm 1.3 \times 10^6 M_\odot pc^{-3} \left(\frac{r}{0.24pc}\right)^{-\alpha} \tag{1.2}$$

with $\alpha = 1.2$ and 1.75 for $r < 0.24$ pc and $r > 0.24$ pc, respectively (Mapelli & Gualandris, 2016). Nonetheless, it was later realised that the star counts within about 0.5 pc of Sgr A* were contaminated by a significant number of young, and therefore dynamically unrelaxed, stars (Gallego-Cano et al., 2018). When omitting the young stars, the projected stellar density of giants appears almost flat, core-like, within a few 0.1 pc of Sgr A* (Buchholz et al., 2009; Do et al., 2009; Bartko et al., 2010).

Thus, observations of the stellar surface brightness from old stars appeared to indicate a possibly core-like structure (Fritz et al., 2016). These results yielded to the missing cusp problem (Gallego-Cano et al., 2018). Dozens of theoretical papers, sought to explain this deficit of old, bright red giant stars. Merritt et al. (2010) explains that in the absence of a cusp, the time for a 10 $M_\odot$ black hole to spiral in to the Galactic center from an initial distance of 5 pc can be much greater than 10 Gyr while a core of initial radius 1–1.5 pc evolves to a size of approximately 0.5 pc after 10 Gyr, roughly the size of the observed core. Possible mechanisms for the creation of the parsec-scale initial core include destruction of stars on centrophilic orbits in a pre–existing triaxial nucleus, inhibited star formation near the SMBH, or ejection of starsby a massive binary (Merritt et al., 2010). Amaro-Seoane & Chen (2014) postulate that the reason for the missing stars in the red giant branch (RGB) is closely intertwined with the disc formation process, which initially was gaseous and went through a fragmentation phase to form the stars. Therefore, during fragmentation the disc developed regions with densities much higher than a homogeneous gaseous disc, i.e., "clumps", which were optically thick, and hence shrank slowly. Stars in the GC interacted with them and in the case of RGB stars, the clumps were dense enough to totally remove their outer envelopes after a relatively low number of impacts. The missing stars in the RGB in the natural context of the star–forming disc that after fragmentation led to the currently observed stellar disc in our GC (Amaro-Seoane & Chen, 2014).

More recent observations of Schödel et al. (2009); Schödel et al. (2017); Gallego-Cano et al. (2018) proved the presence of a cusp. Eventually, Gallego-Cano et al. (2018) revisited the question of the stellar cusp around the SMBH and selected adaptive optics assisted high angular resolution images obtained with the NACO instrument at the ESO VLT and aligned each pointing of the NACO mosaic with a reference frame created from positions measured in Hubble Space Telescope (HST) Wide Field Camera 3 observations of the same field (see Figure 1.3). From what is known about the star formation history of the NSC according to Pfuhl et al. (2011): the average nuclear star formation rate dropped from an initial maximum ∼ 10 Gyr ago to a deep minimum 1-2 Gyr ago and increased again during the last few hundred Myrs (200-300 Myr) and roughly 80% of the stellar mass formed more than 5 Gyr ago, and that mass estimates within R ∼ 1 pc from Sgr A* favor a dominant star formation mode with a "normal" Chabrier/Kroupa initial mass function for the majority of the past star formation in the GC (see Figure 1.4). Since the old stellar component is estimated to be the dominant mass of the NSC in our Galaxy, Gallego-Cano et al. (2018) excluded young, and therefore dynamically not relaxed stars from the analysis (omitted the region $R \leq 1$" (0.04 pc)) and just looked into the old ($>$ 1 Gyr), low-mass stellar component, which is expected to be dynamically relaxed.

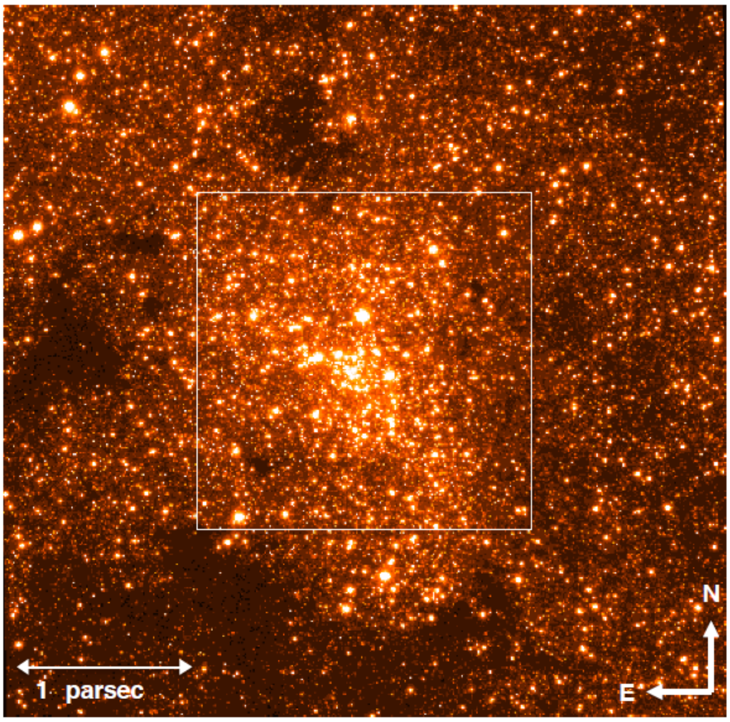

Figure 1.3: Wide-field mosaic the observations from 11th May 2011. The field-of-view is $1.5' \times 1.5'$. The field of about 40" × 40" that corresponds to the deep imaging data is marked by a white square (from Fig. 6 Gallego-Cano et al. (2018))

Gallego-Cano et al. (2018) presented a 3D Nuker model (Lauer et al., 1995) defined as

$$\rho(r) = \rho_b(r_b) 2^{(\beta-\gamma)/\alpha} \left(\frac{r}{r_b}\right)^{-\gamma} \left[1 + \left(\frac{r}{r_b}\right)^{\alpha}\right]^{(\gamma-\beta)/\alpha} \tag{1.3}$$

where r is the 3D distance from Sgr A*, r_b is the break radius, ρ is the 3D density, γ is the exponent of the inner and β the one of the outer power-law, and α defines the sharpness of the transition. With $\alpha = 1$, $r_b = 3.0 \pm 0.4$ pc, $\gamma = 1.29 \pm 0.02$ and $\beta = 2.1 \pm 0.1$, that provides a good description of the cluster structure. The best fit according to the Nuker model is shown in Figure 1.5.

1.2.3 The inner disc(s)

The presence of young massive stars in the central parsec of the MW has been investigated for a long time (Lacy et al., 1982; Rieke & Rieke, 1989; Allen et al., 1990). So far more than a hundred of these young massive stars have been observed in the vicinity of Sgr A* which many of them are O-type and Wolf-Rayet (WR) stars (Genzel et al., 1994, 2003; Paumard et al., 2006; Bartko et al., 2009) (see Fig. 1.6).

Via spectroscopy techniques radial velocity and spectral type of these stars could carefully be understood, while proper motions and brightness have been provided by photometry. The most recent spectroscopic data include observations with the integral field spectrograph SINFONI (Bartko et al., 2009) at the ESO/VLT, and with the OH-Suppressing Infrared Imaging Spectrograph (OSIRIS) at the Keck II telescope (Do et al., 2013). The most recent photometric data include observations with NACO at the ESO/VLT (Trippe et al., 2008; Bartko et al., 2009) and with NIRC2 at the Keck II telescope (Do et al., 2013).

The radial velocities of these massive early-type stars are mostly blue-shifted north, and red-shifted south of Sgr A*, exactly opposite to the rotation of the MW and the old stars in the NSC (Genzel et al., 1996, 2000; Tanner et al., 2006). In the late 1990s, it became clear that most of the bright early-type stars in the central few arcseconds show a **clockwise** motion pattern ($j_z > 0$)[4] on the sky, consistent with an inclined disc in Keplerian rotation around Sgr A* (Genzel et al., 2000). The young ages (4-6 Myr) of these stars and their observed low eccentricities ($e = 0.2 - 0.3$, (Bartko et al., 2009; Lu et al., 2013)) probably favor an in-situ formation in a dense gas accretion disc that can overcome the SMBH tidal forces (e.g. Levin (2006a); Alexander et al. (2008b,a); Bonnell & Rice (2008)). Besides, some bright stars in a **counter-clockwise** motion ($j_z < 0$) have been detected, as well (Bartko et al., 2009).

---

[4] $j_z = (x\ v_y - y\ v_x)/(\{x^2 + y^2\}\{v_x^2 + v_y^2\})^{1/2}$ is the projected, normalized specific angular momentum of the motion on the sky. If $j_z > 0$ the motion is clockwise, and if $j_z < 0$ it is counter-clockwise (Genzel et al., 2000).

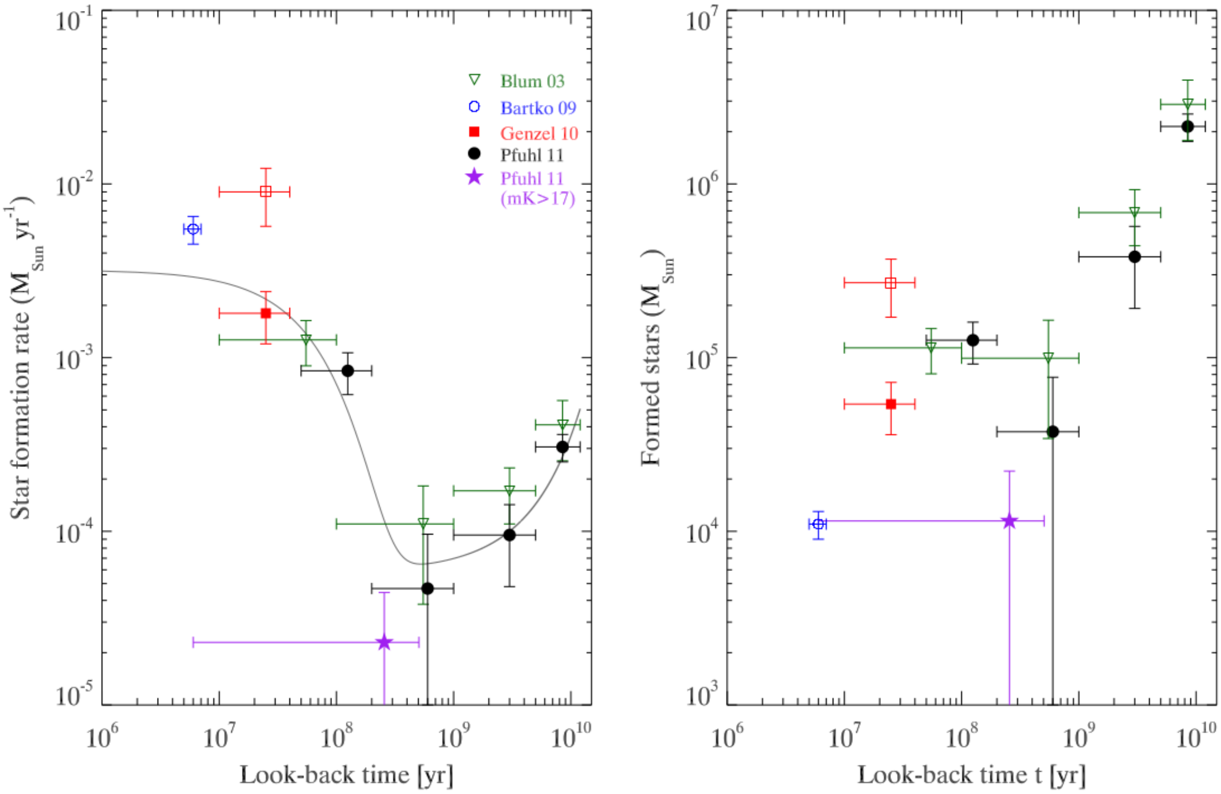

Figure 1.4: Left-hand panel: star formation rate of the Galactic Centre as a function of time. The black circles represent the best fit to the H-R diagram with a Chabrier/Kroupa IMF. The mass error is given by the 1σ error of the fit. The age error is simply the width of the age bin. The star formation history derived by (Blum et al., 2003) (green triangles), by (Genzel et al., 2010) for red supergiants within 1 pc (red filled square) and within 2.5 pc (red square) and by (Bartko et al., 2009) for the stellar discs (blue circle) are indicated for comparison. The star symbol (purple) indicates the recent star formation rate inferred by the early-to-late ratio of faint GC stars (Section 6.1.1 Pfuhl et al. (2011)). The solid gray line shows a simple exponential model of star formation as a function of time. Right-hand panel: the total mass formed in each age bin is shown. Although star formation occurred at a high rate during the last few hundred Myrs, the total mass contribution is lass than 10%. The bulk of the stellar mass formed more than 5 Gyr ago (from Fig. 14 Pfuhl et al. (2011)).

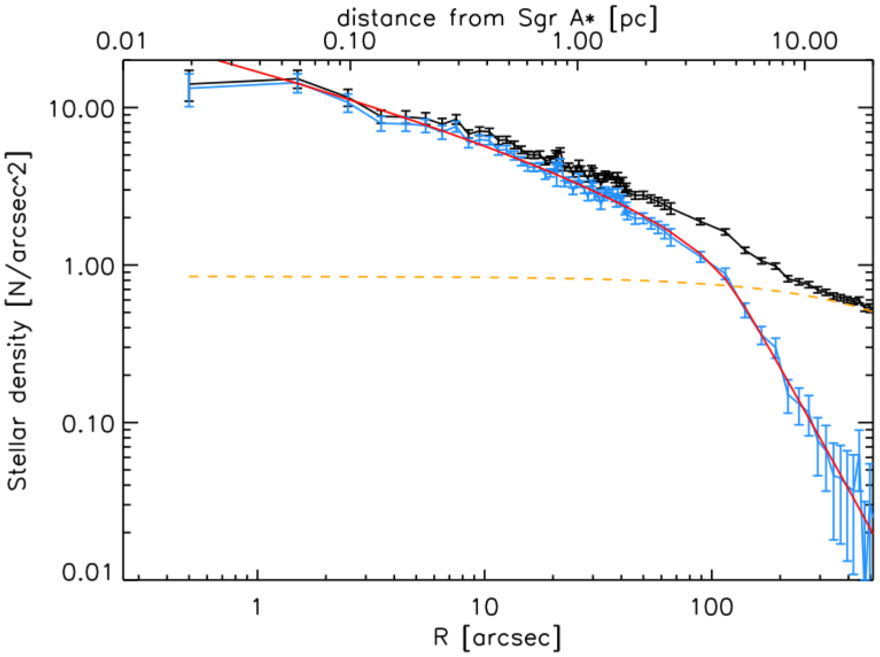

Figure 1.5: The red line is a Nuker model fit. Black: combined, corrected surface density data for stars in the magnitude range $17.5 \leq K_s \leq 18.5$. The dashed orange line is a model for the emission from the nuclear disc that is subtracted from the black data points, resulting in the blue data points (from Fig. 14 Gallego-Cano et al. (2018)).

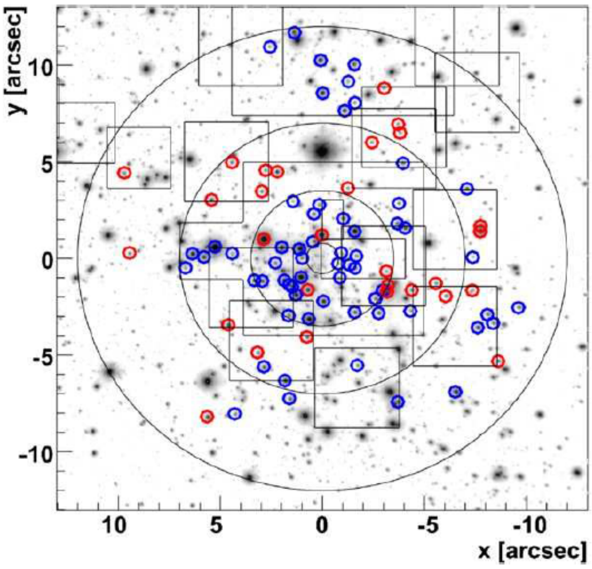

Figure 1.6: Sample of 90 O/WR stars ($m_K < 14$ and $\Delta(v_z) \leq 100kms^{-1}$) in the central 0.5 pc of our Galaxy: blue circles indicate CW orbits (61 O/WR stars) and red circles indicate counterclockwise orbits (29 O/WR stars). The black circles show projected distances of 0.8", 3.5", 7", and 12" from Sgr A*. Squares indicate the exposed fields with SINFONI in the 25 mas pixel^{-1} and 100 mas pixel^{-1} scale. The whole inner 0.5 pc region is contained in lower resolution (250 mas pixel^{-1} scale) SINFONI observations (Paumard et al., 2006) (from Figure. 1 of Bartko et al. (2009)).

More analysis of orbital angular momentum directions shows that some of these early-type stars lie in a ”disc” (Paumard et al., 2006; Bartko et al., 2009; Lu et al., 2009; Yelda et al., 2012; Do et al., 2013; Lu et al., 2013). Thus, this disc is called **clockwise (CW) disc** (Mapelli & Gualandris, 2016). In fact, the fraction of early-type stars that belong to the CW disc is still debated. The analysis of Bartko et al. (2009) for 90 O/WR stars shows that ∼ 50% of the young massive stars belong to the CW disc is extended up to 0.5 pc and is warped or tilted, since the orientation of its normal axis changes by 60° from the inner edge to the outer edge. Furthermore, Bartko et al. (2009) discover that the CW disc is mildly eccentric, with a mean eccentricity of $e = 0.36 \pm 0.06$.

However, new kinematic measurements by Yelda et al. (2014), which improved the precision of the accelerations in the plane of the sky, were in conflict with the presence of the claimed counterclockwise disc. Yelda et al. (2014) have analysed the orbits of 116 young stars in the GC between projected radii R=0.8”–13” (∼ 0.032–0.52 pc) and with marginal significance confirmed again the existence of the CW disc, which has an orbital plane oriented at (i, Ω) = (130°, 96°). They showed that the true disc fraction of young stars is ∼ 20%, a factor of ∼ 2.5 lower than previous estimates, suggesting that what is currently observed as the CW disc may be the remnant of what used to be a more densely populated stellar disc. The similarity in the kinematic properties of the B stars and the O/WR stars suggests a common star formation event. Yelda et al. (2014) verified that the intrinsic eccentricity distribution of the disc stars is unimodal, with an average value of e = 0.27 ± 0.07, which can be achieved through dynamical relaxation in an initially circular disc with a moderately top-heavy mass function.

Thus, the hypothesis of a secondary, counterclockwise disc is still disputed. Theoretical studies, on the other hand, confirm the need of a second disc to clarify current configuration of O/WR stars in the central cluster (Genzel et al., 2010). Using N-body simulations, Cuadra et al. (2008) conclude that neither the evolution of one disc nor the known perturbers within the central parsec (such as stellar or intermediate mass black holes) cannot be sufficient to describe the existing distribution of O/WR stars. In order to grow eccentricities and inclinations more rapidly, a large perturbing potential due to a second disc might be required (Nayakshin et al., 2006). Nayakshin (2005) and Nayakshin et al. (2006) have noted that the interaction between two discs or rings of stars induces mutual orbital precession and thickens initially thin discs over time. Nayakshin et al. (2006) determine that two discs of mass a few 10^3 to 10^4 $M_\bullet$ induce then a thickness of $h_z/R \sim 0.1$ over 4-6 Myr. Nayakshin et al. (2006) results are consistent with the observed values of 10^4 $M_\bullet$ and 5×10^3 $M_\bullet$ for the clockwise and counterclockwise systems (Bartko et al., 2009). Moreover, Löckmann et al. (2009) point out the large range of orbital orientations and warping of the O/WR stars observed by Lu et al. (2009); Bartko et al. (2009) can be best described by the interaction between two discs rather than evolution of one single, initially very thin circular disc over 6 Myr.

Additionally, the presence of three O/WR binaries in the inner 0.2 pc of the Galactic centre is now approved (Ott et al., 1999; Martins et al., 2006; Rafelski et al., 2007; Pfuhl et al., 2014). The first confirmed binary (IRS 16SW) is an equal-mass binary (50 $M_\odot$) at a projected distance estimated as ~ 0.05 pc with a period of 19.5 days (Ott et al., 1999; Martins et al., 2006; Rafelski et al., 2007). Pfuhl et al. (2014) discovered two additional binaries, an eclipsing Wolf-Rayet binary with a period of 2.3 days, and a long-period binary with an eccentricity of 0.3 and a period of 224 days. Both of these binaries are estimated to be at only ~ 0.1 pc from the SMBH. Apart from these three confirmed binaries in the CW disc, few other binary candidates might exist (Pfuhl et al., 2014). Using radial velocity change upper limits, Pfuhl et al. (2014) estimate a spectroscopic binary fraction in the GC of $f_{SB} = 0.30^{+0.34}_{-0.21}$, broadly consistent with the massive binary fraction observed in dense young clusters.

1.2.4 The S-star cluster

The population of a few stars whose orbits are (totally or partially) inside the innermost arcsecond of the GC (~ 0.04 pc or 1") are referred to as the S-star cluster (Eckart & Genzel, 1996; Schödel et al., 2002, 2003; Ghez et al., 2003; Genzel et al., 2003; Eisenhauer et al., 2005; Gillessen et al., 2009, 2017). The naming of the 'S'-stars originated in Eckart & Genzel (1996) to denote those remarkably fast moving stars in the 'Sgr A*(IR)-cluster' that were known at that time (Genzel et al., 2010) (apparently, "S" stands simply for "(infrared) source" (Merritt, 2013)). Figure. 1.7 displays within the central 1 arcsec^2 of the Galaxy[5].

Contrary to the stars of the CW disc, S-stars seem to be fainter ($m_K = 14 - 17$) and probably lower mass stars (Habibi et al., 2017) with high-eccentric and randomly oriented orbits. They are so close to the central black hole that by tracking their individual orbits around Sgr A*, one can collect information on the gravitational potential in which they move. Thus, the key to determine the central mass and the distance to is tracing the orbit of these stars (Gillessen et al., 2009, 2017). The S-stars are spatially isotropically distributed, and the orientation of their orbits is consistent with a thermal distribution (Schödel et al., 2003; Gillessen et al., 2009, 2017). It is highly unlikely that the S-stars formed at their present location since the SMBH's tidal forces are too strong to allow star formation at these distances.

To date, the number of known stellar orbits around Sgr A* has been updated to around 40, which 8 stars out of these 40 belong to the CW disc (Gillessen et al., 2017). Figure 1.8 shows the distribution of the angular momentum vectors for the 40 orbits. Eight of the orbits have an orientation that is compatible with the clockwise stellar disc (Bartko et al., 2009; Yelda et al., 2014) at (Ω=104°, i =

---

[5] Unfortunately, two similar, but slightly different, labeling conventions are in use for these stars. A group centered in the Max-Planck-Institut für extraterrestrische Physik near Munich, Germany uses *Sn*, with *n* a numeral; a group centered in Los Angeles, California prefers *S0-n* (Merritt, 2013).

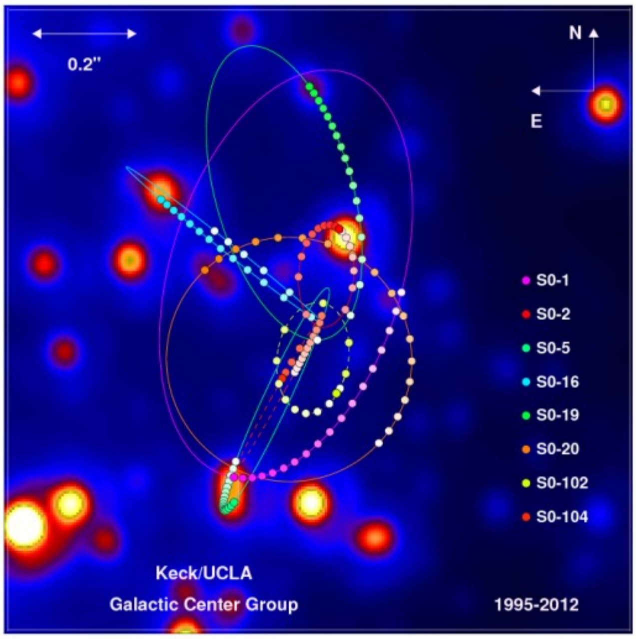

Figure 1.7: The orbits of stars within the central 1" × 1" arcseconds of our Galaxy. These orbits provide the best evidence yet for a supermassive black hole. While every star in this image has been observed to move since 1998, estimates of orbital parameters are best constrained for stars that have been observed through at least one turning point of their orbits. (Credit: UCLA research team from the data sets obtained with the W.M. Keck Telescope.)

126°); the same six stars as in Gillessen et al. (2009), S66, S67, S83, S87, S96, and S97, plus the stars S91 and R44 (Gillessen et al., 2017).

The star S2 (the brightest star of the S-star cluster) continues to yield the best constraints on the mass of and distance to Sgr A* (Gillessen et al., 2017). Using the data from S2's closest approach to the SMBH, Gravity Collaboration et al. (2018) have reported the first direct detection of the first-order parameterised post-Newtonian correction terms (PPN(1)), due to Special and General Relativity. Over the past 26 years, Gravity Collaboration et al. (2018) have monitored the radial velocity and motion on the sky of S2, mainly with the SINFONI and NACO adaptive optics instruments on the ESO/VLT, and since 2016 and leading up to the pericentre approach in May 2018, with the four-telescope interferometric beam-combiner instrument GRAVITY. From data up to and including pericentre, Gravity Collaboration et al. (2018) robustly detect the combined gravitational redshift and relativistic transverse Doppler effect for S2 of $z = \Delta\lambda/\lambda \approx 200\ kms^{-1}/c$ with different statistical analysis methods. Gravity Collaboration et al. (2018) showed that the data from S2 are inconsistent with pure Newtonian dynamics and the S2 star pericentre passage fulfills the predictions of general relativity when the gravitational redshift and the relativistic Doppler effect are taken into account. Habibi et al. (2017) analysed the result of 12 years of high resolution spectroscopy within the central arcsecond of the GC. Habibi et al. (2017) have obtained high signal to noise H- and K-band spectra

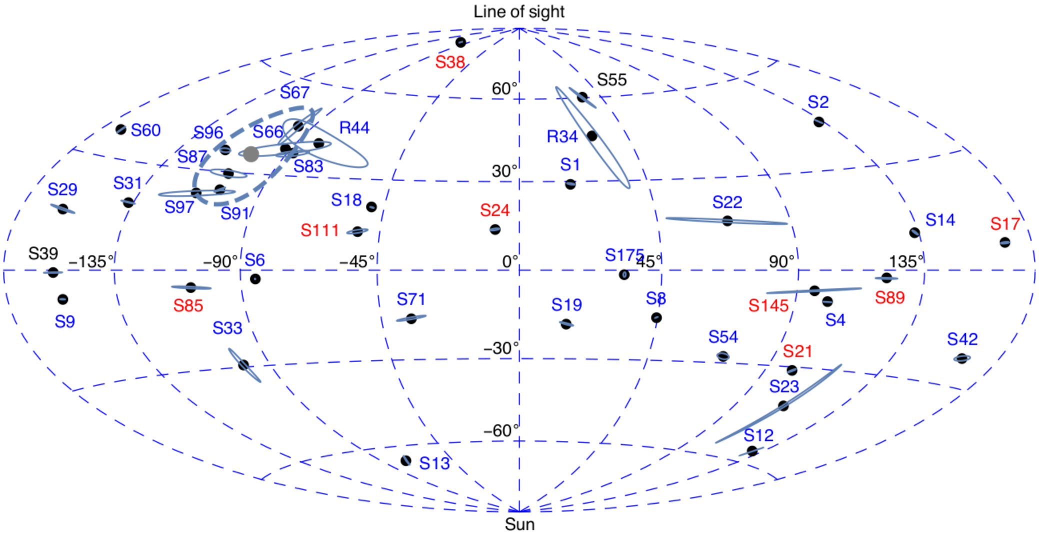

Figure 1.8: Orientation of the orbital planes of those S-stars. The vertical dimension corresponds to the inclination i of the orbit and the horizontal dimension to the longitude of the ascending node Ω. The color of the labels indicates the stellar type (blue for early-type stars, red for late-type stars). The stars S66, S67, S83, S87, S91, S96, S97 and R44 are members of the CW disc (Bartko et al., 2009; Yelda et al., 2014) at $(\Omega = 104°, i = 126°)$ marked by the thick grey dot and the dashed line, indicating a disc thickness of 16°. A star in a face-on, clockwise orbit relative to the line of sight, for instance, would be located at the top of the graph, while a star with an edge-on seen orbit would be located on the equator of the plot (From Fig. 12 of Gillessen et al. (2017)).

of eight stars orbiting the central supermassive black hole. Using deep H-band spectra, showing that these stars must be high surface gravity (dwarf) stars. These analysis reveals an effective temperature of 21000-28500 K, a rotational velocity of 60-170 kms^{-1}, and a surface gravity of 4.1–4.2. These parameters imply a spectral type of B0-B3V for these stars. The inferred masses lie within 8–14 $M_{\odot}$. Habibi et al. (2017) derived an age of $6.6^{+3.4}_{4.7}$ Myr for the star S2, which is compatible with the age of the clockwise rotating young stellar disc in the GC. The estimated age of all other studied S-stars is less than 15 Myr, which are compatible with the age of S2 within the uncertainties.

In a recent study, Habibi et al. (2019) identified new late-type stars, including the first five warm giants (G2-G8III), within the central arcsecond^2 (0.04×0.04 pc^2) of the Galaxy. Habibi et al. (2019) findings increases the number of late-type stars to 21, of which they presented deep spectra for 16. The updated star count, based on individual spectral classification, is used to reconstruct the surface density profile of giant stars. Assuming a metallicity of Z=1.5 $Z_{\odot}$, they measure an initial-mass range of 0.5–2 $M_{\odot}$ and radii of 4–30 $R_{\odot}$ for these late-type stars. Habibi et al. (2019) find a cusp structure for the spectroscopically identified old ($>$ 3 Gyr) giant stars ($m_K < 17$) within 0.25–10 arcsecond of the GC. This cusp is described by a single power law with an exponent $\Gamma = 0.34 \pm 0.04$. Their study provides the first spectroscopic detection of a cusp of giant stars toward the central arcsecond in agreement with the recent studies that found a cusp profile of fainter giants outside the central arcsecond out to 2 pc from the Sgr A* (Baumgardt et al., 2018; Gallego-Cano et al., 2018; Schödel et al., 2018).

In addition, S0-27 has been suggested to be the first potential binary in the S-star population (Jia et al., 2019). The periodic feature on the proper motion makes S0-27 a potential binary candidate.

The paradox of youth in the S-star cluster

The S-star cluster is one of the most mysterious members of the GC. There are $\sim$ 200 young, massive stars in the the central parsec of the Galaxy where is one of the richest ”massive star formation regions” in the entire MW. The young stars in the S-star cluster follow orbits that are nearly random in orientation and that have an approximately ”thermal” distribution of eccentricities, $N(< e) \sim e^2$ (Merritt et al., 2009). If there is indeed a central black hole associated with Sgr A* the provenance of such young stars very close to it is an enigmatic puzzle due to the strong tidal shear from the SMBH (Ghez et al., 2003). This is the so called ”paradox of youth” (Ghez et al., 2003). Various scenarios have been proposed to solve the ”paradox of youth” and to explain the formation of the early-type stars that orbit within the central parsec. These scenarios can be divided in two families: (i) ”in-situ” formation models, which assume local star formation by some non standard process, and the (ii) migration models, which assume formation at larger distances from the SMBH followed by fast migration to their current location (Mapelli & Gualandris, 2016).

The SMBH of the GC is expected to prevent star formation in its vicinity by disrupting any nearby molecular clouds. This is due to the fact that gravitational collapse occurrence in the presence of the tidal shear from the SMBH, requires gas clouds denser than the critical "Roche" density (Mapelli & Gualandris, 2016),

$$n_{Roche} \sim 10^7 cm^{-3} \left(\frac{M_{SMBH}}{3 \times 10^6 M_\odot} \right) \left(\frac{pc}{r} \right)^3, \tag{1.4}$$

which for $M_{SMBH} = 4.3 \times 10^6$ $\mathrm{M}_\odot$ and the distance of the molecular cloud from the SMBH of r=0.1-1 pc, exceeds by several orders of magnitude the density of any gas currently observed in the central region ($\sim 10^3$ to 10^8 cm^{-3}, (Jackson et al., 1993; Christopher et al., 2005; Montero-Castaño et al., 2009)). Thus, in-situ star formation in the central parsec requires significant compression of the gas (Morris, 1993).

The most promising mechanism for presence of such stars in the immediate vicinity of Sgr A*, is the interaction of a binary star with the SMBH, which leads to the disruption of the binary, the energetic ejection of one star, and the capture of the other star on a close orbit around the SMBH (Hills, 1988). In order to be feasible, the Hills process requires a continuous reservoir of young binary stars at large radii, as well as a mechanism to scatter the binaries onto plunging orbits.

Madigan et al. (2009) identified a secular instability of eccentric stellar disc(s) around SMBHs that can propel individual orbital eccentricities to significantly higher or lower values on the order of a precession timescale. The dynamical evolution of such a disc results in several of its stars acquiring high orbital eccentricity. Binary stars on such highly eccentric orbits would get tidally disrupted by the Sgr A* black hole, possibly producing both S-stars near the black hole and high-velocity stars in the Galactic halo (Madigan et al., 2009). Perets et al. (2007) study the role of massive perturbers in deflecting stars and binaries to almost radial (loss cone) orbits, where they pass near the central massive black hole, interact with it are ultimately destroyed. Massive perturbers could be molecular clouds of different masses, in particular giant molecular clouds, open or globular stellar clusters, and perhaps also intermediate mass black holes (IMBH) (Perets et al., 2007). Hills (1988) assumed a full loss cone while Yu & Tremaine (2003) took into account the empty loss cone regime. However, the empty loss cone region for binary-SMBH interactions extends out to $>$ 100 pc because of their large tidal radius. On these large scales massive perturbers are abundant enough to dominate the relaxation processes. Relaxation by massive perturbers dominates relaxation by two-body stellar interactions only when they are massive enough to compensate for their small space densities (Perets et al., 2007).

Binary stars in the Hills' mechanism, could also be members of the stellar disc(s) of the GC that were transferred near Sgr A* by an IMBH that inspiraled into the Galactic center a few million years ago (Levin, 2006b). A young star cluster with an IMBH can form both the disc(s) and S-stars (Fujii et al., 2010). The eccentricities and inclinations of the young stars carried near the central SMBH by the resonance were a thermal and isotropic distribution, while young stars in the outer region were distributed in a disc. These distributions agree with that of S-stars and a young stellar disc (Fujii et al., 2010).

In order to deepen the evolution of the orbital eccentricities of stars deposited near Sgr A*, Perets et al. (2009) performed Newtonian N-body simulations including a dense cluster of 10 $M_{\odot}$ stellar-mass black holes, expected to accumulate near the SMBH by mass segregation. They showed that perturbations from the stellar-mass black holes randomize the stellar orbits, partially erasing the dynamical signatures of their origin. The eccentricities of the initially highly eccentric stars evolve, in 20 Myr (the S-star lifespan), to a distribution that is consistent with the observed eccentricity distribution Perets et al. (2009) but the eccentricities of the initially more circular orbits fail to evolve to the observed values in 20 Myr, arguing against the disc migration scenario of Levin (2006b); Fujii et al. (2010).

Moreover, there has been speculation that the cores of intermediate-mass stars stripped of their envelopes by tidal interaction with the SMBH in the GC (Davies & King, 2005; Dray et al., 2006). Davies & King (2005) argue that S-stars can be the remnants of low-to-intermediate mass red giants that have been scattered into near-radial orbits and tidally stripped as they approach the central black hole, making them into rather blue objects. A star stripped on the red giant branch (i.e., prehelium ignition) has a luminosity $\sim 10^2 L_{\odot}$, with an effective temperature $T_{eff} \sim 10^4$ K would not be visible in IR surveys which explains the observed depletion of red giants in the very center of the Galaxy (Davies & King, 2005).

Antonini et al. (2010); Ginsburg & Loeb (2007) showed that the observed S-stars could be the merger product of the two stars in the binary in the Hills' mechanism. Besides, Kozai–Lidov resonances (Kozai, 1962; Lidov, 1962) can induce collisions in the vicinity of the SMBH and increase the merger rate and explain B-type stars in the S-star cluster (Antonini et al., 2010). In collisions involving a low-mass and a high-mass star, the merger product acquires a high core hydrogen abundance from the smaller star. Therefore, mergers tend to rejuvenate stars, in the sense that the lower mass star sinks to the center of the merger remnant, effectively resetting the nuclear clock of the merger product to the zero-age main sequence (Antonini et al., 2011).

1.2.5 The G-clouds

In 2011, Gillessen et al. (2012) reported the presence of a dense gas cloud approximately three times the mass of Earth that is falling into the accretion zone of Sgr A*. A faint dusty object, nicknamed G2 by Burkert et al. (2012), orbiting the SMBH on a highly eccentric orbit (~ 0.98) with a pericenter radius of roughly 20 light hours ($\sim$ 2000 Schwarzschild radii) from the central massive black hole Sgr A* (Pfuhl et al., 2015). The enigma was whether this object going to be tidally disrupted by the SMBH or not.

The G2 cloud was detected as an L$'$-band continuum source, as well as a line emission source in near-IR hydrogen and helium recombination lines but a missing counterpart source in K-band (Gillessen et al., 2012; Pfuhl et al., 2015; Plewa et al., 2017). It is also seen in the spectroscopic data as a strong redshifted emission component in the Brackett-γ (Brγ) line. The object has a remarkably low temperature $\sim$ 560 K and a luminosity about five times that of Sun, unlike any star that have been so far detected near Sgr A* (Gillessen et al., 2012). The L$'$ astrometry is not consistent with Brγ astrometry and there is an apparent positional offset between the Brγ line emission and L$'$ continuum emission of G2 (Phifer et al., 2013). The Brγ line emission is elongated along its direction of motion and traces hot gas that appears to be externally heated by ionizing photons from massive stars in the vicinity of G2 (Gillessen et al., 2012; Witzel et al., 2014). In Brγ, G2 shows clear evidence of tidal interaction with the black hole (Gillessen et al., 2012, 2013a,b; Pfuhl et al., 2014). Unlike Brγ, the L$'$ emission remains spatially unresolved, continues to follow a well–defined Keplerian orbit, and is constant in brightness (Witzel et al., 2014). The L$'$ emission is much more compact than the emission in Brγ and thus originates in a different region. This is most likely explained by optically thick dust that has had constant temperature and size over the past decade and is internally heated (Witzel et al., 2014). Pfuhl et al. (2015) detected a tail emission in the Brγ and L$'$-band continuum, which seems to follow G2 in the position–velocity diagrams. It seems that the cloud G2 is actually a bright knot of a longer gas streamer since the tail follows G2 in time and is continuously connected to the head, G2 (Pfuhl et al., 2014; Gillessen et al., 2014).

The detection of G2's orbit returns to $\sim$ 2003 (Gillessen et al., 2012; Mapelli & Gualandris, 2016). The observation of a blue-shifted ($-3000kms^{-1}$) component in April 2013 indicated that a part of G2 had already passed pericentre. The bulk of G2 has transited at pericentre in Spring 2014 (see Figure 1.9), avoiding complete tidal disruption (Mapelli & Ripamonti, 2015). No apparent sign of disruption or enhancement of its L$'$ luminosity and even emission of X-ray flares was detected and the object is still point-like (Mapelli & Gualandris, 2016; Haggard, 2014). The dust continuum emission is unresolved in L$'$-band, stays consistent with the location of the Brγ emission, but the total luminosity of the Brγ and L$'$ emission has remained constant to within the measurement uncertainty (Plewa et al., 2017).

Pfuhl et al. (2015) assessed the semimajor axis and eccentricity of $a = 0.042 \pm 0.01$ pc and $e = 0.98 \pm 0.007$ for the G2 cloud. In particular, the inclination and longitude of ascending node of G2, $(i, \Omega) = (118 \pm 2°, 82 \pm 4°)$, corresponds to being almost coplanar with the early-type CW disc (Gillessen et al., 2013b): the orbit of the cloud is $\sim$ 10° tilted with respect to the most recent estimates

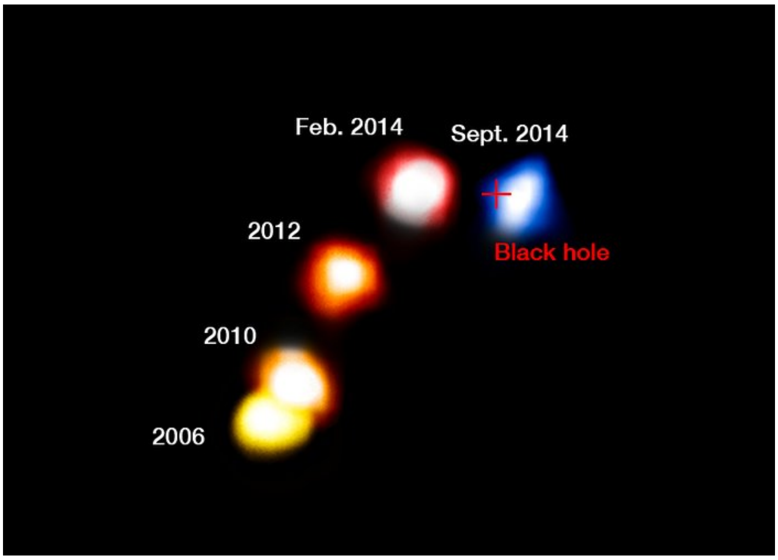

Figure 1.9: The sharpest images of the gas cloud G2, so far, showing the motion of the cloud passing the SMBH (the red cross) at the centre of the MW, and remains compact. The blobs have been colorized to show the motion of the cloud; red indicates that the object is receding and blue approaching (Credit: ESO/Andreas Eckart).

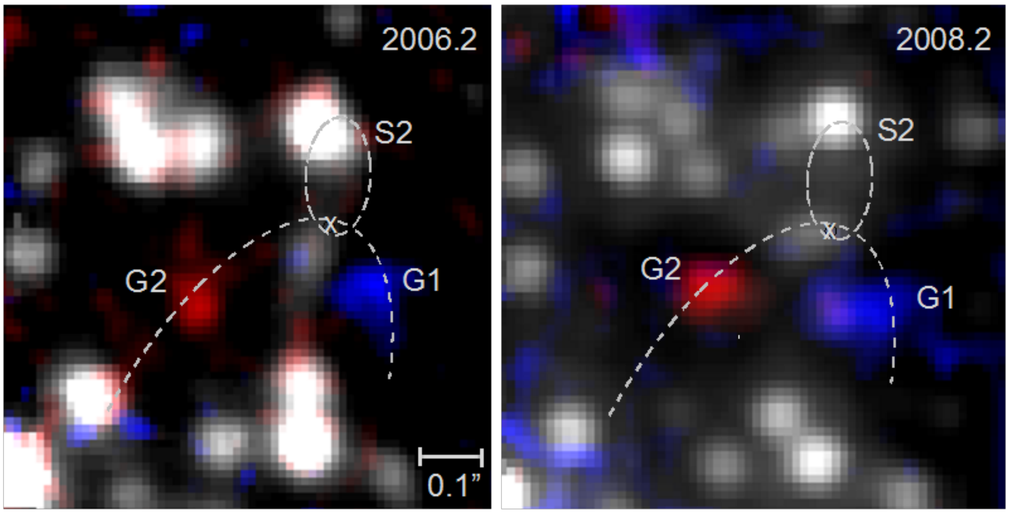

Figure 1.10: Color composites from 2006 and 2008 data sets. The red channel is centered on the velocity of the Brackett-γ line peak of G2; the blue channel on the one of G1. The grayscale background image is the continuum emission showing the S-stars. The orbits of G2 and the star S2 are shown as dashed lines, and the position of Sgr A* is marked with a cross (Pfuhl et al., 2015). The images are taken with the SINFONI instrument at the VLT (credit: Max Planck Institute for Extraterrestrial Physics (MPE)/Stefan Gillessen and his colleagues).

of the CW disc orientation ($i, \Omega = 129 \pm 18°, 98 \pm 18°$) (Mapelli & Gualandris, 2016).

Shortly after the detection of G2, another L′–band source, a dusty, ionized gas cloud of moderate mass, analogous to G2 was reported in the vicinity of Sgr A* (Pfuhl et al., 2015) (see Figure 1.10). This object, the G1 cloud, which was already observed by Clénet et al. (2005) and Ghez et al. (2005), passed its pericentre in 2001-2002 with no K–band counterpart, making it a similarly red source as G2 (Pfuhl et al., 2015). Although the orbits differ in their semimajor axes and in their eccentricities (G1 is on a smaller orbit with lower eccentricity; see Table 1.1), the orientation of the G1 orbit is very similar to the G2 orbit in all three angles. Thus, one can concludes that G1 also lies in the plane of the clockwise stellar disc the same as G2 (Pfuhl et al., 2015). Furthermore, another similarity of these two clouds lies in their total dust mass which for G1 in Ghez et al. (2005) was evaluated to be $1.3 \times 10^{-12} M_{\odot}$, and is very similar to the one estimated for G2 of $\approx 10^{-12} M_{\odot}$ (Gillessen et al., 2012).

Table 1.1: Comparison of the Orbital Elements of G1 (Pfuhl et al., 2015) and G2 (Gillessen et al., 2013b) with the orientation of the clockwise disc (CW Disc) as published by Bartko et al. (2009). a: semimajor axis in pc; e: eccentricity; i: inclination; Ω: longitude of the ascending node; ω:argument of pericentre (from Table 1 Pfuhl et al. (2015)).

	$a(pc)$	e	i	Ω	ω	Pericentre time
G2	0.042± 0.01	0.976± 0.007	$118 \pm 2°$	$82 \pm 4°$	$97 \pm 2°$	2014.25± 0.06
G1	0.0144± 0.0064	0.860± 0.050	$108 \pm 2°$	$69 \pm 5°$	$109 \pm 8°$	2001.57± 0.40
CW Disc			$129 \pm 18°$	$98 \pm 18°$		

Even though the nature of G2 is barely recognizable, the observed astrometric positions and radial velocities of G1 are compatible with the G2 orbit, assuming that about 13 yr prior to the current pericentre approach of G2, the G1 cloud went through pericentre on a similar orbit and a simple drag force model can decelerate a cloud on a G2–like orbit to an orbit that matches the G1 data (Pfuhl et al., 2015). For this reason, the G–objects could be assumed to have a joint origin.

While G2 is called ”gas cloud” in the first paper by Gillessen et al. (2012), number of other models proposed that actually there resides a (faint and undetected) star at the origin of G2 (Gillessen et al., 2014). The most fundamental difference between various models is whether or not a compact hidden source (e.g., a faint star) exists at the center of G2, which could provide a continuous source of gas supply to G2 on its orbit (Pfuhl et al., 2015; Gillessen et al., 2014). Two models have been proposed to explain the nature of G2 without a central source (or the gas cloud scenario). One of these hypotheses which could explain why G2's orbit is coplanar with the clockwise stellar disc, is that G2 might be a clump formed from the winds of massive stars in a clockwise disc of young stars (e.g. Paumard et al., 2006; Lu et al., 2009; Pfuhl et al., 2015). Accordingly, the most likely progenitor stars for that scenario is, firstly, the eclipsing binary IRS16SW (Martins et al., 2006; Gillessen et al., 2009), which consists of two $50M_{\odot}$ stars, and secondly the massive, young star S91. Both objects are part of the clockwise stellar disc, and their position on the disc is consistent with being the origin of G2 (Gillessen et al., 2014). Another possibility for the core–less scenario is that G2 could be the debris of a star that underwent a partial tidal disruption (Pfuhl et al., 2015). Guillochon et al. (2014) proposed that G2 formed out of the debris stream produced by the removal of mass from the outer envelope of a nearby giant star. Guillochon et al. (2014) investigated if tidal debris stream condenses into clumps that fall periodically onto Sgr A*, one of these clumps could be the observed G2 cloud, with the rest of the stream being detectable at lower Brγ emissivity along a trajectory that would trace from G2 to the star that was partially disrupted.

In addition, two other models have been suggested including a central source for the G objects. Since the presence of stars is ascertained close to Sgr A*, Murray-Clay & Loeb (2012) proposed that G2 might be the evaporating protoplanetary disc around a faint (young) star. Such a disc is not tidally stable at the position of G2, and hence it gets disrupted, the closer the object gets to the SMBH. The gas of the disc is then ionized by the UV radiation field of the surrounding stars and the recombination lines can be observed (Gillessen et al., 2014). The debris around a star would flag the star, which itself could be too faint to be observable, thus, this model can clearly explain the compactness of G2. Moreover, (Mapelli & Ripamonti, 2015) discussed the emission properties of rogue planets and planetary embryos in the GC. Their study shows that rogue planets can hardly be detected by current or forthcoming facilities, unless they are tidally disrupted and accreted onto the SMBH. In contrast, photoevaporation of planetary embryos might lead to a recombination rate as high as $\approx 10^{45} s^{-1}$, corresponding to a Br-γ luminosity of $\approx 10^{31} ergs^{-1}$, very similar to the observed luminosity of the dusty object G2. Apart from the population of young massive stars near Sgr A*, several lines of evidence point to on-going star formation within two parsecs of Sgr A* suggesting a population of photoevaporative protoplanetary discs associated with newly formed low mass stars (Yusef-Zadeh et al., 2015a,b, 2017). Consequently, the SMBH might capture planets or planetary embryos orbiting the young stars lie in the innermost parsec of our Galaxy and bring them onto nearly radial orbits (Mapelli & Ripamonti, 2015). One would need to speculate about planet formation in the

GC (Gillessen et al., 2014). Concerning about this and to explain the high eccentricity of G–clouds, Trani et al. (2016) studied the dynamics of hypothetical planets around stars in the CW disc and in the S-star cluster and they found the semi-major axis and eccentricity of planets escaping from the S-stars correspond to those of G1 and G2 clouds. The second model concerning a central source is that the G2 gas cloud falling in toward Sgr A* is the mass-loss envelope of a young T-Tauri star (Scoville & Burkert, 2013). A young, low mass star with a mass-loss rate $\sim 10^{-7} M_{\odot} yr^{-1}$ and a terminal wind velocity $\sim 100\ kms^{-1}$ would produce a cometary wind bubble with observational properties similar to the G2 cloud (De Colle et al., 2014).

On the other hand, observational work by Phifer et al. (2013) favors a stellar origin of G2, based, however, not on their actual data, but expressing the prior that it should be more likely to find stars around Sgr A* than gas clouds (Gillessen et al., 2014). Assuming a stellar origin for G-objects, Trani et al. (2019) explain the existence of G–objects through three–body encounters between binaries of the stellar disc and stellar black holes from a dark cusp around Sgr A*.

Chapter 2

Hypervelocity stars: from Galactic nucleus to the Galactic halo

The term ”Hypervelocity star” (HVS) is applied to describe an unbound star travel with such extreme velocities that a gravitational interaction with a massive compact object can most likely explain its origin. Theorists have proposed different possible mechanisms for expelled unbound stars observed in the halo of the Milky Way (MW). These mechanisms can be examined with larger and more complete samples such as *Gaia* Data Release 2 (DR2). In the following, I describe the importance and alternative origins of such stars as well as their difference with the Galactic Disc ”runaways”. For a detailed review of the HVSs we refer to Brown (2015).

2.1 Observation of hypervelocity stars

The most recent HVS Survey is the MMT (Multiple Mirror Telescope) survey, a spectroscopic survey of stars within the colour range of 2.5–4 $M_\odot$ late B–type stars (Brown et al., 2014; Capuzzo-Dolcetta & Fragione, 2015). The MMT observational approach is rationalised by that such stars should not exist at faint magnitudes in the outer halo unless they were ejected there. The MMT survey is complete over 29% of the sky and identifies 21 HVSs ejected from the MW at distances between 50 and 120 kpc.

The first HVS (HVS1) was discovered serendipitously by Brown et al. (2005), with an apparent radial velocity of $853{\pm}12$ kms^{-1} and a heliocentric distance of ~ 55 kpc, that could be consistent with the Galactic rest-frame velocity of ~ 709 kms^{-1}. At a galactocentric distance of 50 kpc, the mass of the Milky Way is $\sim 5 \times 10^{11}$ $M_\odot$ (Wilkinson & Evans, 1999) and the escape velocity is ~ 305 kms^{-1}. Thus, HVS1 is moving well over twice the escape velocity and in a direction 174° from the Galactic center (Brown et al., 2005). Based on its rapid rotation ($v\ sini \simeq$ 190 kms^{-1}), HVS1 is classified as a relatively short-lived 3-M$_\odot$ main-sequence B star (Brown et al., 2014; Brown, 2015).

Two other serendipitous HVS discoveries were published soon after the discovery of HVS1. Hirsch et al. (2005) discovered an unbound object, a helium-rich subdwarf O star (hereafter HVS2) in the halo of the MW with a heliocentric radial velocity of at least 720 kms^{-1}. The next one was HE 0437-5439 (hereafter, HVS3), a 16th magnitude main-sequence B-star with a heliocentric radial velocity of 723±3 kms^{-1} (Edelmann et al., 2005). HVS3 might have a Large Magellanic Cloud (LMC) origin since it is only 16° away from the LMC and much closer to the LMC (LMC; 18 kpc) than to the GC, thus it can reach its position from the center of the LMC (see section 2.4.9). But this scenario requires an ejection velocity of 1000 km s^{-1}, thus an unseen SMBH or an intermediate–mass black hole (IMBH) in the LMC (see 2.4.4) (Edelmann et al., 2005; Gualandris & Portegies Zwart, 2007; Brown, 2015). On the other hand, HVS3 has been identified as a 9 M$_\odot$ main-sequence star 50 kpc away (Bonanos et al., 2008; Przybilla et al., 2008a). The travel time from the Galactic Centre to the current location of HVS3 is 100 Myr while a 9 M$_\odot$ star will have a main–sequence lifetime $\sim$ 35 Myr (Gualandris & Portegies Zwart, 2007). Therefore, if originated from the MW centre, HVS3 should be a "blue straggler"[1] which means the progenitor was a binary system ejected from the MW at $>$ 800 km s^{-1} (see 2.4.7) (Brown, 2015).

After the discovery of HVS1, Warren Brown and his colleagues planned for a targeted observing program to detect more candidates among distant stars within the colour range of 2.5–4 M$_\odot$ B–type stars in radial velocity alone. Radial velocity surveys have not yet uncovered lower-mass HVSs and a different approach for finding unbound stars is required to combine radial velocity and proper motion (known HVSs at distances of 50–100 kpc with proper motions are too small, <1 mas yr^{-1}, to be measured with ground-based telescopes) (Brown, 2015).

However, a clean sample of HVSs is important for constraining the Galactic centre ejection mechanism. Brown et al. (2018) use *Gaia* Data Release 2 (DR2) measurements (Gaia Collaboration et al., 2018) to explore the origin of the highest velocity stars in the HVS survey. The measurements reveal a clear pattern in B-type stars. Brown et al. (2018) compare *Gaia* proper motions with previous Hubble Space Telescope (HST) measurements and evaluate the origin of unbound stars based on computed trajectories and ejection velocities. They select a gravitational potential model, trace the trajectory of each star backwards in time, and calculate the required ejection velocity from that position in the MW. The results are insensitive to the choice of the potential model because the stars are on nearly radial trajectories. Brown et al. (2018) conclude with speeds of $\simeq$ 100 kms^{-1} below Galactic escape velocity halo stars are the dominant ones in the sample. Disc runaway stars, on the other hand, have speeds up to $\simeq$ 100 kms^{-1} above Galactic escape velocity, but most disc runaways are bound. Stars

---

[1] Blue stragglers (Sandage, 1953) are main-sequence stars that lie above the turnoff region at the blue end of the colour–magnitude diagram. They appear to have abnormally long lifetimes on the main–sequence due to mass transfer.

with speeds $\gtrsim 100$ kms^{-1} above Galactic escape velocity originate from the Galactic centre (the highest velocity stars). Furthermore, they found two bound stars which might have GC origin (Figures 2.1 and 2.2 summarize their results).

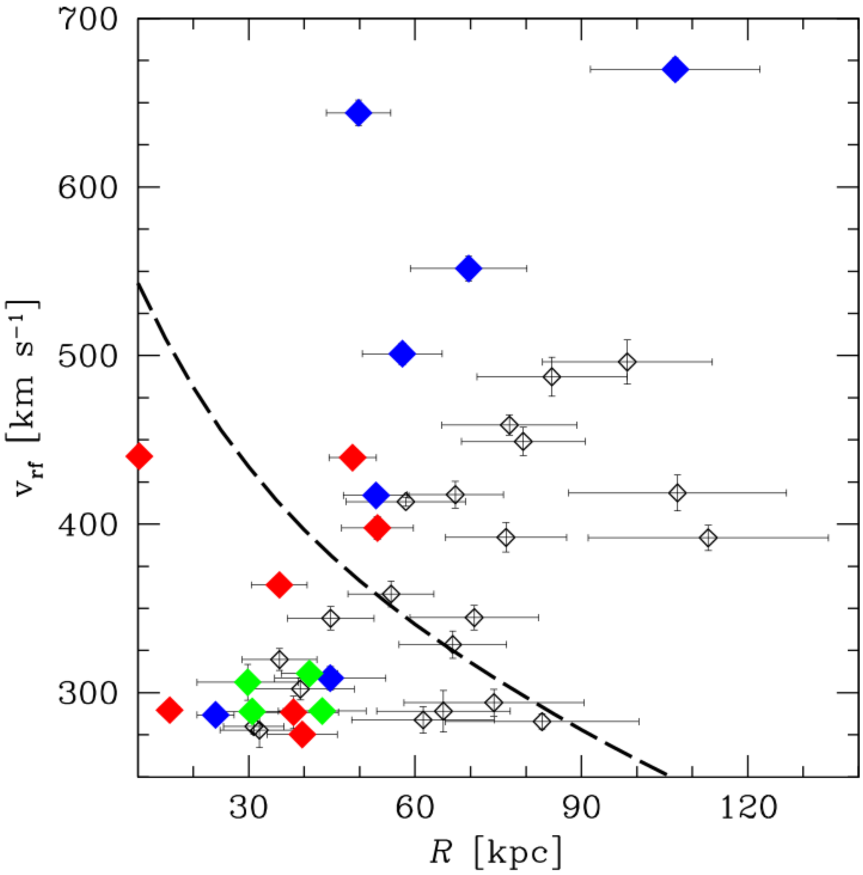

Figure 2.1: Distribution of v_{rf} versus Galactocentric radial distance R for the 39 velocity outliers with Gaia measurements. Dashed line is Galactic escape velocity in the Kenyon et al. (2014) gravitational potential model. Symbol color indicates probable origin: Galactic centre (blue), Galactic disc (red), Galactic halo (green), and ambiguous (empty). (From Fig. 3 Brown et al. (2018))

In a recent study, Boubert et al. (2018) have combined the historical data on high-velocity stars with *Gaia* DR2 data and found that almost all previously-known high-velocity late-type stars are most likely bound to the Milky Way except one late-type candidate that has a reasonably high probability of being unbound from the Milky Way and thus hypervelocity (see Figure 2.3). Marchetti et al. (2019) also search for the fastest stars in the MW using the *Gaia* DR2 catalogue. They derive distance and total velocities distribution of more than 7 million stars in our MW, a small catalogue compared to the full 1.3 billion sources with proper motions and parallaxes. As expected given the relatively small sample size of bright stars, Marchetti et al. (2019) find no HVS candidates. Instead, they find 7 hyper–runaway star candidates, coming from the Galactic disc.

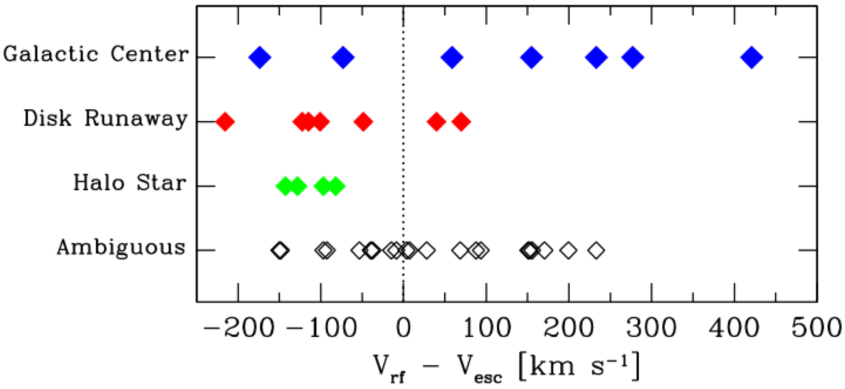

Figure 2.2: Probable origin, on the basis of trajectory and velocity, plotted relative to Galactic escape velocity. (From Fig. 4 Brown et al. (2018))

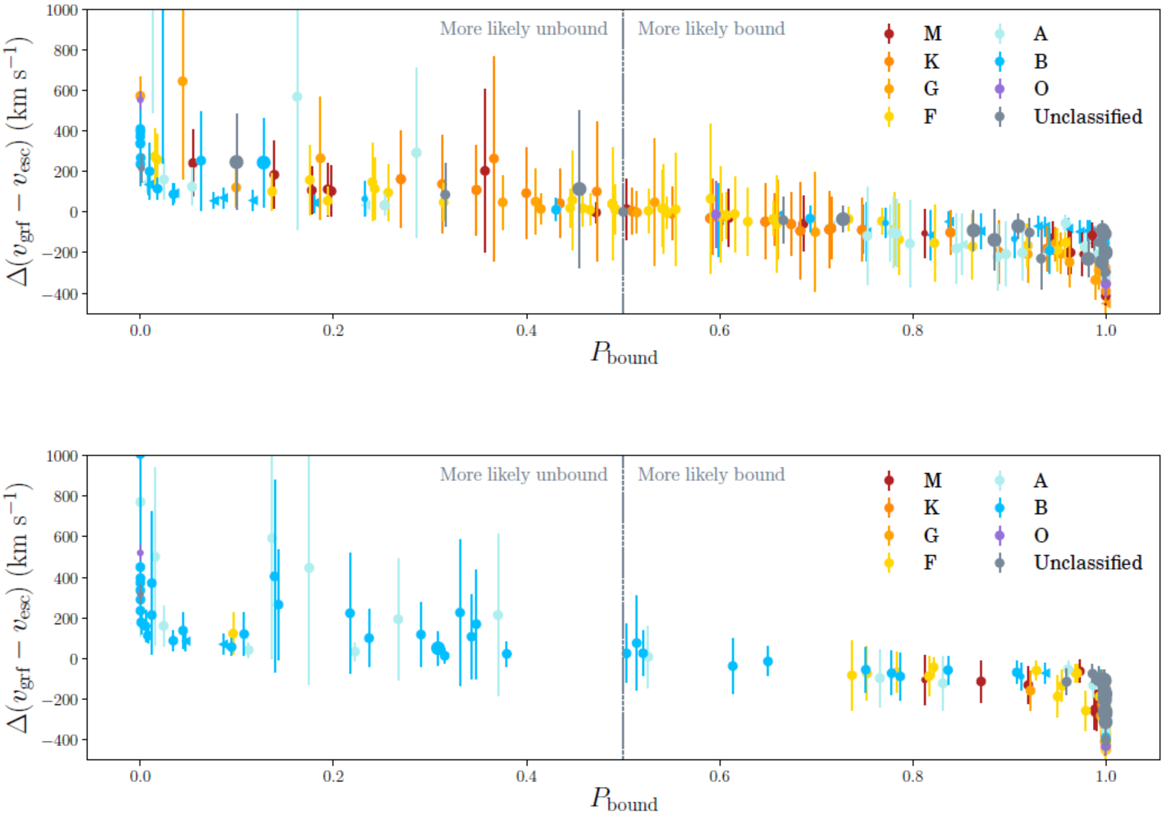

Figure 2.3: The probability of a candidate hypervelocity star being bound to the Galaxy (P_{bound}) versus the difference between the Galactocentric rest-frame velocity and the escape speed. Top: P_{bound} before Gaia DR2, bottom: P_{bound} after Gaia DR2 (from Fig. 2 Boubert et al. (2018)).

In addition, metallicity provides a possible constraint on the origin of HVSs (Brown, 2015). If HVSs are short-lived stars, their abundance patterns should reflect their place of origin. Stars formed in the Galactic Centre are expected to have solar iron abundance and possibly enhanced alpha element abundance (Carr et al., 2000; Ramírez et al., 2000). Stars formed in the Galactic disc should have $[M/H] = +0.3$ if they originate from $R = 4$ kpc and $[M/H] = -0.4$ if they originate from $R = 14$ kpc (Hayden et al., 2014). Early B-type stars in the Solar Neighborhood have solar abundance $[M/H] = 0.0$ (Nieva & Przybilla, 2012). Du et al. (2018), using *Gaia* DR2 data combined with observations from the Large Sky Area Multi-object Fiber Spectroscopic Telescope (LAMOST) Data Release 5, found 24 high-velocity stars which are mostly metal-poor and α enhanced. Adopting the method from Marchetti et al. (2019), Du et al. (2018) measure the probability that stars are derived from the GC is about > 0.16 for these stars.

2.2 Hypervelocity stars versus runaway stars

Not all *high velocity* stars are necessarily hypervelocity stars (HVSs). To distinguish between *high velocity* stars, we have to divide them into two different categories, i.e. runaway stars and HVSs (Capuzzo-Dolcetta & Fragione, 2015). Runaways were initially identified by Humason & Zwicky (1947) as B-type stars at unexpectedly large distances from the disc but historically defined in the context of Galactic disc O and B stars with motions faster than 40 kms^{-1} (Blaauw, 1961). About 30 % of O-type stars and 10% of B-type stars, in the Solar Neighborhood, are runaways based on their peculiar velocities (Gies & Bolton, 1986). Because most O and B stars are born as binaries, runaways are naturally explained by binary disruption mechanisms. There are two proposed ejection mechanisms: supernova ejections and dynamical ejections (Brown, 2015). A runaway star is ejected from a close binary at the moment its companion explodes as a supernova (Blaauw, 1961; Portegies Zwart, 2000; Zubovas et al., 2013). By this method a runaway star can reach a maximum velocity of 200-300 kms^{-1} that is the sum of the supernova kick velocity and the orbital velocity of the progenitor binary (Portegies Zwart, 2000). It is possible that for the binaries composed of early B and a Wolf-Rayet (WR) star, the ejection velocities reach 400 kms^{-1} or higher (Przybilla et al., 2008b). Additional effects may come from asymmetric explosions (Przybilla et al., 2008b). However, in all cases, the ejection velocities are below Galactic escape velocity. An alternative to the binary–supernova scenario is the dynamical ejection scenario based on three- and four-body dynamical encounters in dense stellar systems (Poveda et al., 1967). In the three–body encounter tight very massive binaries interact with a massive star, one member of the binary could be captured by the massive star, while the other star may be ejected with high velocity (Leonard & Duncan, 1990; Gvaramadze et al., 2009; Gvaramadze & Gualandris, 2011; Perets & Šubr, 2012). The early B-type stars (the progenitors of the majority of neutron stars) can be ejected as runaways with velocities of $>$ 200-400 km s^{-1} (typical of pulsars), while 3-4 M$_\odot$ stars can attain velocities of $>$ 300-400 kms^{-1} (typical of the bound population of halo late B-type stars) (Gvaramadze et al., 2009). The runaway production by this process could be responsible for the origin of high peculiar velocities ($\geq$ 70 kms^{-1}) observed for some very massive ($\geq$ 60-70 M$_\odot$) runaway stars in the Milky Way and the Large Magellanic Cloud (e.g. λ Cep, BI237, 30 Dor 016), which can hardly be explained within the framework of the binary–supernova scenario (Gvaramadze & Gualandris, 2011). In stellar binary-binary interactions or that of four–body interactions, smoothed particle hydrodynamic simulations find that high velocity encounters frequently yield merger events instead of ejections owing to tidal dissipation effects (Fregeau et al., 2004; Brown, 2015). The maximum possible ejection velocity in the dynamical ejection mechanism is set by the escape velocity of the most massive star. A runaway may undergo both a dynamical and a supernova ejection in a two–step process and because most runaway ejections are bound, runaways are expected to dominate the population of velocity outliers near the disc. Nevertheless, both the supernova and dynamical ejection mechanisms are probable in nature due to observations (Hoogerwerf et al., 2001) (see Brown (2015) for more details).

Hypervelocity stars (HVS), on the other hand, are stars escaping the host Galaxy through a three–body interaction with a massive gravitational potential such as an SMBH (Hills, 1988) in the centre of the Galaxy. The only runaways that can be confused with HVSs are those rare *Hyper–runaways* in the halo with speeds $>$ 400 kms^{-1} at $R = 50$ kpc (Brown, 2015).

To determine better the diversity of Hypervelocity and hyper–runaways, one requires to compare their ejection rates in the MW. Quantitatively, the Perets & Šubr (2012) dynamical ejection velocity model predicts that 4×10^{-4} of runaways are ejected at $\geq$ 600 kms^{-1} from the Solar circle and decelerate in 400 km s^{-1} at $R = 50$ kpc. Thus the ejection rate of hyper-runaways with analogous velocities with HVSs is 8×10^{-7} year^{-1} . This hyper-runway rate is approximately 1% of the HVS ejection rate. A theoretical estimate of the Milky Way HVS ejection rate of $10^{-3} - 10^{-4}$ year^{-1}, was carried out by Hills (1988), based on the number of hard binaries, $a = 0.1 - 1$ AU expected to encounter the MBH in a full loss cone. This estimation was confirmed by Yu & Tremaine (2003) except for an empty MBH loss cone. Adapting 10^{-4} year^{-1} for the Milky Way HVS ejection rate (Brown, 2015), it can be concluded that the observed number of unbound B stars is consistent with theoretically predicted HVS ejection rates but inconsistent with hyper–runaway ejection rates (see Brown (2015) for more details).

2.3 Reasons for studying hypervelocity stars

Hypervelocity stars (HVSs) are super–fast objects, most likely originated from the Galactic Centre (GC) and can be observed in the halo of the MW at speeds that exceed Galactic escape velocity. The discovery of these fabulous objects thus connect the outer parts of the MW to its very centre and may give a new glimpse for exploring a wide range of mysterious phenomena of our home galaxy. Therefore, HVSs are potentially direct links to the neighborhood of Sgr A* as well as links to the MW dark matter halo.

HVSs departed the centre of the Galaxy in ~ 100 Myr ago thus could mirror the *stellar population* in the proximity of Sgr A*. Substantially, the parent mass function of HVSs can be constrained by combining predictions of HVS rates with the observations. The ratio of high- to low-mass HVSs thus provides a sensitive measure of the stellar mass function near Sgr A*. Since comparing different types of stars is difficult (due to the unknown stellar mass function, multiplicity, and orbital distribution of HVS progenitors), Brown (2015) investigate the ejection rate of specific types of stars targeted in well-defined surveys to compare different types of stars. Brown (2015) study the 20 G- and K-type stars from the SDSS+SEGUE spectroscopic catalog (3.6% of sky). Moreover, they search for G– and F–type stars with unbound radial velocity (Kollmeier et al., 2009) through 291,111 SDSS stellar spectra and did an optimized search for unbound F–type stars in the SDSS+SEGUE. Brown (2015) find an ejection rate of $\sim 10^{-2}$ year^{-1} for unbound G– and K–type stars near the Sun which are thus much more numerous than any runaway or HVS ejection mechanism can explain. Their inspection for G– and F–type stars in SDSS spectra results in zero although careful consideration of survey volume yields an upper limit on the ejection rate of unbound G-type stars of $< 3 \times 10^{-4}$ year^{-1}. The search for F–type stars in the SDSS+SEGUE also yields to zero with a similar upper limit on the ejection rate of unbound F-type stars of $< 4 \times 10^{-4}$ year^{-1} (Kollmeier et al., 2010). The observed rate of unbound late B-type stars (2.5–4 $M_\odot$ main-sequence stars at 50–120 kpc distances) is consistent with the theoretical 10^{-4} year^{-1} HVS ejection rate but is 100 times greater than the hyper-runaway rate. The number of unbound B stars in the halo, therefore, supports a Galactic Center origin (Brown, 2015).

HVSs could be proficient detectors of *binary fraction* in the centre of our Galaxy. Due to Hills (1988) mechanism, astronomers believe that HVSs are the remnants of tidal disruption of binary stars that got very close to the SMBH in the GC. Thus the properties of binaries in the GC are tied to the HVSs since roughly all O and B type stars in the disc are in binaries including a third equal–mass twin population (Kobulnicky & Fryer, 2007). Besides, HVSs present a direct exploration of the origin and multiplicity of the nearest stars distributed around Sgr A* if one assumes those stars as disrupted companion of HVSs (Hills, 1988; Ginsburg & Loeb, 2006, 2007; Antonini et al., 2010) and even if planets or planetary systems inhabit in the innermost region of the GC ((Ginsburg et al., 2012), chapter 4 and 5 of this thesis).

Furthermore, simply owing to binary disruptions and subsequent tidal disruption events HVSs can be associated with the growth of central SMBHs. Dynamical calculations suggest that a significant fraction of the former companions in Hills mechanism give rise to tidal disruption events (Bromley et al., 2012). As a result, the SMBH may have grown by a factor of 2–4 in the past 5–10 Gyr straightforwardly taking into consideration the numbers of observed HVSs and S–stars in the MW (Brown, 2015). So, the ejection rate of HVSs is directly associated with the mass growth of the central SMBHs.

Another interesting point is that, as demonstrated by Hansen (2007); López-Morales & Bonanos (2008), observed HVSs in the MW are slow– and also fast–rotator, suggesting different acceleration origins. This proposes that fast–rotating HVSs have not generated by interactions of binary stars with an SMBH. This feature exhibits *ejection history* of various HVSs. For instance, 5 HVSs near ∼ 120 Myr display the evidence that a massive star cluster or IMBH has in-spiralled into the Galactic Center in the past couple hundred Myr since lower velocities at shorter travel times are not expected to come from a single ejection event, in the opposite sense required for ejections from an in-spiralling IMBH.

Finally, the existence of HVSs in the halo of the Galaxy can theoretically be applied as probes of the Galactic dark matter potential (Gnedin et al., 2005; Yu & Madau, 2007; Fragione & Loeb, 2017; Hattori & Valluri, 2019). Moreover, exploiting the kinematics of HVSs is important to constrain the mass distribution of our Galaxy.

2.4 Different scenarios for acceleration of hypervelocity stars

The detection of fast-moving stars has tremendously improved throughout the last decade. Although, majority of these stars are plausibly surmised to bring about by an SMBH-stellar binary interaction, howbeit other mechanisms could undertake their production. In this section, different scenarios which are accountable for high-velocity stars ejection are discussed. Besides, it is important to denote that the S-star formation channel is connected simultaneously to HVS production in most of the mechanisms introducing below.

2.4.1 Binary disruption by an SMBH

The earliest and most popular mechanism, to produce incredibly fast–moving HVSs that are indeed gravitationally unbound to the MW, presented by Hills (1988), involves the disruption of a pair of stars after getting captured in the Supermassive black hole's potential well. As one of the stars is seized by the SMBH and remains on highly eccentric orbits or spirals in towards the SMBH, its companion is thrown out of the MW at a tremendous velocity. So far the Hills' three–body exchange mechanism has been studied analytically and computationally by several authors and is efficiently comprehended (e.g. Yu & Tremaine (2003); Ginsburg & Loeb (2006); Bromley et al. (2006); Kenyon et al. (2008); Zhang et al. (2010); Antonini et al. (2010); chapter 4 of this thesis). Application of the Hills mechanism corroborates that a supermassive black hole (SMBH) lurks at the centre of the Galaxy on account of the consistency of the HVSs creation rate with the observations (Perets, 2009a). *Gaia* DR2 provides improved proper motions for many HVSs that may directly link HVSs to their SMBH origin. Using these measurements, Brown et al. (2018) proved the Galactic Centre origin of several number of HVSs verifying powerfully the Hills mechanism. Although this information supports strongly production of HVSs due to Hills mechanism, it is still unclear if "all" the HVSs are originated via this method.

2.4.2 Stellar cluster disruption

As a supplemental method Capuzzo-Dolcetta & Fragione (2015); Fragione & Capuzzo-Dolcetta (2016) discussed the accelerations of stars to hypervelocities due to the close interaction of a single or massive black hole binary (BHB) and a passing–by, orbitally decayed massive stellar cluster (Arca-Sedda et al., 2016) employing N–body simulations. The underlying procedure is also a three–body encounter where the bodies are the SMBH (of 10^8 $M_\odot$), the Globular Cluster and the test star belonging to the Globular Cluster. During the cluster orbital motion, it has the probability to pass close to an SMBH in the centre of its host galaxy. The likelihood of this passage is enhanced due to dynamical friction braking which makes the massive cluster spirals into a dense galactic centre region (Tremaine et al., 1975; Capuzzo-Dolcetta, 1993; Capuzzo-Dolcetta & Miocchi, 2008a; Antonini et al., 2012). When the stellar cluster passes by the SMBH, some of its stars can be stripped from the cluster and ejected with high velocities.

As a matter of fact, the existence of black hole binaries (BHBs) in some galactic centres is a necessary consequence of hierarchical galaxy formation (Yu, 2002; Milosavljević & Merritt, 2003). Scattering of the stellar cluster with a secondary BH, comparable in mass with the primary, leads to a peculiar distribution velocity for the stars ejected at high velocities. Comparison of these distributions with the proper motion and radial velocity data of galaxies with 10^8 $M_\odot$ central black hole(s) can shed light to the discrimination of a central single or binary BH. Moreover, the infall of a Globular Cluster on a massive BHB could increase the energy loss by the BHB and conduce them to the final stage, where gravitational waves emission is the main mechanism to cause the energy loss of the binary.

The interaction of a young passing–by stellar cluster and the Milky Way's SMBH results in both single and binary HVSs (Fragione et al., 2017). The hypervelocity binaries (HVBs) can have three different fates; they can survive and continue their journey, merge or can be disrupted as a consequence of the velocity kick. The N-body simulations of Fragione et al. (2017) concludes in compact and eccentric HVBs. According to Kroupa (1995), they estimate $\sim 7\%$ of HVBs merge originating blue–straggler HVSs while traveling across the Galaxy at hypervelocities.

2.4.3 Close encounters between two single stars

Two–body gravitational interactions between two single stars can eject one of the two stars (Henon, 1969; Lin & Tremaine, 1980). Theoretically, Yu & Tremaine (2003) show that due to this process the rate of ejection with velocities $\geq 10^3 kms^{-1}$ is only about 10^{-11} year^{-1} for solar–type stars. Therefore, practically the probability of single stars' close encounters is too rare to be detectable. Maybe stars with impact parameters of a few solar radii can produce velocity changes that are large enough to be considered as an HVS ejection.

2.4.4 Interaction with a black hole binary

Substituting one star of the binary system in Hills mechanism with a black hole can lead to another three–body interaction for production of HVSs. Yu & Tremaine (2003) noted that, in theory, a binary black hole (BHB) may interact with a single star and result in the slingshot of the star as an HVS. This hypothesis was based on a work formerly done by Hansen & Milosavljević (2003) arguing that young stars observed at central arcsecond of the MW may have been shorn from cluster surrounding an intermediate-mass black hole (IMBH) of mass $10^3 - 10^4$ M$_\odot$ inspiralling toward Sgr A*. Because of continuously dynamical interactions with the surrounding stellar population, a massive BHB undergoes energy exchanges with low angular momentum stars passing near it. Eventually, most of those stars will be cast out with the energy obtained after one or several encounters with the BHB.

A Secondary possibility could be the investigation of an inspiralling IMBH on to an SMBH surrounded by a cusp of bound stars. Sesana et al. (2007) studied the scattering of stars bound to Sgr A* by an in-spiralling IMBH and compared the predicted radial and velocity distributions of HVSs with the limited-statistics data available on that time, and showed that the IMBH model appears to produce a spectrum of ejection velocities that is too flat. In contrast with the observations of 3–4 M$_\odot$ HVSs, the "IMBH model" comes out to give rise to an excess of HVSs with extremely fast velocities of $V > 1500$ kms^{-1}. Later Sesana et al. (2008) develop the "IMBH model" and examine the same scenario taking advantage of N–body simulations and find that depending on binary mass ratio, eccentricity, and initial slope of the stellar cusp, a core of radius ~ 0.1 pc typically forms in 1–10 Myr which on this timescale about 500–2500 HVSs are expelled with speeds sufficiently large to escape the gravitational potential of the Milky Way.

The "IMBH model" is also examined via numerical methods. Baumgardt et al. (2006); Löckmann & Baumgardt (2008) performed N–body simulations of inspiralling intermediate-mass black holes all starting from circular orbits at an initial distance of 0.1 pc from the centre of the MW. Their simulations show that the presence of IMBHs in the Galactic Centre deplete the central cusp of stars and change the stellar density distribution inside $r < 0.02$ pc into a core profile which takes at least 100 Myr to refill. Baumgardt et al. (2006) found that as a consequence of the IMBH inspiral, HVSs are composed with nearly isotropic spatial distributions that make it complicated to recognize them from HVSs via binary star–SMBH interactions.

With the assumption of two massive black holes (MBHB) instead of an intermediate-mass black hole, Sesana et al. (2006); Sesana et al. (2008) looked into a new model for HVSs expulsion to quantify the properties of the HVSs that would populate the halo of the MW in the presence of an MBHB at the GC. Based on eccentricity, initial semi–major axis of the pair, and with the assumption of an MBHB of mass 3.5×10^6 $\mathrm{M}_\odot$ (that Sgr A* is the most massive component of the pair, and that the binary mass ratio is $q = 1/81$, and that the loss-cone is always full), Sesana et al. (2006) realized the number of created HVSs ($\sim 10^4 - 10^6$) still is not in agreement with the real observations.

On the other hand, Rasskazov et al. (2019) improved "IMBH model" simulations, profiting the accurate `AR-CHAIN` algorithm performing another series of three–body interactions. A potential intermediate-mass black hole is supposed to orbit the central supermassive black hole in our Galactic Centre. An unbound star is expelled out as HVS, after encountering the SMBH–IMBH binary.

Rasskazov et al. (2019) found two discrepancies in the calculation of the eccentricity evolution rate and direction of the ejection velocity distribution (in the plane of the binary) with the results of Sesana et al. (2006). It seems that Sesana et al. (2006) used an incorrect procedure to calculate the eccentricity evolution rate since these values due to Rasskazov et al. (2019) are up to 1.5 times higher. Also scattering experiments of Rasskazov et al. (2019) illustrate that the direction of the ejection velocity is non-uniform for eccentric binaries with a peak at $\lesssim \pi$ not at $3\pi/2$ as in Sesana et al. (2006). Their new findings demonstrate the HVS velocity directions are concentrated around the binary orbital plane with a preferred direction in the binary plane if the binary were an eccentric one.

Moreover, regardless of the binary or stellar parameters, the HVSs velocities distribution found to be a power–law $(dN/dv) \propto v^{-4}$. Besides, Rasskazov et al. (2019) results compared with Hills mechanism shows that IMBH model causes an ejection velocity distribution which is flattened towards the BH binary plane while the Hills mechanism produces a spherically symmetric one with faster stars on average.

Lu et al. (2007) demonstrated that a four–body interaction among a binary star and a binary black hole residing in the centre of our Galaxy can expel hypervelocity binaries (HVBs) with velocities above 1000 kms^{-1} while both stars preserving their integrity. Nevertheless, the recent discovery of a candidate HVB ~ 5.7 kpc away from the Centre of the MW with ejection speed of ~ 570 kms^{-1}

(Németh et al., 2016) may justify the existence of a hypothetical massive black hole binary in our Galactic Centre.

2.4.5 Stellar–mass black holes

O'Leary & Loeb (2008) offered a novel scenario for generating HVSs assuming that stars within 0.1 pc of the Galactic Centre face a cluster of stellar–mass black holes that have migrated to that region. The main idea is based on this probe that if the stellar population of the bulge contains black holes formed in the final core collapse of ordinary stars with mass $m \gtrsim 30$ M$_\odot$ then about 25,000 stellar–mass black holes should have segregated by dynamical friction into the central parsec of the MW, forming a black hole cluster around the central supermassive black hole (Morris, 1993; Miralda-Escudé & Gould, 2000).

O'Leary & Loeb (2008) calculated the rate at which stars will scatter off black holes and populate the MW halo. For small ejection velocities ($\sim$ 100 kms^{-1}) the rate does not depend on the stellar mass function or mass of the black holes and drops approximately as a power law $\propto v_{ej}^{-2.5}$. For large velocities ($\gtrsim$ 800 kms^{-1}) the rate of HVSs gets suppressed due to tidal dissipation and Star–BH collisions. In contrast to Hills mechanism with ejection velocities go over 4000 kms^{-1} (Bromley et al., 2006; Ginsburg & Loeb, 2006), the observed distribution of HVSs via such encounters could not reach speeds $\sim$ 2000 kms^{-1}. Thus this can be a drawback of this method that could not be employed for interpretation of the most HVSs ejections.

2.4.6 Dynamical evolution of a disc

Rather than examining the interaction of a binary star and SMBH individually, the interaction of a disc of binaries can be presumed to study the production of HVSs and S–stars. In the Hills mechanism, to produce an HVS, binary stars are required to approach closely to the SMBH in the centre of the MW. These binaries could be originated at distances above 1 pc from the SMBH and brought inwards within a massive young star cluster as proposed by Gould & Quillen (2003) or scattered due to relaxation enhanced by massive perturbers as discussed by Perets et al. (2007). Löckmann & Baumgardt (2008) noted that binaries might come close to the SMBH via the Kozai–Lidov mechanism that can excite the orbital eccentricities and transport them to the vicinity of the SMBH. As a consequence of these concepts, we can mention the young stars which are observed in the Galactic Centre at the distances $0.04 \leq r \leq 0.4$ pc from Sgr A*. It appears that a subset of these stars orbits around the SMBH in a thin disc (the so–called clockwise disc) (Levin & Beloborodov, 2003). Haas & Šubr (2016) employed an N–body modelling to investigate the dynamical evolution of a thin and eccentric disc of stars with a 100% fraction of binaries orbiting around the SMBH in our Galactic Centre.

Considerable amounts of binaries are brought to the vicinity of the SMBH simply because of the effect of the Kozai–Lidov (Kozai, 1962; Lidov, 1962) oscillations on orbital parameters of the binaries which are induced by the disc itself. As a consequence, enhancement of the eccentricity of binary orbits around the SMBH transfer them to the tidal break-up radius at which they are separated, result in the ejection of one star as high or hypervelocity and capture of its twin around the SMBH as S–star. In this model, qualitatively, kinematic properties of the HVSs and S–stars are in agreement with those of the observed stars. The binary fraction of the clockwise disc is not well determined either from the observation or from star formation models in the Galactic Centre. However, the total number of generated HVSs, as well as their velocity distribution, strongly depends on the properties of the initial binary population which leaves the validity of the model ambiguous.

2.4.7 Triple tidal disruption

The binary star in the Hills mechanism can be replaced by a triple star system interacting with the central massive black hole. Studies show that a hypervelocity binary (HVB) can be a consequence of a triple system encountering with an SMBH. As mentioned in section 2.4.4 an HVB candidate has been discovered recently at a distance of ≈ 5.7 kpc from the Galactic Centre. The existence of such fast–moving binary stars had been predicted by Perets (2009b) through a triple tidal disruption by an SMBH. Perets (2009b) noted that some of these HVBs may merge and form blue stragglers. This is due to the fact that the apparent main–sequence lifetime of a few observed HVSs is estimated to be shorter than the flight time from the GC. Thus these HVSs might have been HVBs which evolved into a blue straggler star due to internal processes after ejection. In fact, the detected star in the halo could be a rejuvenated HVB.

Fragione & Gualandris (2018) retested the triple tidal disruption scenario using high–precision `AR-CHAIN` code, for various inner and outer binary separations as well as different star masses to include the most likely values obtained by Perets (2009b). Their results conclude that a very small fraction of encounters $\lesssim 1\%$ can produce HVBs. Although we do not have satisfactory statistics about the fraction of triple systems or other information such as the semimajor axis or mass of these systems but to have an idea about the rate of HVB production, Fragione & Gualandris (2018) assume that nearly 13% of stars are found in triples (Tokovinin, 2014), which gives the ejection rate of $\approx 1\ \mathrm{Gyr}^{-1}$. This interprets into roughly 10 HVBs to be found in the Galaxy from the triple disruption mechanism.

2.4.8 Supernovae explosions

In the binary supernova mechanism, a stellar binary is unbound when the primary star explodes as a supernova (Blaauw, 1961), due to mass loss and a natal kick if the explosion is asymmetric. Via

Monte Carlo simulations, Zubovas et al. (2013) examined the likelihood of HVS production through supernovae happening within binaries in a disc of stars around Sgr A*. Zubovas et al. (2013) propose that a disk of stars analogous to the disks of young stars currently observed in the central parsec (Paumard et al., 2006) formed during extended GC star formation over the last $\sim$ 108 yr (Blum et al., 2003). Core-collapse supernovae will have disrupted many of these binaries, ejecting some secondary (less massive) stars with a range of terminal velocities. They took into account the effects of binary hardening (reduction in binary separation), which may occur as binaries migrate through a gaseous disc from which the binary stars formed (Baruteau et al., 2011). Three cases no hardening, moderate hardening (binary separation reduced by 2) and strong hardening (binary separation shrunk by 10) give rise to 37, 75 and 512 HVSs, respectively, meaning the strong hardening case increases Supernova–induced HVS production. Besides, the probability that a secondary has terminal velocity $> 400kms^{-1}$ reaches to a maximum for the strong hardening model. This implies that massive binaries formed in the few central parsecs of the GC to have had typical separations a factor 2 less than those in the field at the point just before the supernova explosion. The rate of binary ejections in Zubovas et al. (2013) work is $\sim 10^{-4}$ yr^{-1}, comparable to that of the tidal disruption processes.

Another systematic Monte Carlo simulation was carried out by Tauris (2015) to investigate the maximum possible velocities of HVSs when asymmetric supernovae are considered i.e. when the newborn neutron star receives a momentum kick at birth. Tauris & Takens (1998) derived analytical formulae to calculate the velocities of stars ejected from binaries in which asymmetric supernovae occur. Their computation shows that the companion's ejection speed is related to different parameters such as the mass of both stars, their initial separation and the kick velocity imparted on the newborn neutron star. Although it seems that the average kick velocities lies in the range 400–500 kms^{-1} (Lyne & Lorimer, 1994; Hobbs et al., 2005), however, Tauris (2015) found values of 1000–1200 kms^{-1}. Such large kicks may be realistic taking into account some larger estimations for neutron star kicks including the radio pulsars B2011+38 and B2224+65 (Hobbs et al., 2005) ($v \gtrsim 1500\ kms^{-1}$ for both), IGR J11 014-6103 (Tomsick et al., 2012; Pavan et al., 2014) ($v \gtrsim 1000\ kms^{-1}$) and B1508+55 (Chatterjee et al., 2005) ($v \gtrsim 1100\ kms^{-1}$). Furthermore, via this mechanism the HVSs reach up to $\sim 770\ kms^{-1}$ and $\sim 1280\ kms^{-1}$.

2.4.9 Tidal disruption from satellite galaxies

Edelmann et al. (2005) noted that HVS3 is only 16.3° from the centre of the Large Magellanic Cloud (LMC) and that the star was consistent with being ejected from the LMC's centre 35Myr ago at $\sim$ 700 km s^{-1}. An origin in the LMC solves the problem that HVS3 would not live long enough to survive the journey from the Galactic Centre to its current location. Recently, Erkal et al. (2019), using proper motion measurements from *Gaia* DR2, find that HVS3 is highly likely to be coming almost from the centre of the LMC. During its closest approach, $21.1^{+6.1}_{-4.6}$ Myr ago, it had a relative velocity of $870^{+69}_{-66} kms^{-1}$ with respect to the LMC. This large kick velocity is only consistent with the Hills mechanism, requiring a massive black hole near the centre of the LMC. This provides strong evidence that the LMC harbours a massive black hole of at least $4 \times 10^3 - 10^4 M_\odot$ (Erkal et al., 2019).

As another example, Li et al. (2012) searched through Sloan Digital Sky Survey (SDSS) Data Release 7 and identified 13 F-type hypervelocity star candidates. They used SEGUE spectroscopy and proper motions from the SDSSUSNO (Munn et al., 2004). They argued from orbit integrations that 9 candidates emanated from the Galactic Centre of the disc, whilst the remaining 4 had a more exotic origin, such as tidal disruption of dwarf galaxies (Abadi et al., 2009). If HVSs are the tidal debris of a typical star-forming dwarf galaxy in the Local Group, the stars should have $-2 < [M/H] < -0.5$ (McConnachie, 2012). Du et al. (2018) found 24 high-velocity stars (using *Gaia* DR2 data and spectroscopy from ground-based spectroscopic survey LAMOST DR5) and five of them appear to have an origin in the tidal debris of a disrupted dwarf galaxy.

Moreover, utilizing the new proper motion and velocity information available from *Gaia* DR2, Boubert et al. (2018) found only one late-type object (LAMOST J115209.12+120258.0) that is unbound from the Galaxy. Performing integrations of orbital histories, Boubert et al. (2018) realized that this object cannot have been ejected from the Galactic centre and thus may be either debris from the disruption of a satellite galaxy or a disc runaway.

Chapter 3

Numerical background: algorithmic regularization of the few-body problem

In the following, I describe the construction of numerical integration which has been implemented in the Algorithmic-Regularization-Chain code (`AR-CHAIN`). First, I introduce a historical background of the methods for removing singularities from the equations of motion (regularization) which have been developed for almost a century. Then I will discuss various versions of `AR-CHAIN` for arbitrary mass ratios. Finally, I will introduce the modified version of `AR-CHAIN` , the `ARGdf` code, used in our work.

3.1 Historical overview

The numerical integration of the gravitational N-body problem under a Newtonian force has always been a difficult and time-consuming task since the employment of computers in astrodynamics and celestial mechanics. The classical methods were not satisfactory simply because during the integration of an N-body system the well known singularity of the force at zero distances creates difficulties if studied by direct methods. The particular challenge is when applying numerical techniques for few-body scattering and the interaction with black holes in galactic centres. Inevitably, such interactions induce the formation of strongly perturbed two-body motion. Since the common time-step cannot exceed the Kepler period, the created two-body systems (that have semi-major axes much smaller than the interparticle distance) thus require special *regularization* treatment.

Regularization is the procedure of presenting appropriate space and time variables such that in binary collisions, i.e. where the distance of two point masses reaches an arbitrarily small value, the equation of motion becomes regular and singularities disappear. The regularized differential equations could be solved then by means of conventional numerical integrators.

The main concept was provided by Levi-Civita (1920) for the regularization of the special case of the binary collisions in the planar (2-dimensional) Kepler problem. A procedure which is accomplished in three steps; firstly, defining a "fictitious" time instead of the physical time as an independent variable proposed originally by Sundman (1907) to slows down the motion whenever the distance of two masses is small. Then representing a "conformal squaring" between the parametric u-manifold i.e. a Riemann surface with two sheets, and the physical x-plane. Finally, the elimination of first derivatives by means of using new variables in the energy equation (Waldvogel, 2008).

Kustaanheimo (1964) and Kustaanheimo & Stiefel (1965) generalized the notion to three dimensions, often abbreviated as *KS regularization*, applying both coordinate transformation and a time transformation. After Stiefel & Scheifele (1971) published their book about inclusive use of the KS-regularization for the perturbed two-body problem, the implementation of the method became favoured to a wide range of problems characterized by dominant motion. Aarseth & Zare (1974); Zare (1974) and Heggie (1974) took advantage of KS regularization method to deal with the general three-body motion, whereas Heggie (1974) utilized it for the N-body problem then. However, another powerful regularization method was required for the general case of comparable masses, the chain concept. The birth of the chain structure was the paper by Mikkola & Aarseth (1989) which was sharpened later in Mikkola & Aarseth (1993) for implementation on dominant interactions in few-body systems (small N-body systems), known as KS-chain algorithm. In addition, Mikkola & Tanikawa (1999a,c) and Preto & Tremaine (1999) created a new method of regularization by manipulating the Hamiltonian and using a modified leapfrog method as the basic integrator. Further, to handle systems with very large mass ratios, Mikkola & Aarseth (2002) produced the Time Transformation Leapfrog method combined with the Bulirsch–Stoer extrapolation (Gragg, 1964, 1965; Bulirsch & Stoer, 1966) that slows down the internal dominant two-body motion. The usage of extrapolation method relies upon the time–symmetry of the leapfrog algorithm which in the case of requiring velocity–dependent perturbations such as relativistic terms, it is not possible unless symmetrizing the time with help of a generalized midpoint method as in Mikkola & Merritt (2006) particularly for the case of two-body problem. Eventually, the `AR-CHAIN` algorithm (Mikkola & Merritt, 2008b) includes all the methods mentioned above with the superiority of choosing the right version of it work for arbitrary mass ratios.

3.2 Algorithmic Regularization Chain Integrator (AR-CHAIN)

In this section, I describe development in the `AR-CHAIN` integrator formulation during years, from the implementation of the chain structure to the mixture of the Logarithmic Hamiltonian (logH) and Time Transformation Leapfrog (TTL) methods. Then I conclude with the version of `AR-CHAIN` which we applied in our work, the `ARGdf` (hereafter the units are chosen so that the gravitational constant $G = 1$).

3.2.1 The chain concept (KS-CHAIN integrator)

The chain idea was invented by Mikkola & Aarseth (1989, 1990) for high precision computation of particle motions with strong interactions in small N-body systems (N >3) and then was reformulated in Mikkola & Aarseth (1993) to fulfil the motion of an arbitrary number of bodies. The importance of chain configuration lies in the fact that if the centre of mass coordinates was selected, instead of the chain, for distant close pairs the relative coordinates would have been the differences of large numbers that leads to noticeable roundoff errors. The algorithm is such that a chain of interparticle vectors is created to cover all the particles of the system. To construct the chain, after calculation all the distances in the system and arranging them, the shortest distance between two particles is found then the closest particle to one of the components of the present chain is identified. This particle is attached to the nearest end of the chain and this procedure proceeds to include all the particles in the chain. The algorithm is very cautious; if non-chained lengths are shorter than the smallest chain vectors or if two chain vectors form a triangle that has one shorter non-chained side, the chain will be updated to embrace small distances in the chain after every integration step (see Figure. 3.1).

After formation of chain vectors, the next step is transformation to regularized KS variable. A system of N point masses with inertial coordinates r_i, velocities v_i and masses m_i $(i = 1, ..., N)$, are now renamed as $1, 2, ..., N$ and linked along the chain. One may use the generating function

$$S = \sum_{k=1}^{N-1} W_k(r_{k+1} - r_k), \tag{3.1}$$

in order to obtain the momenta $p_k = \partial S/\partial r_k$ as the relative momentum vectors W_k

$$p_k = W_{k-1} - W_k \qquad\qquad (k = 1, ..., N), \tag{3.2}$$

with $W_0 = W_N = 0$. Neglecting the centre-of-mass motion, the unperturbed Hamiltonian will take the form

$$\begin{aligned} H &= T - U \\ &= \sum_{k=1}^{N-1} \frac{1}{2}\left(\frac{1}{m_k} + \frac{1}{m_{k+1}}\right) W_k^2 - \sum_{k=2}^{N} \frac{W_{k-1}.W_k}{m_k} \\ &\quad - \sum_{k=1}^{N-1} \frac{m_k m_{k+1}}{R_k} - \sum_{1\leq i\leq j-2} \frac{m_i m_j}{R_{ij}}, \end{aligned} \tag{3.3}$$

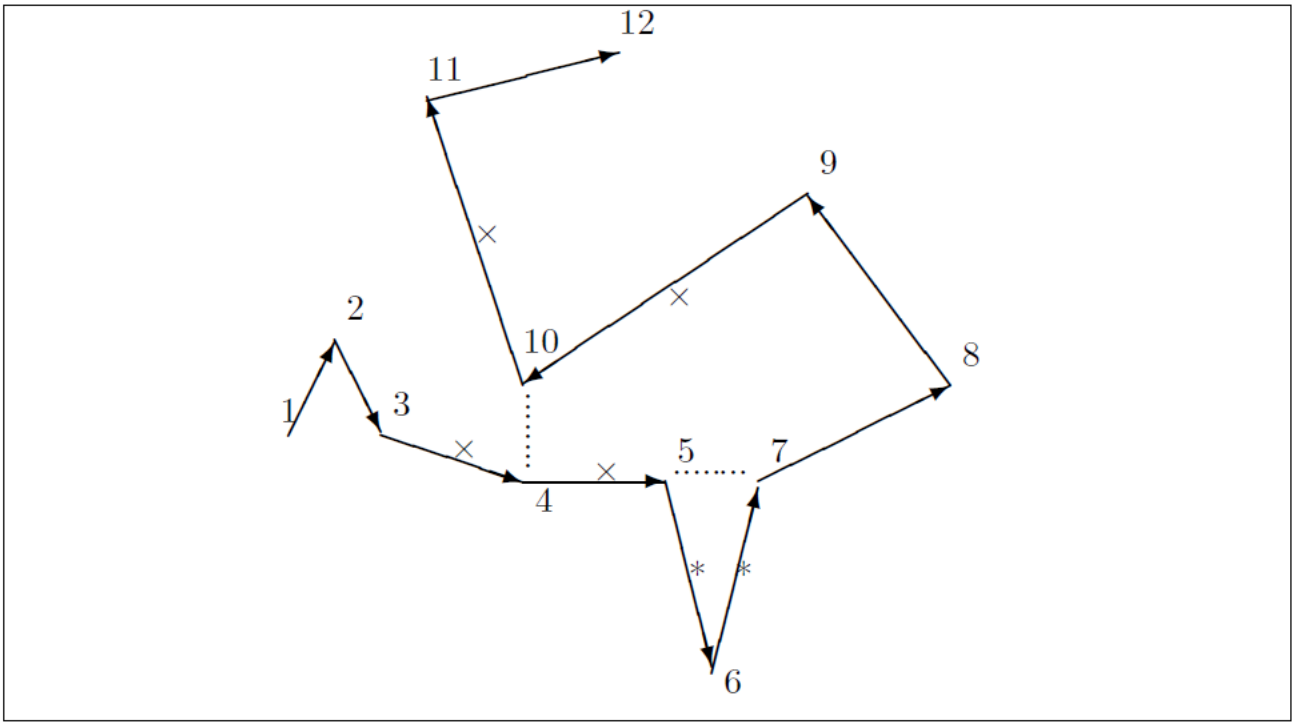

Figure 3.1: Construction of the chain and demonstration of two instances when the chain needs an update; dashed line between 5 and 7 is shorter than lengths marked by * and dashed line between 4 and 10 is shorter than those chained vectors in two sides of 4 and 10 marked by × (both dashed lines are non-chained vectores). If this happens, formation of a new chain is needed. (From Fig. 1 Mikkola & Aarseth (1993))

where $R_k = |X_k|$ are the chain vectors and

$$R_{ij} = \left| \sum_{i \leq k' \leq j-1} X_{k'} \right|$$

are the non-chained distances. If the chain vectors are defined as $X_k = r_{k+1} - r_k$ and chain velocities as $V_k = v_{k+1} - v_k$, by replacement of the KS–transformation of coordinates

$$X_k = \widehat{Q_k} Q_k, \tag{3.4}$$

and momenta

$$W_k = \widehat{Q_k} P_k / (2Q_k^2), \tag{3.5}$$

where $\widehat{Q}$ indicates the well known KS–matrix (Stiefel & Scheifele, 1971)

$$\widehat{Q} = \begin{pmatrix} Q_1 & -Q_2 & -Q_3 & Q_4 \\ Q_2 & Q_1 & -Q_4 & -Q_3 \\ Q_3 & Q_4 & Q_1 & Q_2 \\ Q_4 & -Q_3 & Q_2 & -Q_1 \end{pmatrix} \tag{3.6}$$

the Hamiltonian in terms of the regularizing variables Q_k, P_k can be achieved. Now employment of the time transformation $dt = g d\tau$ where $g = 1/L = 1/(T+U)$ the inverse Lagrangian, the regularized Hamiltonian is obtained as $\Gamma = g(H - E) = (T - U - E)/(T + U)$ (Aarseth, 2003) and produces the equations of motion of the form

$$\frac{dQ}{d\tau} = \frac{\partial \Gamma}{\partial p_k}, \qquad \frac{dP_k}{d\tau} = -\frac{\partial \Gamma}{\partial Q_k} \tag{3.7}$$

which signify the two-body solutions are regular for any $R_k \to 0$.

3.2.2 Logarithmic hamiltonian

In order to apply explicit symplectic integration together with regularization methods, a simplified form of the Hamiltonian is required. Such regularization methods (e.g. Mikkola & Aarseth (1990, 1993)) operate a time transformation function and a KS coordinate transformation so that the Hamiltonian becomes inseparable because of the involvement of coordinates in the kinetic energy. Consider the Hamiltonian $H = T - U$ and applying the time transformation $ds = U dt$ (where s is the new independent variable). Mikkola & Tanikawa (1999a) and simultaneously Preto & Tremaine (1999) demonstrated the logarithmic Hamiltonian (LogH) in the extended phase space as

$$\Lambda = log(T + P_t) - log(U), \tag{3.8}$$

where $P_t = -E_0$ (the momentum of time) is the negative energy of the system. Then the equations of motion can be written as

$$\mathbf{p}_k^{'} = -\frac{1}{U}\frac{\partial U}{\partial \mathbf{r}_k}, \tag{3.9}$$

$$\mathbf{r}_k^{'} = -\frac{1}{T-E_0}\frac{\partial T}{\partial \mathbf{p}_k}, \tag{3.10}$$

$$t^{'} = \frac{\partial \Lambda}{\partial P_t} = \frac{1}{T-E_0}, \tag{3.11}$$

$$P_t^{'} = -\frac{\partial \Lambda}{\partial t} = \frac{1}{U}\frac{\partial U}{\partial t}, \tag{3.12}$$

with the N-body kinetic energy $T = \sum_{k=1}^{n}(\mathbf{p}_k^2/2m_k)$ and force function $U = \sum_{i<j}(m_i m_j/r_{ij})$. In these equations the derivatives of coordinates and momenta are joint and the right hand sides of these equations do not depend on the left hand side variables. Thus, the application of the simple leapfrog algorithm is possible and provides regular results in case of two-body motion but still coping with close multi-particle collisions could not be accomplished correctly. Hence, later Mikkola & Tanikawa (1999c) completed the method by utilization of the extrapolation algorithm (Gragg, 1964; Bulirsch & Stoer, 1966) for more precision.

3.2.3 Time transformed leapfrog

None of the discussed regularization schemes above are able to maneuver very well the case of extremely large mass ratios as the equations of motion are created with the energy terms which are controlled by the large bodies of the system, accordingly the zero masses could not be treated (Mikkola & Aarseth, 2002). In order to deal with Supermassive black holes (SMBH) or black hole binaries in galactic nuclei, other kind of treatment or smoothing method is desirable. The mentioned chain regularization is unlikely handling systems with such massive black holes because the total subsystem energy that explicitly appears in the equations of motion is dominated by the binary components with small periods and large binding energies (Aarseth, 2003).

To manage this problem, Mikkola & Aarseth (2002) introduced a novel time transformation procedure with some correspondence and connection with their Logarithmic Hamiltonian (LogH) method (Mikkola & Tanikawa, 1999a,c). In this new treatment, to solve a system of second–order differential equations

$$\ddot{\mathbf{r}} = \mathbf{F}(\mathbf{r}), \tag{3.13}$$

a coordinate–dependent time transformation function $\Omega(..,\mathbf{r}_k,..)$ was adapted in which avoids the masses appear in the time transformation function and therefore usage of the method is convenient for any set of masses. Consider an arbitrary time transformation

$$ds = \Omega(\mathbf{r})dt, \tag{3.14}$$

that is not trivial to solve. With a new auxiliary quantity $\omega = \Omega$ it is possible to write the equations of motion in the form

$$\mathbf{r}^{'} = \frac{\mathbf{v}}{\omega}, \qquad t^{'} = \frac{1}{\omega}, \qquad \mathbf{v}^{'} = \frac{\mathbf{F}}{\Omega} \tag{3.15}$$

where prime indicates d/ds. Therefore, instead of calculating ω explicitly, using the relation $\omega = \Omega$, it could be evaluated by the auxiliary differential equation

$$\dot{\omega} = \mathbf{v} \cdot \frac{\partial\Omega}{\partial\mathbf{r}}. \tag{3.16}$$

In the special case of the Newtonian equations of motion

$$\ddot{\mathbf{r}_k} \equiv \mathbf{F}_k = \sum_{j\neq k} m_j \frac{\mathbf{r}_j - \mathbf{r}_k}{\mathbf{r}_{kj}^3}, \tag{3.17}$$

where $r_{kj} = |\mathbf{r}_j - \mathbf{r}_k|$. Assumption of few-body system, the choice of

$$\Omega = \sum_{i<j} \frac{\Omega_{ij}}{\mathbf{r}_{ij}}, \tag{3.18}$$

seems convenient where Ω_{ij} is an adjustable constant and can be taken as the mass products $\Omega_{ij} = m_i m_j$, or as unity, $\Omega = 1$. This particular function has the advantage that for the problems with very large mass ratios, it does not treat the bodies differently depending on their masses and results in regular equations of motion. Thus the gradient of Ω could be evaluted as

$$\frac{\partial\Omega}{\partial\mathbf{r}_k} \equiv \mathbf{G}_k = \sum_{j\neq k} \Omega_{ij} \frac{\mathbf{r}_j - \mathbf{r}_k}{r_{kj}^3}. \tag{3.19}$$

The corresponding time–transformed equations of motion are given by

$$\mathbf{r}_k^{'} = \frac{\mathbf{v}_k}{\omega}, \qquad t^{'} = \frac{1}{\omega}, \tag{3.20}$$

$$\mathbf{v}_k^{'} = \frac{\mathbf{F}_k}{\Omega}, \qquad \omega^{'} = \frac{1}{\Omega}\sum_k \mathbf{v}_k.\mathbf{G}_k, \tag{3.21}$$

for each particle k. Consequently, the time–transformed leapfrog algorithm can be constructed

$$\mathbf{r}_{1/2} = \mathbf{r}_0 + \frac{h}{2}\frac{\mathbf{v}_0}{\omega_0}, \tag{3.22}$$

$$t_{1/2} = t_0 + \frac{h}{2}\frac{1}{\omega_0}, \tag{3.23}$$

$$\mathbf{v}_1 = \mathbf{v}_0 + h\frac{\mathbf{F}(\mathbf{r}_{1/2})}{\Omega(\mathbf{r}_{1/2})}, \tag{3.24}$$

$$\omega_1 = \omega_0 + h\frac{\mathbf{v}_0 + \mathbf{v}_1}{2\Omega(\mathbf{r}_{1/2})} \cdot \frac{\partial\Omega(\mathbf{r}_{1/2})}{\partial\mathbf{r}_{1/2}}, \tag{3.25}$$

$$\mathbf{r}_1 = \mathbf{r}_{1/2} + \frac{h}{2}\frac{\mathbf{v}_1}{\omega_1}, \tag{3.26}$$

$$t_1 = t_{1/2} + \frac{h}{2}\frac{1}{\omega_1}. \tag{3.27}$$

The present leapfrog algorithm when used with the Gragg–Bulirsch–Stoer (hereafter GBS) extrapolation procedure (Gragg, 1964, 1965; Bulirsch & Stoer, 1966) can be a powerful integrator for few-body calculations.

If one chooses $\Omega = U$ (U is negative of the potential), and substitutes with $\omega = T - E$ (T is the kinetic and E is the total energy), this method could be equivalent to the logarithmic Hamiltonian (logH) technique.

3.2.4 Generalized algorithm regularization

The LogH cannot be a recommendable substitution for regularized methods since it does not use coordinate transformation (KS) and the differential equations are not regularized. Manipulation of the Hamiltonian can adjust the usage of the leapfrog algorithm and extrapolation methods, nevertheless, not sufficient for very close approaches. On the other hand, Time Transformation Leapfrog (TTL) method was introduced to solve the problem of very large mass ratios related in the famous problem of black hole binaries in the galactic nuclei (e.g. the studies of Quinlan & Hernquist (1997); Milosavljevic & Merritt (2001)). Combined with the extrapolation method (Gragg, 1964, 1965; Bulirsch & Stoer, 1966) these regularized algorithms considerably could improve precision. Basically, for utilization of extrapolation method it is necessary that leapfrog algorithm be time–symmetric which is not possible in the case of velocity–dependent perturbations (such as relativistic terms associated in black hole dynamics) except with the help of the implicit midpoint method which still is not very efficient (Mikkola & Merritt, 2006).

To manage this complexity, (Mikkola & Merritt, 2006) decided to eliminate the requirement for the implicit midpoint method by proposing the Generalized Algorithmic Regularization (GAR). The GAR method is a generalization to the well-known modified midpoint method to obtain the required time symmetry so that the algorithmic regularization by the leapfrog can be used and handle forces depend on velocities. The leapfrog provides a regular basic algorithm, allowing the use of extrapolation method.

To review the GAR method in brief, first one should consider a differential equation like

$$\dot{\mathbf{z}} = \mathbf{f}(\mathbf{z}), \tag{3.28}$$

with an approximate solution over a short time interval h,

$$\mathbf{z} \approx \mathbf{z_0} + \mathbf{d}(\mathbf{z_0}, h), \tag{3.29}$$

which can be written in the pair of equations

$$\dot{\mathbf{x}} = \mathbf{f}(\mathbf{y}); \qquad \dot{\mathbf{y}} = \mathbf{f}(\mathbf{x}) \tag{3.30}$$

so that the solution with the choice of initial values $\mathbf{x_0} = \mathbf{y_0} = \mathbf{z_0}$ would be as $\mathbf{x(t)} = \mathbf{y(t)} = \mathbf{z(t)}$. Now the leapfrog–like algorithm can be created

$$\mathbf{x_{1/2}} = \mathbf{x_0} + \frac{h}{2}\mathbf{f}(\mathbf{y_0}), \tag{3.31}$$

$$\mathbf{y_1} = \mathbf{y_0} + hf(\mathbf{x_{1/2}}), \tag{3.32}$$

$$\mathbf{x_1} = \mathbf{x_{1/2}} + \frac{h}{2}\mathbf{f}(\mathbf{y_1}). \tag{3.33}$$

By separating the rise of $\mathbf{y}$ in two procedures and using $\mathbf{d}(\mathbf{z}, h)$ which is more general, one step in the generalized midpoint method can be written

$$\mathbf{x_{1/2}} = \mathbf{x_0} + \mathbf{d}(\mathbf{y_0}, +\frac{h}{2}), \tag{3.34}$$

$$\mathbf{y_{1/2}} = \mathbf{y_0} - \mathbf{d}(\mathbf{x_{1/2}}, -\frac{h}{2}), \tag{3.35}$$

$$\mathbf{y_1} = \mathbf{y_{1/2}} + \mathbf{d}(\mathbf{x_{1/2}}, +\frac{h}{2}), \tag{3.36}$$

$$\mathbf{x_1} = \mathbf{x_{1/2}} - \mathbf{d}(\mathbf{y_1}, -\frac{h}{2}). \tag{3.37}$$

Now we arrive to the formulas that have the time reversibility and is a generalized midpoint algorithm. The extension to N steps can be easily obtain by defining a "subroutine" like $\mathbf{A}(\mathbf{x}, \mathbf{y}, h)$ such that

$$A(\mathbf{x}, \mathbf{y}, h): \quad \mathbf{x} \to \mathbf{x} + \mathbf{d}(\mathbf{y}, +\frac{h}{2}) \tag{3.38}$$

$$\mathbf{y} \rightarrow \mathbf{y} - \mathbf{d}(\mathbf{x}, -\frac{h}{2}) \tag{3.39}$$

and setting $\mathbf{y} = \mathbf{x}$ then repeating $A(\mathbf{x}, \mathbf{y}, h)A(\mathbf{y}, \mathbf{x}, h)$ for N times and finally receiving $\mathbf{x}$ as the result.

To generalize the algorithm to the N–body system, unification of logarithmic Hamiltonian Mikkola & Tanikawa (1999a,c) and Time transformation Leapfrog Mikkola & Aarseth (2002) schemes and attachment of the velocity–dependent forces can be accomplished as follows. First consider the two–body problem with perturbation force depending on the velocity and equations of motion

$$\dot{\mathbf{v}} = -m\frac{\mathbf{r}}{r^3} + \mathbf{f}(\mathbf{r}, t, \mathbf{v}), \tag{3.40}$$

$$\dot{\mathbf{r}} = \mathbf{v}, \tag{3.41}$$

where $\mathbf{r}$ and $\mathbf{v}$ are the position and velocity vectors. Having the binding energy of the two–body system as $b = \frac{m}{r} - \frac{1}{2}\mathbf{v^2}$ and its derivative as $\dot{b} = -\mathbf{v} \cdot \mathbf{f}$, two time transformation equations achieve

$$\frac{dt}{ds} = \frac{1}{\frac{1}{2}\mathbf{v^2} + b}, \tag{3.42}$$

$$\frac{dt}{ds} = \frac{r}{m}. \tag{3.43}$$

Now for the N–body formulation assume the kinetic energy

$$T = \frac{1}{2}\sum_k m_k \mathbf{v_k^2}, \tag{3.44}$$

and the potential energy

$$U = \sum_{i<j} \frac{m_i m_j}{|\mathbf{r_i} - \mathbf{r_j}|}, \tag{3.45}$$

and a coordinate–dependant time transformation function Ω

$$\Omega = \sum_{i<j} \frac{\Omega_{ij}}{|\mathbf{r_i} - \mathbf{r_j}|}. \tag{3.46}$$

If one takes Ω_{ij} as unity, compared with 3.42 and 3.43, the two time transformations for the N–body system is defined

$$t' = \frac{1}{(\alpha T + B)} = \frac{1}{(\alpha U + \beta\Omega + \gamma)}, \tag{3.47}$$

where $B = U - T$ and $E = T - U$ are the binding and total energies, respectively. Moreover, α, β and γ are adjustable constants. Therefore, we have $B = -\alpha E + \beta\Omega + \gamma$ that is gained solving the differential equation

$$\dot{B} = -\alpha \sum_k \mathbf{v}_k \cdot \mathbf{f}_k + \beta \sum_k \frac{\partial \Omega}{\partial \mathbf{r}_k} \cdot \mathbf{v}_k. \tag{3.48}$$

In consequence, the equations of motion that can applied to build the regularized leapfrog, could be obtained as

$$t^{'} = \frac{1}{(\alpha T + B)}, \tag{3.49}$$

$$\mathbf{r}_k^{'} = t^{'}\mathbf{v}_k, \tag{3.50}$$

$$\tau^{'} = \frac{1}{(\alpha U + \beta\Omega + \gamma)}, \tag{3.51}$$

$$\mathbf{v}_k^{'} = \tau^{'}(\frac{\partial U}{\partial \mathbf{r}_k} + \mathbf{f}_k)/m_k, \tag{3.52}$$

$$B^{'} = \tau^{'}\sum_k(-\alpha\mathbf{f}_k + \beta\frac{\partial\Omega}{\partial\mathbf{r}_k})\cdot\mathbf{v}_k, \tag{3.53}$$

where $\mathbf{r}_k$ and $\mathbf{v}_k$ are the position and velocity of the mass m_k.

3.2.5 Explicit algorithmic regularization

The Implicit and generalized midpoint algorithms (Mikkola & Merritt, 2006, 2008b; Harfst et al., 2008) have been demonstrated to successfully time-symmetrize the algorithmic regularization leapfrog even when the the equations of motion contain velocity–dependent forces such as relativistic terms. Therefore, employment of the extrapolation method could be authorized. The implicit midpoint method may still be better, when the perturbations are petite, and the generalized midpoint method can be efficient only when the velocity dependence of the forces is significant, nonetheless computationally expensive.

Hellström & Mikkola (2010) introduced a new scheme that uses an auxiliary velocity algorithm, dubbed as the auxiliary–velocity algorithm or AVA for short. It provides a time–symmetric regularization algorithm for the few–body problem with velocity–dependent perturbations, but it is fully explicit. It has the ability to be exerted either on its own or within extrapolation methods.

Thereupon, the new integrator links the basic leapfrog and the modified midpoint for velocity–dependent and/or time–dependent perturbations through an auxiliary velocity.

Consider the equations of motion

$$\dot{\mathbf{r}} = \mathbf{v}, \tag{3.54}$$

$$\dot{\mathbf{v}} = \mathbf{A}(\mathbf{r}, \mathbf{v}), \tag{3.55}$$

where usually $\mathbf{A}(\mathbf{r}, \mathbf{v}) = \mathbf{A}_0(\mathbf{r}) + \mathbf{a}(\mathbf{r}, \mathbf{v})$ with $\mathbf{A}_0(\mathbf{r})$ as the unperturbed part . For this set of equations, usage of the implicit midpoint method would be computationally expensive and not recommended. On the other hand, if one defines an auxiliary velocity $\mathbf{w}$ such that the equations of motion in the extended parameter space $(\mathbf{r}, \mathbf{v}, \mathbf{w})$ could be illustrated as

$$\dot{\mathbf{r}} = \mathbf{v}, \tag{3.56}$$

$$\dot{\mathbf{w}} = \mathbf{A}(\mathbf{r}, \mathbf{v}), \tag{3.57}$$

$$\dot{\mathbf{v}} = \mathbf{A}(\mathbf{r}, \mathbf{w}), \tag{3.58}$$

thus the leapfrog-like explicit algorithm can be constructed simply because the righthand side variables of these equations do not depend on the left hand sides. If the initial values are set $\mathbf{w_0} = \mathbf{v_0}$, one leapfrog integration step ould be carried out as

$$\mathbf{r}_{1/2} = \mathbf{r}_0 + \frac{h}{2}\mathbf{v}_0, \tag{3.59}$$

$$\mathbf{w}_{1/2} = \mathbf{v}_0 + \frac{h}{2}\mathbf{A}(\mathbf{r}_{1/2}, \mathbf{v}_0), \tag{3.60}$$

$$\mathbf{v}_1 = \mathbf{v}_0 + h\mathbf{A}(\mathbf{r}_{1/2}, \mathbf{w}_{1/2}), \tag{3.61}$$

$$\mathbf{w}_1 = \mathbf{w}_{1/2} + \frac{h}{2}\mathbf{A}(\mathbf{r}_{1/2}, \mathbf{v}_1), \tag{3.62}$$

$$\mathbf{r}_1 = \mathbf{r}_{1/2} + \frac{h}{2}\mathbf{v}_1. \tag{3.63}$$

This leapfrog algorithm is explicit and time–symmetric in the extended space of variables with the capability to work in any extrapolation algorithm.

To operate it in the N–body system, it is useful to star with the perturbed two–body problem reduced equations of motion

$$\ddot{\mathbf{r}} = -\frac{\mu\mathbf{r}}{r^3} + \epsilon\mathbf{a}(t, \mathbf{r}, \mathbf{v}), \tag{3.64}$$

where $\mathbf{a}$ is a general perturbation acceleration depending also on time, μ and ϵ are the gravitational and perturbation parameters, respectively. With the assumption

$$ds = U(\mathbf{r})dt, \tag{3.65}$$

for the time transformation, the algorithmic regularization is generated

$$\mathbf{r}^{'} = \mathbf{v}/T_B, \tag{3.66}$$

$$\mathbf{v}^{'} = [\mathbf{A}(\mathbf{r}) + \epsilon\mathbf{a}(t, \mathbf{r}, \mathbf{v})]/U, \tag{3.67}$$

$$\mathbf{w}^{'} = [\mathbf{A}(\mathbf{r}) + \epsilon\mathbf{a}(t, \mathbf{r}, \mathbf{w})]/U, \tag{3.68}$$

with $T_B(\mathbf{v}) = T + B = U(\mathbf{r})$. Besides, for the binding energy ($B = U - T$) we have

$$B^{'} = -\epsilon < \mathbf{v}, \mathbf{a}(t, \mathbf{r}, \mathbf{v}) > /U, \tag{3.69}$$

where $< ., . >$ indicates Euclidean inner product.

Accordingly, the formulation for the N–body system is directly. As usual, the kinetic energy $T = \frac{1}{2}\sum_{i=1}^{N} m_i||\mathbf{v}_i||^2$ and the potential energy $U = \frac{1}{2}\sum_{i\neq j}\frac{m_i m_j}{\mathbf{r_{ij}}}$. Hence,

$$\begin{aligned}\ddot{\mathbf{r}_i} &= \nabla U/m_i + \epsilon\mathbf{a}_i(t, \mathbf{R}_i, \mathbf{v}_i)\\ &\equiv \mathbf{A}_i(\mathbf{R}_i) + \epsilon\mathbf{a}_i(t, \mathbf{R}_i, \mathbf{v}_i),\end{aligned} \tag{3.70}$$

demonstrates the equation of motion for the ith mass and $\mathbf{R}_i = (\mathbf{r}_{i1}, ..., \mathbf{r}_{iN})$. As before, the time transformation is

$$ds = Udt. \tag{3.71}$$

As a result, we can write

$$\mathbf{r}_i^{'} = \mathbf{v}_i/T_B, \tag{3.72}$$

$$\mathbf{v}_i^{'} = [\mathbf{A}_i(\mathbf{R}_i) + \epsilon\mathbf{a}_i(t, \mathbf{R}_i, \mathbf{v}_i)]/U, \tag{3.73}$$

$$\mathbf{w}_i^{'} = [\mathbf{A} - i(\mathbf{R}_i) + \epsilon\mathbf{a}_i(t, \mathbf{r}_i, \mathbf{w} - i)]/U, \tag{3.74}$$

$$B^{'} = -\epsilon\sum_{i=1}^{N} m_i < \mathbf{v} - i, \mathbf{a} - i(t, \mathbf{R}_i, \mathbf{v}_i) > /U. \tag{3.75}$$

where as before, $T_B(\mathbf{v}) = T + B = U(\mathbf{r})$ and $B = U - T$ is the binding energy.

3.2.6 Algorithmic regularization chain

This section discusses about the configuration of the Algorithmic Regularization Chain, abbreviated as AR–CHAIN, which is the main algorithm of the `AR-CHAIN` code we used in our works. Structure of the algorithm is composed of three main ingredients; the chain, time transformation and extrapolation method (Mikkola, 2008a,b). Subsequently, the integrator is a mixture of the chain, LogH and TTL schemes, discussed in the previous sections. In fact, the precedence of the code is its emphasis on the chain structure which in analogy with the old regularization routines, considerably decreases the roundoff errors. Taking advantage of a time transformation along with the leapfrog algorithm, this code regularizes the equations of motion and allows the utilization of extrapolation method for enhancement of accuracy. Since leapfrog creates the time symmetry that is a convenient situation for an efficient extrapolation exertion, constructing the adaptable leapfrog is an important part of this integrator.

The algorithm begins with forming and collecting the chain coordinates $\mathbf{X}_k = \mathbf{r}_{ik} - \mathbf{r}_{jk}$ and chain velocities $\mathbf{V}_k = \mathbf{v}_{ik} - \mathbf{v}_{jk}$. The Newtonian equation of motion read

$$\dot{\mathbf{X}} = \mathbf{V}, \tag{3.76}$$

$$\dot{\mathbf{V}} = \mathbf{A}(\mathbf{X}) + \mathbf{f}, \tag{3.77}$$

where $\mathbf{A}$ is the N–body acceleration with probable external effects $\mathbf{f}$ due to other bodies.

The basic Hamiltonian is written

$$H = T - U = \frac{1}{2}\sum_k m_k \mathbf{v}_k^2 - \sum_{i<j} \frac{m_i m_j}{|\mathbf{r}_{ij}|}. \tag{3.78}$$

The time transformation function could be

$$\Omega(\mathbf{r}) = \sum_{i<j} \frac{\Omega_{ij}}{|\mathbf{r}_{ij}|}, \tag{3.79}$$

where Ω is a coordinate–dependent time transformation function (Mikkola & Aarseth, 2002). Therefore, having the new independent variable$s$ and $ds = \Omega(\mathbf{r})dt$, the two equivalent time transformation can be written (Mikkola & Merritt, 2006)

$$t^{'} = \frac{dt}{ds} = 1/(\alpha T + B) = 1/(\alpha U + \beta\Omega + \gamma), \tag{3.80}$$

where α, β and γ are adjustable constants. If one considers the auxiliary quantity ω as

$$\dot{\omega} = \frac{\partial \Omega}{\partial \mathbf{X}} \cdot \mathbf{V}, \tag{3.81}$$

with the initial value $\omega(0) = \Omega(0)$, the value of ω is determined (Mikkola & Aarseth, 2002). Then similar to 3.80 we have

$$ds = [\alpha(T + B) + \beta\omega + \gamma]dt = [\alpha U + \beta\Omega + \gamma]. \tag{3.82}$$

The corresponding equations of motion that can be derived to construct the leapfrog are

$$t^{'} = 1/(\alpha(T + B) + \beta\omega + \gamma), \tag{3.83}$$

$$\mathbf{X}^{'} = t^{'}\mathbf{V}, \tag{3.84}$$

for the coordinates, and

$$\tilde{t^{'}} = 1/(\alpha U + \beta\Omega + \gamma), \tag{3.85}$$

$$\mathbf{V}^{'} = \tilde{t^{'}}(\mathbf{A} + \mathbf{f}), \tag{3.86}$$

$$\omega^{'} = \tilde{t^{'}}\frac{\partial\Omega}{\partial\mathbf{X}} \cdot \mathbf{V}, \tag{3.87}$$

$$B^{'} = -\tilde{t^{'}}\frac{\partial T}{\partial\mathbf{V}} \cdot f, \tag{3.88}$$

for the velocities. Further, as mentioned before, the extrapolation can be applied to increase the precision.

It is possible to solve the problem when acceleration $\mathbf{f}$ is a velocity–dependent perturbation, $\mathbf{f} = \mathbf{f}(\mathbf{X}, \mathbf{V})$, for instance if one takes into account the role of Post-Newtonian terms in simulations of black hole dynamics (Mikkola & Merritt, 2006, 2008b). In this case, the operative leapfrog routines for the chain coordinates and velocities, respectively, are

$\mathbf{X}(s)$:

$$\delta t = s/(\alpha(T + B) + \beta\omega + \gamma) \tag{3.89}$$

$$t = t + \delta t \tag{3.90}$$

$$\mathbf{X} \rightarrow \mathbf{X} + \delta t\mathbf{V} \tag{3.91}$$

$\mathbf{V}(s)$:

$$\tilde{\delta t} = s/(\alpha U + \beta\Omega + \gamma) \tag{3.92}$$

$$\mathbf{V} \rightarrow \mathbf{V} + \tilde{\delta t}(\mathbf{A} + \mathbf{f}) \tag{3.93}$$

$$B \to B + \tilde{\delta t}\langle \frac{\partial T}{\partial \mathbf{V}} \rangle \cdot \mathbf{f} \tag{3.94}$$

$$\omega \to \omega + \tilde{\delta t}\frac{\partial \Omega}{\partial \mathbf{X}} \cdot \langle \mathbf{V} \rangle \tag{3.95}$$

the averages of the initial and final $\mathbf{V}$'s are shown with $\langle \frac{\partial T}{\partial \mathbf{V}} \rangle$ and $\langle \mathbf{V} \rangle$.

For the above mapping, when the extrapolation is employed, n leapfrog steps is applied as

$$\mathbf{X}(h/2)[\mathbf{V}(h)][\prod_{\nu=1}^{n-1}(\mathbf{V}(h)\mathbf{X}(h)]\mathbf{V}(h)\mathbf{X}(h/2). \tag{3.96}$$

The distinction of the `AR-CHAIN` code is that the code could be applicable for arbitrary mass ratios. Different alternatives for (α, β, γ) lead to various implementation of the code. The choice of $(\alpha, \beta, \gamma) = (1, 0, 0)$ would execute the logarithmic Hamiltonian (logH) method (Mikkola & Tanikawa, 1999a,c; Preto & Tremaine, 1999) which provides a kind of regularization without coordinate transformation, which produces exact trajectories for Newtonian two-body motion. If one selects $(\alpha, \beta, \gamma) = (0, 1, 0)$ then the time transformation leapfrog method (TTL) is accomplished that can handle large mass ratios and regular results for close encounters involving arbitrary numbers of bodies. The option $(\alpha, \beta, \gamma) = (0, 0, 1)$ brings about the normal basic leapfrog. Furthermore, the post–Newtonian terms i.e. velocity–dependent forces (Mikkola & Merritt, 2006, 2008b) could be activated and in company with TTL method a good combination for investigating the dynamics of supermassive black holes (SMBHs) in galactic nuclei.

3.2.7 Algorithmic regularization chain with the post–Newtonian approach

The `AR-CHAIN` algorithm, integrates the equations of motion of the small N–body system by means of algorithmic regularization (Mikkola & Tanikawa, 1999a,c), executed with a chain configuration (Mikkola & Aarseth, 1993) and the time transformation leapfrog (Mikkola & Aarseth, 2002).

For the numerical study of particles orbiting a central massive object, Velocity-dependent forces were included via a generalized midpoint method based on the leapfrog algorithm, perfectly suited as in the case of the Galactic Center (GC) stars around the Supermassive black hole (SMBH) (Mikkola & Merritt, 2006). To date, results for the orbital motion accurate through 3.5 post–Newtonian (3.5PN) order are known (Mora & Will, 2004; Jaranowski & Schäfer, 1998; Pati & Will, 2002). The version of the `AR-CHAIN` code that we have employed for the calculations, also incorporates pairwise post–Newtonian forces of orders up to and including 3.5PN (Mora & Will, 2004). The parametrized post–

newtonian formalism for the general relativistic force per unit mass is given by (Soffel, 1989)

$$\mathbf{a} = \underbrace{\mathbf{a}_0}_{\text{Newtonian}} + \underbrace{\underbrace{c^{-2}\mathbf{a}_2}_{\text{1PN}} + \underbrace{c^{-4}\mathbf{a}_4}_{\text{2PN}}}_{\text{pericentre shift}} + \underbrace{\underbrace{c^{-5}\mathbf{a}_5}_{\text{2.5PN}}}_{\text{GW}} + \underbrace{c^{-6}\mathbf{a}_6}_{\text{3PN}} + \underbrace{c^{-7}\mathbf{a}_7}_{\text{3.5PN}}, \tag{3.97}$$

where $\mathbf{a}$ is the acceleration of particle 1, $\mathbf{a}_0$ is the Newtonian acceleration and c expresses the speed of light in vacuum. The notation nPN represents the nth post-Newtonian correction to Newtonian gravity. 1PN and 2PN corrections are responsible for the pericentre shift (Kupi et al., 2006; Amaro-Seoane, 2018) and 2.5PN terms denote the energy loss via gravitation waves. Moreover, the equations of motion are conservative up to the 2PN level and the first non–conservative effect occurs only at 2.5PN order, associated with the gravitational radiation emission (Blanchet, 2014). We have implemented 1PN, 2PN and 2.5PN terms for a non-spinning SMBH added to the Newtonian acceleration. Relativistic flattening plays no role through 3PN order (Pati & Will, 2002) and the first post–Newtonian correction to radiation reaction appears at 3.5 order (Galley et al., 2012) which are excluded in our computations.

If we write the equations of motion in the standard form of "Newtonian–like" manner, the acceleration of body 1 is given schematically by

$$\begin{split}\mathbf{a}_1 = \frac{d^2\mathbf{x}_1}{dt^2} = \frac{m_2}{r^2}\{\mathbf{n}[-1 + (1PN) + (2PN) + (2.5PN) + (3PN) + (3.5PN) + ...]+ \\ \mathbf{v}[(1PN) + (2PN) + (2.5PN) + (3PN) + (3.5PN) + ...]\},\end{split} \tag{3.98}$$

where the position and mass of the body i is indicated as $\mathbf{x}_i$ and m_i, the unit vector from body 2 to 1 is $\mathbf{n} = (\mathbf{x}_1 - \mathbf{x}_2)/r$ with r as the separation of two bodies and the relative velocity is $\mathbf{v} = \mathbf{v}_1 - \mathbf{v}_2$ (switching $1 \rightleftharpoons 2$ the equation for body 2 is achieved, (Mora & Will, 2004)). The best way to write a set of equations of motion in terms of the relative coordinates, is to first reduce the two–body problem to one–body problem by setting the centre of mass of the system as the origin, then convert all the variables to relative coordinates, $\mathbf{x} = \mathbf{x}_1 - \mathbf{x}_2$, having

$$\mathbf{x}_1 = [m_2/m + (\eta\delta m/2m)(v^2 - m/r) + (2PN) + ...]\mathbf{x}, \tag{3.99a}$$

$$\mathbf{x}_2 = [-m_1/m + (\eta\delta m/2m)(v^2 - m/r) + (2PN) + ...]\mathbf{x}, \tag{3.99b}$$

where the reduced mass is $\eta = \mu/m = m_1 m_2/m^2$ and $\delta m = m_1 - m_2$. The results will be as

$$\mathbf{a} = \frac{d^2\mathbf{x}}{dt^2} = \frac{m}{r^2}[(-1 + A)\mathbf{n} + B\mathbf{v}], \tag{3.100}$$

where A and B illustrate the post–Newtonian contributions. For $A = A_1 + A_2 + \ldots$ and $B = B_1 + B_2 + \ldots$ in an appropriate harmonic gauge, Blanchet & Iyer (2003) derived

$$A_1 = 2(2+\eta)\frac{m}{r} - (1+3\eta)v^2 + \frac{3}{2}\eta\,\dot{r}^2, \tag{3.101a}$$

$$\begin{aligned} A_2 = &-\frac{3}{4}(12+29\eta)\left(\frac{m}{r}\right)^2 - \eta(3-4\eta)v^4 \\ &- \frac{15}{8}\eta(1-3\eta)\dot{r}^4 + \frac{1}{2}\eta(13-4\eta)\frac{m}{r}v^2 \\ &+ (2+25\eta+2\eta^2)\frac{m}{r}\dot{r}^2 + \frac{3}{2}\eta(3-4\eta)v^2\dot{r}^2, \end{aligned} \tag{3.101b}$$

$$A_{2.5} = \frac{8}{5}\eta\frac{m}{r}\dot{r}\left(\frac{17}{3}\frac{m}{r} + 3v^2\right), \tag{3.101c}$$

$$\begin{aligned} A_3 = &[16 + \left(\frac{1399}{12} - \frac{41}{16}\pi^2\right)\eta + \frac{71}{2}\eta^2]\left(\frac{m}{r}\right)^3 + \eta[\frac{20827}{840} + \frac{123}{64}\pi^2 - \eta^2]\left(\frac{m}{r}\right)^2 v^2 \\ &- [1 + \left(\frac{22717}{168} + \frac{615}{64}\pi^2\right)\eta + \frac{11}{8}\eta^2 - 7\eta^3]\left(\frac{m}{r}\right)^2\dot{r}^2 - \frac{1}{4}\eta(11-49\eta+52\eta^2)v^6 + \frac{35}{16}\eta(1-5\eta+5\eta^2)\dot{r}^6 \\ &- \frac{1}{4}\eta(75+32\eta-40\eta^2)\frac{m}{r}v^4 - \frac{1}{2}\eta(158-69\eta-60\eta^2)\frac{m}{r}\dot{r}^4 + \eta(121+16\eta-20\eta^2)\frac{m}{r}v^2\dot{r}^2 \\ &+ \frac{3}{8}\eta(20-79\eta+60\eta^2)v^4\dot{r}^2 - \frac{15}{8}\eta(4-18\eta+17\eta^2)v^2\dot{r}^4, \end{aligned} \tag{3.101d}$$

$$\begin{aligned} A_{3.5} = &-\frac{8}{5}\eta\frac{m}{r}\dot{r}[\frac{23}{14}(43+14\eta)\left(\frac{m}{r}\right)^2 + \frac{3}{28}(61+70\eta)v^4 \\ &+ 70\dot{r}^4 + \frac{1}{42}(519-1267\eta)\frac{m}{r}v^2 \\ &+ \frac{1}{4}(147+188\eta)\frac{m}{r}\dot{r}^2 - \frac{15}{4}(19+2\eta)v^2\dot{r}^2], \end{aligned} \tag{3.101e}$$

and

$$B_1 = 2(2-\eta)\dot{r}, \tag{3.102a}$$

$$\begin{aligned} B_2 = &-\frac{1}{2}\dot{r}[(4+41\eta+8\eta^2)\frac{m}{r} - \eta(15+4\eta)v^2 \\ &+ 3\eta(3+2\eta)\dot{r}^2], \end{aligned} \tag{3.102b}$$

$$B_{2.5} = -\frac{8}{5}\eta\frac{m}{r}(3\frac{m}{r} + v^2), \tag{3.102c}$$

$$\begin{aligned}B_3 = \dot{r}\{[4 + \left(\frac{5849}{840} + \frac{123}{32}\pi^2\right)\eta - 25\eta^2 - 8\eta^3]\left(\frac{m}{r}\right)^2 \\ + \frac{1}{8}\eta(65 - 152\eta - 48\eta^2)v^4 + \frac{15}{8}\eta(3 - 8\eta - 2\eta^2)\dot{r}^4 \\ + \eta(15 + 27\eta + 10\eta^2)\frac{m}{r}v^2 - \frac{1}{6}\eta(329 + 177\eta + 108\eta^2)\frac{m}{r}\dot{r}^2 \\ - \frac{3}{4}\eta(16 - 37\eta - 16\eta^2)v^2\dot{r}^2\},\end{aligned} \tag{3.102d}$$

$$\begin{aligned}B_{3.5} = \frac{8}{5}\eta\frac{m}{r}[\frac{1}{42}(1325 + 546\eta)\left(\frac{m}{r}\right)^2 + \frac{1}{28}(313 + 42\eta)v^4 + 75\dot{r}^4 \\ - \frac{1}{42}(205 + 777\eta)\frac{m}{r}v^2 + \frac{1}{12}(205 + 424\eta)\frac{m}{r}\dot{r}^2 - \frac{3}{4}(113 + 2\eta)v^2\dot{r}^2].\end{aligned} \tag{3.102e}$$

We define the dimensionless spin angular momentum of a black hole, χ, that can have any value between zero and the maximum value allowed by the Kerr solution (Kerr, 1963), which as a vector is described like

$$\mathbf{J} = \chi\left(\frac{GM_{\bullet}^2}{c}\right), \qquad 0 \le \chi \le 1 \tag{3.103}$$

where G is the gravitational constant and $M_{\bullet}$ is the mass of the black hole. In the weak–field and low–velocity limit, the spin of an SMBH has an additional nonradial acceleration due to its nonsphericity, which is described in terms of the relativistic quadrupole moment $\mathcal{Q}$, and the standard (no–hair) relation between J and $\mathcal{Q}$ is

$$\mathcal{Q} = -\frac{1}{c}\frac{J^2}{M_{\bullet}}. \tag{3.104}$$

In the covariant spin supplementary condition gauge (Kidder, 1995), the lowest–order contributions of the SMBH's spin–related, N–body accelerations $\mathbf{a}_J$ is written (Merritt et al., 2010)

$$\mathbf{a}_{J,1} = -\frac{3G^2M_{\bullet}}{c^3}\sum_{j\neq 1}\frac{m_j}{r_{1j}^3}\left\{[\mathbf{v}_{1j} - (\mathbf{n}_{1j}\cdot\mathbf{v}_{1j})\mathbf{n}_{1j}]\times\chi - 2\mathbf{n}_{1j}(\mathbf{n}_{1j}\times\mathbf{v}_{1j})\cdot\chi\right\}, \tag{3.105a}$$

$$\mathbf{a}_{J,j} = \frac{2G^2M_{\bullet}^2}{c^3r_{1j}^3}\left\{[2\mathbf{v}_{1j} - 3(\mathbf{n}_{1j}\cdot\mathbf{v}_{1j})\mathbf{n}_{1j}]\times\chi - 3\mathbf{n}_{1j}(\mathbf{n}_{1j}\times\mathbf{v}_{1j})\cdot\chi\right\}, \tag{3.105b}$$

$$\dot{\chi} = \frac{G}{2c^2}\sum_{j\neq i}\frac{m_j}{r_{ij}^2}[\mathbf{n}_{1j}\times(3\mathbf{v}_1 - 4\mathbf{v}_j)]\times\chi, \tag{3.105c}$$

where SMBH is the first particle and all the other particles are in the range $2 \le j \le N$. Moreover, we have $r_{ij} \equiv |\mathbf{x}_i - \mathbf{x}_j|$, $\mathbf{x}_{ij} \equiv \mathbf{x}_i - \mathbf{x}_j$, $\mathbf{n}_{ij} = \mathbf{x}_{ij}/r_{ij}$ and $\mathbf{v}_{ij} \equiv \mathbf{v}_i - \mathbf{v}_j$.

It is interesting to note that the acceleration due to the quadrupole moment does not come out of the post-Newtonian expansion, at any order, since those equations are derived under the assumption that the bodies are point masses (Merritt, 2013). the quadrupole term read as (Merritt et al., 2010)

$$\mathbf{a}_{\mathcal{Q},j} = +\frac{3}{2}\chi^2\frac{G^3}{c^4}\frac{M_{\bullet}^3}{r^4}\left[5\mathbf{n}_{1j}(\mathbf{n}_{1j}\cdot\hat{\mathbf{J}})^2 - 2(\mathbf{n}_{1j}\cdot\hat{\mathbf{J}})\hat{\mathbf{J}} - \mathbf{n}_{1j}\right], \qquad \hat{\mathbf{J}} \equiv \mathbf{J}/J. \tag{3.106}$$

Accordingly, the equation of motion for the jth particle has the additional spin–related accelerations and quadrupole terms (`AR-CHAIN`) as

$$\mathbf{a} = \frac{m}{r^2}[(-1 + A)\mathbf{n} + B\mathbf{v}] - (\mathbf{a}_J - \mathbf{a}_Q). \tag{3.107}$$

3.3 The `ARGdf` code

The `AR-CHAIN` code is an accurate, direct N–body algorithm suitable to explore the non–relativistic or relativistic dynamics of few–body systems near a compact massive object such as an SMBH. However, exact integration of the evolution of Intermediate–mass black holes (IMBHs) and stellar black holes or even stars (planets) in a few parsec scale requires a formalism that allows modelling a whole galaxy nucleus as well as the dynamical friction on orbiting objects. For this reason, our simulations are performed using `ARGdf` (Arca-Sedda & Capuzzo-Dolcetta, 2019), an extension of the `AR-CHAIN` code developed to take into account both the gravitational field of the galaxy, treated either as a Dehnen (1993) or a Plummer (1911) analytic field, and the dynamical friction effect treated as an extension of Chandrasekhar (1943) theory.

Dehnen models with the density profiles

$$\rho_D(r) = \frac{(3-\gamma)M_D}{4\pi}\frac{a}{r^\gamma(r+a)^{4-\gamma}}, \tag{3.108}$$

where a is a scaling radius and M_D the total mass, and corresponding potential

$$\Phi_D(r) = \frac{GM_D}{a} \times \begin{cases} -\frac{1}{2-\gamma}\left[1 - (\frac{r}{r+a})^{2-\gamma}\right] & \gamma \neq 2 \\ ln\frac{r}{r+a} & \gamma = 2, \end{cases} \tag{3.109}$$

provide reasonable models of the centres of elliptical galaxies (Binney & Tremaine, 1987). Besides, the Plummer model, with the density profile

$$\rho_P(r) = \frac{3M_P}{4\pi}\frac{b^2}{(b^2+r^2)^{5/2}}, \tag{3.110}$$

where b is a length scale and M_p is the model mass, and associated potential

$$\Phi_P(r) = -\frac{GM_P}{(r^2+b^2)^{1/2}}, \tag{3.111}$$

represents the properties of spherical systems which the density near their centre is almost constant, and falls to zero at large radii (Binney & Tremaine, 1987).

To include contributions due to these external potentials, one must calculate their accelerations, as the accelerations exerted from some perturbers, and add them to the N–body accelerations. Further, if a point–like body of mass M and velocity v_M traveling through a homogeneous sea of field stars with overall density ρ, the exerted dynamical friction due to the encounters of the subject body and the field stars will decelerate the subject body at a rate

$$\frac{d\mathbf{v}_M}{dt} \simeq -4\pi^2 G^2 M ln\Lambda \rho \frac{\mathbf{v}_M}{v_M^3}, \tag{3.112}$$

as first discovered by Chandrasekhar (1943). Note that in 3.112 field stars move with slower velocities than the subject body. If the galactic distribution function is Maxwellian with dispersion σ, the dynamical friction term is written

$$\frac{d\mathbf{v}_M}{dt} = -4\pi G^2 M ln\Lambda \rho \left[erf(X) - \frac{2X}{\sqrt{\pi}} e^{-X^2} \right] \frac{\mathbf{v}_M}{v_M^3}, \tag{3.113}$$

where $X \equiv v_M/\sqrt{2}\sigma$ and erf is the error function (Binney & Tremaine, 1987). Nonetheless, Chandrasekhar (equations 3.112 and 3.113) overestimates the dynamical friction rate since at low velocities, whenever the subject body is very slow, the term $|dv_M/dt| \to \infty$. Arca-Sedda & Capuzzo-Dolcetta (2019) refined the standard Chandrasekhar formula to provide an optimal imitation of the local approximation formula. In order to represent the effect of dynamical friction properly, the dynamical friction term in equation 3.112 is multiplied by a *shape function* as

$$\mathcal{L} = \left[1 + \left(\frac{\rho_{bh,i}}{\rho_g(r)} \right) \right] D(M_{tot}, \mu tot), \tag{3.114}$$

which prevents the velocity of the subject body approaches zero. Here, ρ_g and $\rho_{bh,i} = M_i/R_i^3$ are the galaxy density and corrective factor, respectively, where

$$R_i = r_g \frac{(M_i/M_g)^{1/(3-\gamma)}}{1-(M_i/M_g)^{1/(3-\gamma)}}, \tag{3.115}$$

indicates the so–called stalling radius, i.e. the distance in which dynamical friction ceases because there is no net momentum transfer between the background particles and the subject particle (Read et al., 2006; Antonini et al., 2011). the other term in equation 3.114 represents the total (M_tot) and reduced masses (μ_{tot}) of the subject bodies

$$D(M_{tot}, \mu tot) = \frac{1}{20}(N-1)\left(\frac{M_{tot}}{\mu_{tot}} \right)^{1/3}. \tag{3.116}$$

In addition, the velocity of the subject mass (v_M) is replaced with ($v_M + \sigma_{tot}$) with

$$\sigma_{tot}^2 = \frac{GM_g(r)}{r} + \frac{GM_i}{R_i}. \tag{3.117}$$

again to avoid the velocity approaches zero (Webb et al., 2019).

Chapter 4

Dynamics of binary stars with planets approching Sgr A*

Our Galaxy hosts a very massive object at its centre often referred to the supermassive black hole Sgr A*. Its gravitational tidal field is likely so intense to strip apart a binary star passing in its vicinity, so accelerate one of the components as hypervelocity star (HVS) and grab the other star around Sgr A* as S-star. Taking into account that many binary star systems are known to host planets, in this chapter, we aim to broaden the study of the violent dynamics in the Galactic centre to the close interplay of binary stars and their planetary systems with Sgr A* to provide a reliable estimate of likelihood to find high velocity stars with planets around. Results are obtained via high precision numerical integrations including post-Newtonian terms.

Such work has been initiated by Ginsburg & Loeb (2006) who examined the fate of former binary companions by simulating 600 different binary orbits around Sgr A* with a direct summation N-body code. Antonini et al. (2010) have studied binary-SMBH encounters and the inclination excitation and eccentricity chaos due to Kozai–Lidov mechanism leading to collisions and mergers of binary stars. Later, Ginsburg et al. (2012) have extended their previous work performing a series of simulations of binary stars with planets interacting with Sgr A* black hole, interesting although not conclusive because obtained with a code that does not provide sufficient accuracy for close encounters of objects where the mass ratio (SMBH to planet) is $\approx 10^9$, and does not account for relativistic effects. On another side, Fragione & Ginsburg (2017) found that the likelihood of finding exoplanets around high-velocity stars by the transit method depends mainly on mean planetary inclinations and eccentricities (increasing with eccentricity and decreasing with inclination). They computed the probability of a multi-planetary transit and found it in the range $10^{-3} < P < 10^{-1}$ yr^{-1}. Their prediction is that in order to spot a transit it is needed to observe $\sim 10 - 1000$ stars. We underline here that while, at the present time, the exploration of a solitary, super fast and distant hypervelocity planet (HVP) is challenging, gravitational microlensing could be a suitable technique to use to detect, indirectly, the presence of small exoplanets at significant distances from the Earth.

Our study shows what is the quantitative likelihood to disrupt a binary star system upon different initial conditions. The same is convincing for stripping apart planets from their host stars leaving them as wandering planets, even as HVPs, or keeping them bound to their primary star. Also, planets could be swallowed by their host star. The actual possibility of observational counterpart deserves further investigation. Hereinafter we describe the methodology we employed for our five-body (a binary star, where both of the components host a revolving planet, and the SMBH) simulations and the choice of initial conditions for our runs.

4.1 Model and methods

Studying the close interaction of stars and planets with the SMBH is a tough numerical task due to the enormous mass ratio involved ($\gtrsim 10^9$) which would make almost impossible to follow numerically the planet orbits during the close interaction with the SMBH if using standard integration schemes. To do it in a proper, reliable, way we carried out our simulations using a regularized N-body code, the `AR-CHAIN` integrator (Mikkola & Tanikawa, 1999b; Mikkola & Merritt, 2008a), which includes, also, post-Newtonian (PN) corrections up to order 2.5, properly modified to consider an analytic external potential and its dynamical friction (`ARGdf`code, see Arca-Sedda & Capuzzo-Dolcetta (2019)).

Actually, a proper modelization of the GC environment, at least when not too narrow space scales are considered, is needed, so we took into account the local distribution of stars in the form of a regular external potentials which also induces dynamical friction on orbiting objects.

To model the Galaxy density profile in spherical symmetry, we use the sum of a Dehnen (1993) and a Plummer (1911) distribution:

1. the galactic background is represented with a Dehnen's (or γ) whose density profile is

$$\rho_D(r) = \frac{(3-\gamma)M_D}{4\pi}\frac{a}{r^\gamma(r+a)^{4-\gamma}}, \tag{4.1}$$

   where a is a length scale, M_D is the total mass, and $0 \leq \gamma < 3$ is a parameter to adjust the steepness of the profile. For our model, we choose $M_D = 10^{11}$ $\mathrm{M}_\odot$, a=2 kpc and $\gamma = 0.1$, like in Arca-Sedda & Capuzzo-Dolcetta (2017);

2. to model the nuclear star cluster (NSC) around the GC, we use a Plummer density profile

$$\rho_P(r) = \frac{3M_P}{4\pi}\frac{b^2}{(b^2+r^2)^{5/2}}, \tag{4.2}$$

   where b is a length scale and M_p is the model mass. Following Schödel et al. (2014) we adopted $M_p = 2.5 \pm 0.4 \times 10^7 M\odot$ and $b = 4$ pc.

We set mass $M_\bullet = 4 \times 10^6 M_\odot$ to the putative SMBH in the origin of the reference frame.

In this work, we studied the orbital evolution of a binary system, each component of which has a planet orbiting around, at varying initial conditions in the Galactic central region as modelled above. As we said, the basic idea to originate high- and even hyper-velocity stars is due to Hills (1988); a binary, moving on a low energy (E) orbit, approaches closely an MBH well within its sphere of influence where it experiences a 3-body interaction. If an exchange collision occurs, the ejection velocity, is given approximately by

$$v_{ej} \approx 1800 \left(\frac{a_*}{0.1\mathrm{AU}}\right)^{-1/2} \left(\frac{m_{bin}}{2M_\odot}\right)^{1/3} \left(\frac{M_\bullet}{4\times 10^6 M_\odot}\right)^{1/6} \mathrm{kms}^{-1}, \tag{4.3}$$

where a_* and m_{bin} are the separation and total mass of the stars in the binary. Note that this velocity is the velocity at infinity of the ejected star in the absence of the Galactic potential (Merritt, 2013). Due to the energy conservation for the 3-body (binary star + SMBH) system, if one star reaches a high velocity increasing significantly its energy, the companion would reduce its orbital energy and, eventually, could be trapped in a orbit around the SMBH, becoming an S-star.

In our simulations, the stars in the binary systems are assumed equal mass, $m_* = 3M_\odot$, as the first observed HVS (Brown, 2015), revolving around each other on initially circular orbits at various separations, a_*, in the range $0.1 - 0.5$ AU. This way we almost reproduce the set of HVSs studied by Ginsburg & Loeb (2006); Ginsburg et al. (2012), thing useful also for the sake of result comparison. Each star in the binary hosts one planet (see Figure. 4.1) with mass $m_p = 10^{-3}\ M_\odot$ (i.e. Jupiter-like), whose orbit would have been circular of radius $a_p = 0.02$ AU around the primary. The initial position of centre of mass of the 4-body system is located 2000 AU away from the SMBH. Note that this distance (0.01 pc) is well within the SMBH influence radius (~ 2.5 pc) but still $\sim 25,000$ the SMBH Schwarzschild's radius.

This means that the role of an external potential would be relevant just secularly and that, for highly eccentric binary orbits, deviation from Newtonian gravity may be important, so to make necessary to consider, at least, a Post-Newtonian treatment of the violent interaction with Sgr A* object. Hence the simulations are done considering post-Newtonian approximation up to order 2.5 which is the cause of the orbital precession.

Most importantly, we have to place binary stars onto orbits that come close enough to the SMBH. If the tidal disruption radius of a binary is given by (Merritt, 2013)

$$r_t \approx a_* \left(\frac{M_\bullet}{m_*}\right)^{1/3}, \tag{4.4}$$

we have to choose an initial transverse speed ($v_\perp$)

$$v_\perp d = \left(\frac{GM_\bullet}{r_{min}}\right)^{1/2} r_{min}, \tag{4.5}$$

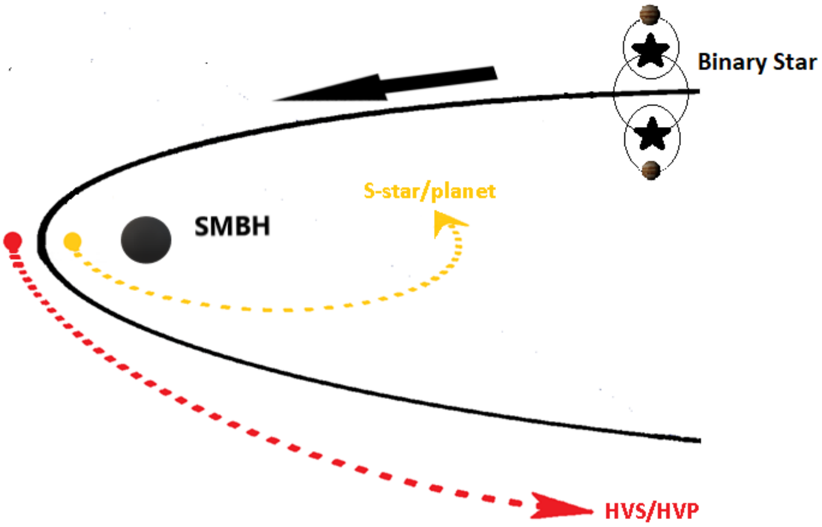

Figure 4.1: Hypothetical sketch of our four-body system approaching the SMBH. One Jupiter-mass planet is assigned to each star in the binary (Figure inspired by Fig.2 Brown (2015)).

for the binary so that $r_{min} \lesssim r_t$, where r_{min} is the minimum distance of the binary's orbit in the initial approach of the binary towards the SMBH and d is the initial position of the system's centre of mass from the SMBH (Ginsburg & Loeb, 2006). Therefore, we give to the system centre of mass a transverse (respect to the binary centre of mass-SMBH joining line) initial speed of $v_\perp = 66.5$ km s^{-1}, which is the maximum speed for systems to enter the binary-SMBH tidal radius.
We run simulations at varying: (i) the inclination angle, i, of the binary orbital plane respect to its centre of mass orbital plane, choosing the values 0°, 90° and 180° (an inclination 0° means that the four-body system is counter rotating respect to the centre of mass orbital plane and inclination 180° is on the opposite), and, (ii), the initial orbital "phase" angle (ϕ) of the binary orbit in the whole $0° - 360°$ range at steps of 15°. The phase angle is defined as the initial value of the angle between the 2 stars (and planets) in the assumption that the two planets start moving from positions on the same line joining the two stars, externally to them (see Fig. 4.2). In total, we have performed 360 simulations which all are extended up to 1600 years. Such a time corresponds to ~ 200 approaches to pericentre by the binary star and to ~ 975 times the initial planet orbital period.

Table 4.1 gives the set of values of the initial parameters. Every run is characterized by the $(a_\star, i, \phi)$ set of values, because $a_P, m_\star$ and m_P are fixed.

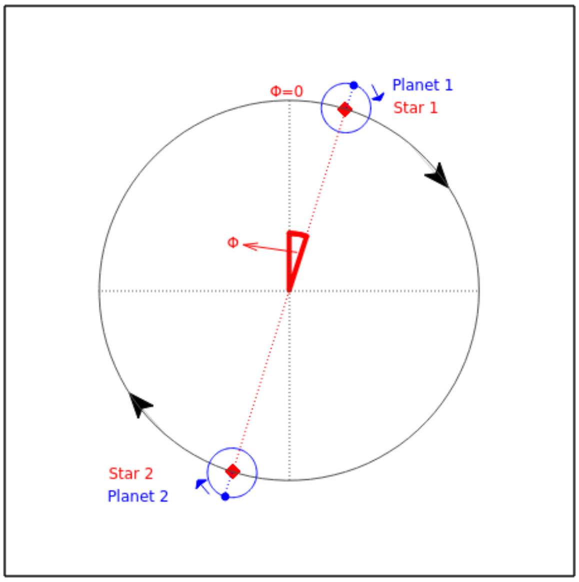

Figure 4.2: The phase angle (ϕ) between the position vectors of the two stars (or star-planet).

Table 4.1: Initial values for run parameters.Angle ϕ varies at 15° steps.

$a_\star$ (AU)	a_P (AU)	$m_\star$ $M_\odot$	m_P $M_\odot$	i deg	ϕ deg
0.1	0.02	3	0.001	0, 90, 180	0–360
0.2	0.02	3	0.001	0, 90, 180	0–360
0.3	0.02	3	0.001	0, 90, 180	0–360
0.4	0.02	3	0.001	0, 90, 180	0–360
0.5	0.02	3	0.001	0, 90, 180	0–360

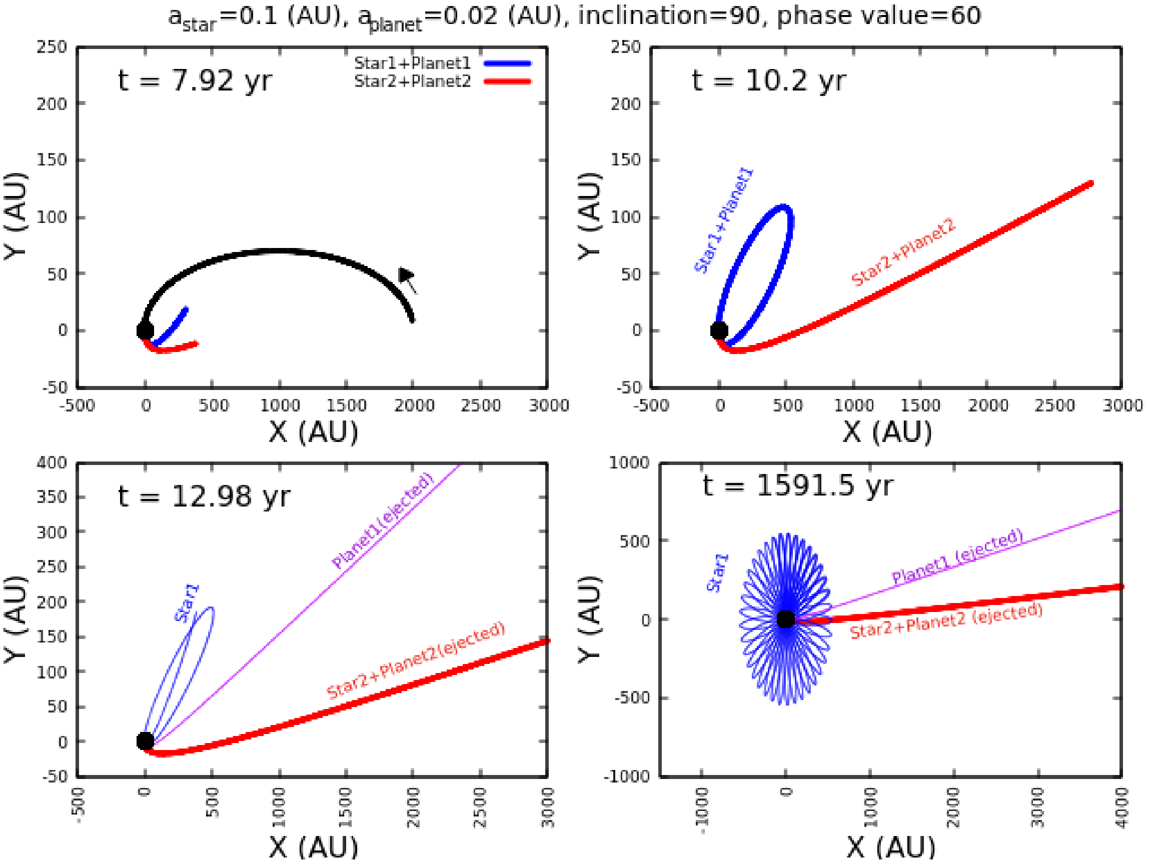

Figure 4.3: Snapshots of the trajectories of the system components for $(0.1, 90°, 60°)$ along their travel around Sgr A* taken at different times.

4.2 Results

Our simulations show that after the interaction of the binary system with the SMBH, there are various possible fates for the four–body system components:

- one of the stars becomes a high- or even hyper-velocity star, keeping, or losing its planet;
- if one star is expelled as high velocity, the other can be captured around the SMBH, starting to revolve on a precessing, eccentric, orbit (S-star) with or without its planet;
- planets can be expelled alone or bound to their host star and follow either unlimited orbits in the Galaxy (hypervelocity planets, HVPs) or revolving independently on highly eccentric orbits around Sgr A* (S-planets), similarly to the S-stars;
- stars and/or planets plunge into the SMBH and get swallowed by it.

In Figures 4.3 and 4.4 two examples of our runs are displayed, with initial values $(0.1, 90°, 60°)$ and $(0.4, 180°, 150°)$, respectively.

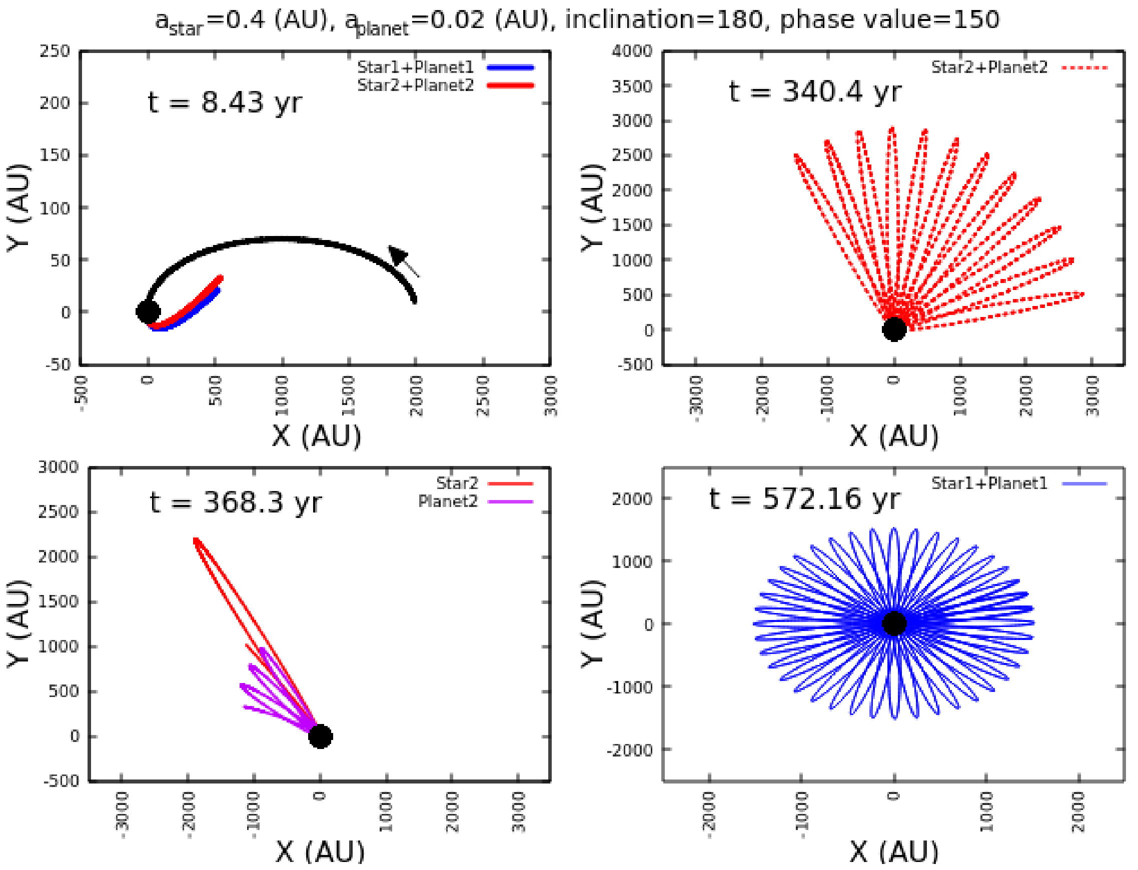

Figure 4.4: Close approach of the system $(0.4, 180°, 150°)$ to Sgr A*: precessing single S-star (solid red line), single S-planet (magenta line) and S-star with planet (blue line). Time flows from left-top to bottom-right.

These figures show two different outcomes after the encounter of the binary system owning planets with the SMBH in the GC. In Figure 4.3 the initial binary separation is $a_\star = 0.1$ AU and the binary orbital plane is perpendicular to its centre of the mass orbital plane, and the initial phase value of the binary orbit is $\phi = 60°$. After the first approach of the binary with the SMBH, one star is ejected together with its planet (red line); the companion star keeps moving around the SMBH for one more revolution (precessing blue line) before its planet is expelled as an HVP (magenta line) while the star remains bound to the SMBH as S-star (blue line). In Figure 4.4 the initial binary separation is larger (0.4 AU) and the orbital plane inclination angle is $i = 180°$; the angular phase of the binary is $\phi = 150°$. After 12 passages around the SMBH (dashed red line), one of the star-planet systems is broken, with both the components becoming S-star and S-planet on individual different paths around the SMBH (solid red line and magenta line, respectively). The other star keeps its planet while it revolves the SMBH as S-star (precessing blue line).

Figure. 4.5 illustrates the results of our simulations in the form of fractional pie. Overall our set of simulations, the fraction of systems result in producing S-stars is the highest, $\sim 40.2\%$, whereas the minimum belongs to the S-stars with orbiting planets ($\sim 1.3\%$). Note that the chance for planets to be thrown out the GC as HVPs or survive around Sgr A* as S-planets is high: ~ 27.1 % and $\sim$ 19.1 %, respectively. Moreover, our simulations could give rise to a small number of planets about HVSs ($\sim 1.6\%$), although 25% of these planets can survive about their host HVS until the end of the simulation. On the contrary, planets around S-stars are more fortunate: $\sim 63\%$ survive while the rest are tidally captured by the host star (see Figure 4.5).

We have to denote that the tidal capture of a planet by the host star occurs when the planet approaches the star closer than the tidal radius which for our Jupiter-like planets in the field of a 3 $M_\odot$ star is ~ 0.007 AU.

Figure 4.6 illustrates, as an example, the star-planet distance versus time for the "HVS with planet" (top panel) and the "S-star with planet" (bottom panel). The plots show how in the first case (top panel) the planet pericentre approaches closely the tidal radius while in the other case the planet always travels safely far from the hosting star.

In addition, Figure. 4.7 displays the fraction of tidally capture planets around S-stars. As expected, due to Kozai–Lidov mechanism, as the time advancing the tidal capture rate of planets increases.

Note also that the "early" mergers onto the SMBH (i.e. $\lesssim 3$ passages around the SMBH) involve only planets and not their parent stars. Moreover, the planet mergers constitute 2.5% of all mergers onto the SMBH and the other 0.2% are star-SMBH mergers.

Furthermore, the likelihood of various outcomes depends strongly on the initial complexity of the system. Results significantly modify based on two crucial elements:

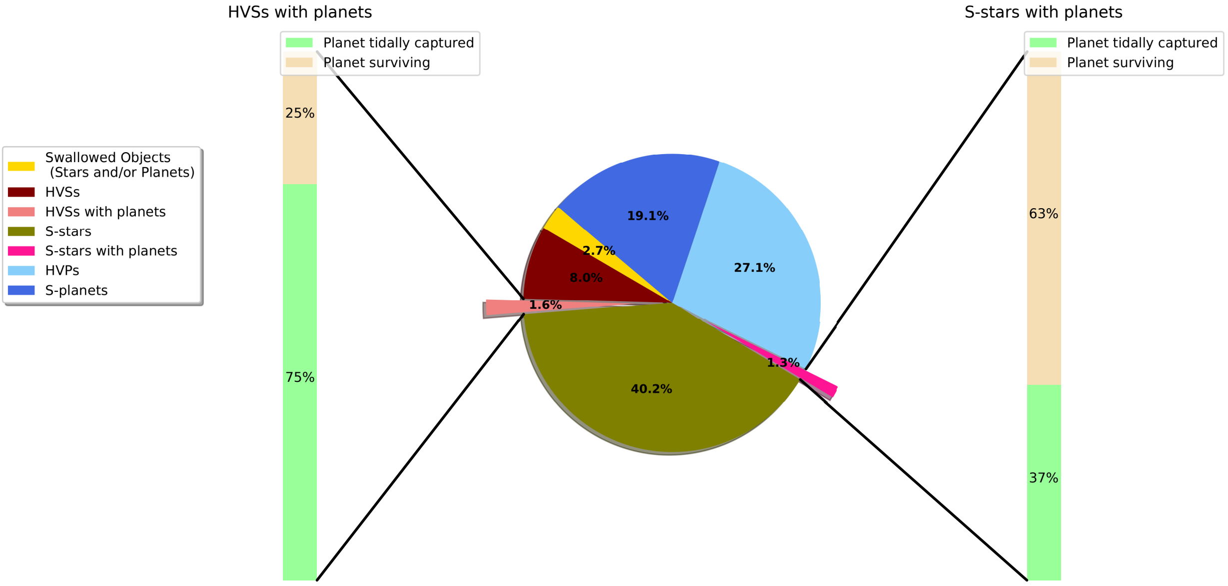

Figure 4.5: The various outcomes of our simulations in their percentage to the total. The two separate bar charts illustrate capture and survivability fraction of planets around HVSs (left bar) and S-stars (right bar). $\sim 75\%$ of planets in the "HVSs with planets" set are tidally destroyed by the companion HVS and this happens always at the first approach of the original system to the SMBH.

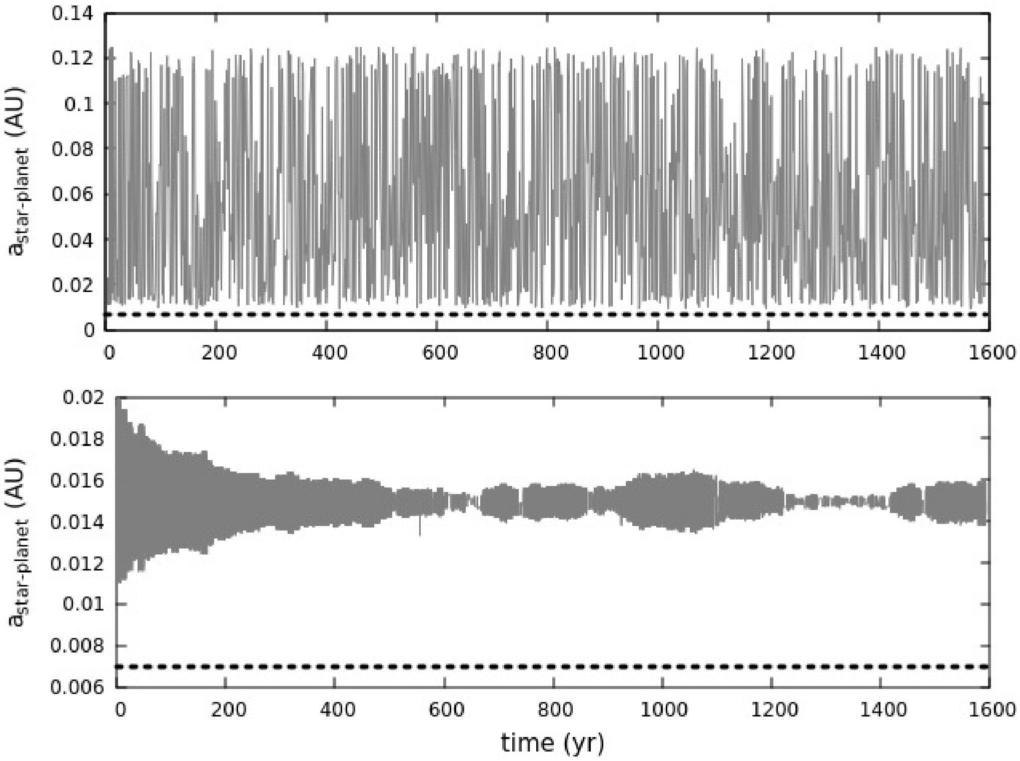

Figure 4.6: Evolution of the star to planet distance versus time for the "HVS with planet" set (top panel) and the "S-star with planet" revolving the SMBH (bottom panel). The dashed horizontal line in the both panels indicates the tidal capture radius of the star (~ 0.007 AU).

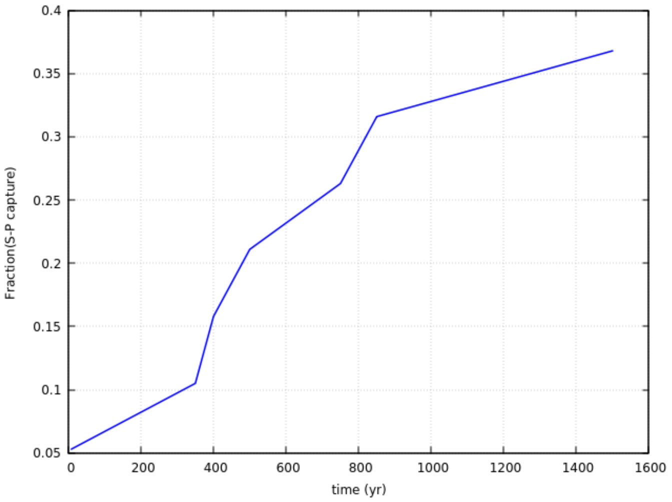

Figure 4.7: Fraction of tidally captured planets in "S-stars with planets" systems versus time.

Table 4.2: The fraction of various outcomes for different inclinations (first column). The second and third columns report the fraction of HVSs and HVPs produced. In the fourth column the term HVS-P means the fraction of HVSs with planets, while the term $S-P$ (fifth column) refers to the fraction of S-stars with planets. The fraction of S-stars and S-planets in our simulations are shown in the sixth and seventh columns, respectively. The eighth column indicates the fraction of stars and/or planets *swallowed* by the SMBH.

inc	HVS	HVP	HVS-P	S-P	S-star	S-planet	swallowed
0°	0.056± 0.03	0.265± 0.11	0.004± 0.00	0.054± 0.02	0.408± 0.18	0.185± 0.08	0.027± 0.01
90°	0.094± 0.04	0.269±0.12	0.092±0.06	0.000±0.00	0.360±0.16	0.160±0.07	0.025±0.01
180°	0.046±0.02	0.254±0.11	0.004±0.00	0.025±0.01	0.435±0.19	0.206±0.09	0.029±0.01

1. **Orbital plane inclination variation:** Our simulations also show that changing the orbital plane of the binary system with respect to their centre of mass orbital plane is effective on the final fate of the star-planet systems. Actually, we found that for both co-rotating ($i = 0°$) and counter-rotating ($i = 180°$) coplanar motions the chance to get HVSs with planets is less than half the case of $i = 90°$. On the contrary, the result of S-stars with planets has almost zero probability for 90° inclined binary planes. Table 4.2 summarizes the probabilities of different outcomes for the three inclinations examined.

2. **Initial star separation variety:** Table 4.3 illustrates our results for different initial semi-major axes. It shows a strong relation between the initial separation of the stars in the binary and the fate of the system after interaction with the SMBH. For tighter binaries, $a_* = 0.1$ and $a_* = 0.2$ AU, there is a little probability of having HVSs with planets, which drops to zero for wider initial star separations, that is $a_* = 0.3$, $a_* = 0.4$ and $a_* = 0.5$ AU.

Due to Hills (1988) prediction, an HVS could reach a speed of $\sim 4000\ kms^{-1}$. In general, of our 360 simulations, 118 HVSs were produced among which there are some HVSs even faster than Hills' expectation ($> 4000\ km\ s^{-1}$), while HVPs could even speed up to $> 9000 km\ s^{-1}$. Figure 4.8 demonstrate the escape velocity of HVS/Ps with respect to their distance from the SMBH. The mean distance where HVS/Ps reach, until the end of the simulation, is $\sim 0.5 pc$. A corresponding escape velocity of $v_{esc} \sim 300 km\ s^{-1}$ at this distance is considered.

Table 4.3: The fraction of various outcomes at varying binary star initial semi-major axis (first column). The meaning of other columns is the same as in Table 4.2.

a_*(AU)	HVS	HVP	HVS-P	S-P	S-star	S-planet	swallowed
0.1	0.142±0.08	0.260±0.15	0.097±0.08	0.000±0.00	0.302±0.17	0.139±0.08	0.059±0.03
0.2	0.059±0.03	0.229±0.13	0.069±0.06	0.035±0.02	0.389±0.22	0.194±0.11	0.024±0.01
0.3	0.063±0.03	0.257±0.14	0.000±0.00	0.028±0.02	0.424±0.24	0.212±0.12	0.017±0.01
0.4	0.035±0.02	0.254±0.14	0.000±0.00	0.056±0.04	0.427±0.24	0.208±0.11	0.021±0.01
0.5	0.028±0.02	0.313±0.17	0.000±0.00	0.014±0.01	0.465±0.26	0.163±0.09	0.017±0.01

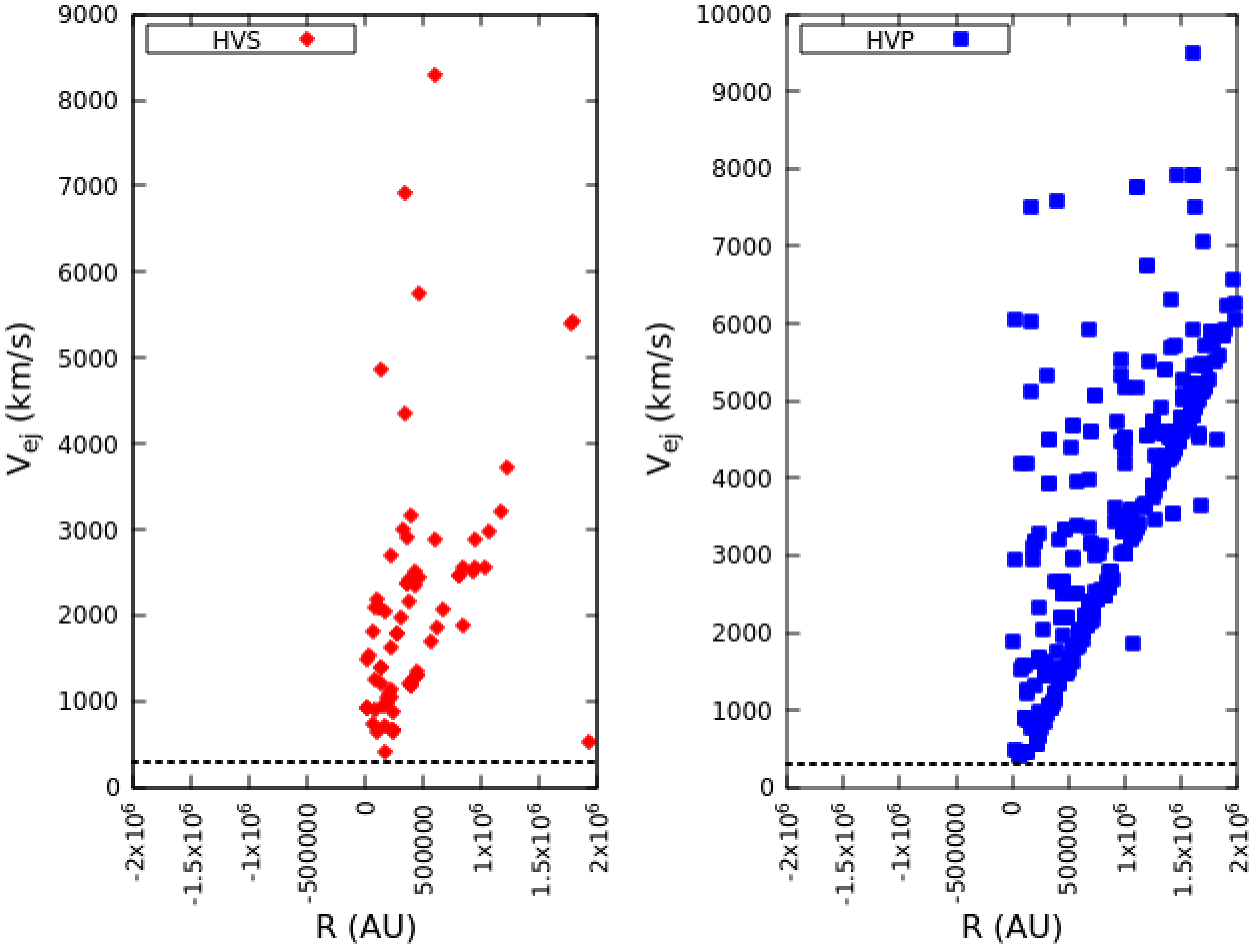

Figure 4.8: Ejection velocity v_{ej} as a function of distance (R) to the SMBH for HVSs (left) and HVPs (right). Black dashed line illustrated $v_{esc} = 300km\ s^{-1}$.

4.3 Conclusions

We investigated the dynamics of binary stars hosting one planet each as they move toward the supermassive object in the centre of our Galaxy. Due to the continuous discovery of exoplanets, the likelihood that every star borrows a certain number of planets around seems quite reasonable. Obviously, the number of output channels after the scattering of the system around the SMBH increases with the complexity of the system. This leads to the intriguing possibility of the existence of HVSs borrowing planets around and/or individual HVPs, as well as planets orbiting, similarly to S-stars, around the massive object (S-planets).

To perform our investigation, we exploited the accuracy and reliability of the regularized N-body code `ARGdf`, which is a modified version of the Mikkola's `AR-CHAIN` code (which includes post-Newtonian corrections up to order 2.5) to account for an external potential and its dynamical friction.

Our simulations deepen and enlarge previous works on similar topics by Ginsburg & Loeb (2006); Ginsburg et al. (2012) and Fragione & Ginsburg (2017). We estimated the ejection and capture probabilities of the four-body system in its interaction with Sgr A* in the general field of the Milky Way. We saw that stars and planets may escape the GC as HVSs or HVPs, respectively, or be captured on tightly bound orbits around the SMBH. In order to have, after the interaction with the SMBH, an HVS with a planet, the initial star binary separation, a_*, should have been sufficiently small, in the range $0.1 \leq a_* \leq 0.2$ AU.

Overall our simulations, about $\sim 1.6\%$ of ejected stars retain their planets which three–quarters of those planets are tidally captured by the host HVS in the later times. On the other hand, wider binary separations, $0.2 \leq a_* \leq 0.5$ AU, produce S-stars with planets which means that in this range of a_* the probability of HVSs with planets is zero (see Table. 4.3).

The most likely outcome of our simulations are S-stars: ~ 40.2 % and $\sim 1.3\%$ of the total outcomes are S-stars with planets, as shown in Figure. 4.5. Furthermore, $\sim 2.7\%$ of objects are swallowed by the SMBH, 90% of which are planets while only 10% are stars. Most of the merger events of planets with the SMBH takes place in $\lesssim 3$ revolutions around Sgr A*.

Our simulations also show that both starless planets and S-stars with planets can exist around the SMBH on high eccentric ($e \sim 0.97 - 0.98$) orbits similar to the G2-cloud orbital eccentricity. Unfortunately, the eccentricity of S-stars and S-planets never diminish below this value, thus star/planets generated via Hills mechanism could never perfectly match with G1 orbital elements. Additionally, we could conclude that, over the time extension of our simulations, the stability of planets about S-stars is much higher than those about HVS.

Finally, we note that more than 500 candidates have been proposed for HVSs in the Open Fast Star Catalog[1] awaiting to raise significantly the chance of planet detection around HVSs.

---

[1] https://faststars.space

Chapter 5

Interaction of S-stars hosting planetary systems with Sgr A* black hole

The centre of our galaxy is occupied with a dynamically relaxed dense cluster of stars, the so-called "S-stars", orbiting in the central gravitational potential which is believed to be created by a supermassive black hole (SMBH) with a mass of $\sim 4.3 \times 10^6$ $M_\odot$ at the distance $\sim$ 8.3 kpc from us (Gillessen et al., 2017) (see section 1.2.4 of this thesis).

Recent spectroscopy analysis of the central arcsecond of the Galactic Center (GC) reveals the presence of a population of both early-type and late-type among the stars in the S-star cluster with the magnitude in the range $m_K = 14 - 17$ (Habibi et al., 2017, 2019). The age estimated for the star S2 is about 6.6 Myr and for the rest of the early-type stars is less than 15 Myr whereas for the late-type stars is $\sim$ 3 Gyr. The younger their ages the more mysterious seems their presence in their current location since strong tidal forces of the SMBH would inhibit star formation in that region (Morris, 1993). For this reason, the migration model, due to binary disruption, is more likely to explain their presence in the vicinity of Sgr A* (Hills, 1988). Therefore, it is usually assumed that the S-stars formed elsewhere and migrated to their current locations (Antonini, 2013). If so, primarily before getting engaged in the GC, they might have hosted planetary systems. In that case, it is plausible that they still preserve their planetary systems throughout their voyage.

The presence of planets or planetary systems in the vicinity of Sgr A* is still debated. (Trani et al., 2016) studied the tidal capture rate of single planets orbiting stars in the CW disc and in the S-star cluster. Trani et al. (2016) found that tidally captured planets which were initially bound to CW disc stars remain in the CW disc. On the contrary, Trani et al. (2016) simulations for S-star cluster illustrate that planets initially bound to S-stars are captured by the SMBH on highly eccentric orbits, matching the semi-major axis and eccentricity of the G1 and G2 clouds.

Many explorations have achieved so far concerning the dynamics and stability of planetary systems in star clusters (e.g., Spurzem et al. (2009); Cai et al. (2017); Li et al. (2019)). Spurzem et al. (2009) investigated the dearth of planets in the long-lived open and globular clusters. Taking advantage of two independent numerical approaches, a hybrid Monte Carlo and a direct N-body method, Spurzem et al. (2009) examined the role of stellar encounters for the paucity of planets in such mature stellar clusters. Slightly close stellar encounters, which are likely to happen in dense clusters, can provoke planets' orbital eccentricity and induce dynamical instability, especially in packed systems. The detached planets generally remain in their host clusters as free floaters. The discovery of freely floating low-mass objects in young stellar clusters such as σ Orionis could be a supporting piece of evidence for this scenario. however, Spurzem et al. (2009) denoted that short-period planets are more difficult to get disrupted by stellar encounters and such interactions can excite modest eccentricity among them, such that orbital decay, tidal inflation, and even disruption of the close-in planets are the subsequent tidal dissipation effects.

To understand better the role of stellar encounters in the destabilization of planetary systems, Cai et al. (2017) performed N-body integration for four different planetary system models in three different star cluster environments (N = 2k, 8k and 32k stars, respectively). Cai et al. (2017) assigned an ensemble of initially identical planetary systems solar-type stars and followed their evolution for 50 Myr. Due to external perturbations and planet-planet interactions, protoplanetary discs survivals are reduced significantly in more populous clusters. Moreover, due to Cai et al. (2017), planet-planet can grow the fragility of planetary systems induce to their ejection and double their absence in the cluster. Albeit, from an observational point of view, Cai et al. (2017) results anticipate higher planet detection rates in the young low-mass star clusters.

In conformity of the above frameworks, following the migration scenario, in this chapter, we intend to investigate the destiny of putative planetary systems around stars in the S-star cluster after close interaction with the central black hole of our galaxy and inspect their dynamics and stability in the super hostile environment of the GC.

5.1 Model and methods

So far, the number of known stellar orbits around Sgr A* has determined to around 40, which 8 stars of this group belong to the CW disc (Gillessen et al., 2017). The S-star cluster is indeed a dynamically relaxed cluster. The brightest star of this ensemble is the star S2 which is measured to be a B-type main sequence star (Ghez et al., 2003). In general, 32 out of 40 stars of this group are young stars of spectral type of B0-B3V (Gillessen et al., 2017) with the estimated mass of $8 - 14 M_{\odot}$ (Habibi et al., 2017) while the other 8 stars are old (G, K, and M type) with an initial-mass range of $0.5 - 2$ $\mathrm{M}_{\odot}$ (Habibi et al., 2019). Besides, out of the 32 B-type S-stars, 8 appear to be part of the CW disc, while the remaining 24 have randomly oriented orbits.

We run simulations for the 40 innermost stars for which their orbital parameters are known, using the data of Gillessen et al. (2009, 2017) as initial conditions. We carry out our simulations by means of `ARGdf`code (Arca-Sedda & Capuzzo-Dolcetta, 2019) which is a modified version of `AR-CHAIN` (Mikkola & Tanikawa, 1999a,c; Mikkola & Merritt, 2008b), a fully regularized N-body code with post-Newtonian corrections up to order 2.5, enabled to use analytical external potentials and their dynamical friction. Figure. 5.1 delineates comparison of our computed orbits of the S-stars (without planets) with the observed trajectory of S-stars in Gillessen et al. (2009).

The semi-major axis of the S-stars orbits lies in the range of $\sim$ 0.005-0.05 pc, and they approach very close to Sgr A* where the relativistic terms could be important. For this reason, we made our simulations taking into account the post-Newtonian corrections of equation of motion up to order 2.5. The mass of Sgr A* is set to $\sim$ 4.3 $\times 10^6$ $\mathrm{M}_\odot$ and a distance of 8.33 kpc to Sgr A* is assumed (Gillessen et al., 2009, 2017), i.e., 1" corresponds to 40.4 mpc (milliparsec). Both population of young (B-type) or old (G, K, and M type) giant stars (post main-sequence) are observed in this region (Ghez et al., 2003). The stars in Habibi et al. (2017) belong to the early-type group and in Habibi et al. (2019) belong to the late-type group. Habibi et al. (2017) derived specifically the masses of 8 stars in early-type group. We use their evaluation to estimate the mass of other early-type stars which have a similar magnitude (m_k) to the stars which are studied in Habibi et al. (2017) and for the rest of early-type S-stars (fainter ones) we assume the mass range of $8-14M_\odot$. Furthermore, Habibi et al. (2019) measured an initial-mass range of $0.5-2$ $\mathrm{M}_\odot$ for the older stars ($\sim$ few Gyr old). We also implement the mass range of $0.5-2$ $\mathrm{M}_\odot$ for late-type stars in our simulations.

We assign planetary systems to each of the stars in S-star cluster similar to our Solar planetary system in mass, eccentricity and semi-major axis. For late-type stars, every planetary system is composed of 7 planets; Mercury, Venus, Earth, Mars, Jupiter, Saturn and Uranus. For the early-type stars, every planetary system consists of 3 giant planets (Jupiter, Saturn and Uranus). Since it is less likely that massive early-type stars harbor planets so close, for these stars we exclude the first 4 planets.

We change the inclination of the planetary system orbits respect to the parent star orbital plane in the range $0^\circ-180^\circ$ with increments of 10°. Since the star S85 has the longest orbital period of $\sim$ 3580 yr, we stop the simulations at the time 4000 yr to follow at least one of its periods. Each run consists of total 193 bodies (192+SMBH) with the mass ratio of $\sim 10^{13}$, so the average computation time for each single run is $\sim$ 48-72 hours and the total number of simulations is 76. Table 5.1 shows the assumed parameters of our runs.

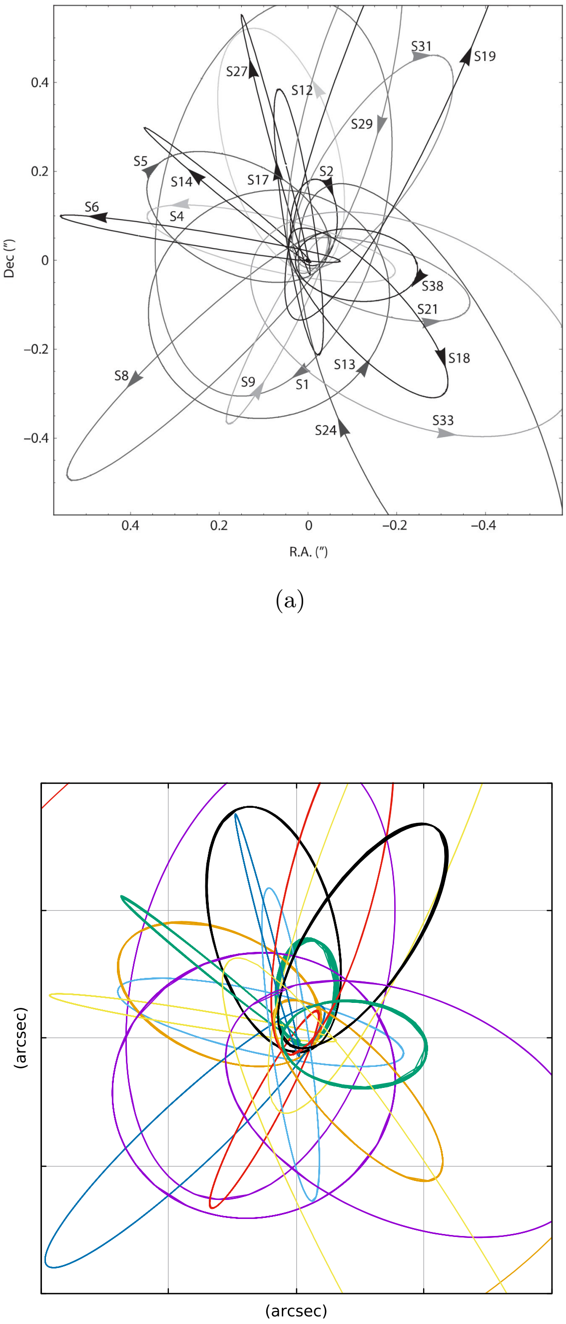

(a)

(b)

Figure 5.1: Comparison of trajectories of the S-stars projected onto the plane of the sky due to Gillessen et al. (2009) (a) with their orbits due to our simulation including PN terms up to order 2.5 (b). The scale of both figures is the same in arcsecond.

Table 5.1: Assumed parameters for our simulations.

Spectral Type	**Mass Range** ($M_{\odot}$)	**Number of Planets**	**inclination (degree)**
early-type	$8-14$	3	$0-180$
late-type	$0.5-2$	7	$0-180$

5.2 Results

We find that $\sim 51\%$ of planets survive on stable orbits around their host S-stars after the close interaction with the SMBH until the end of simulation. Moreover, $\sim 49\%$ starless planets which are captured by the SMBH and revolve on individual orbits around it. In most of the cases Saturn- and Uranus-like planets leave the planetary system after the first passage around the SMBH. Figure. 5.2 displays the fraction of stable star-planet systems after the encounter with the SMBH. The stability of of orbital elements for planets assigned to the star "S89" (a=0.044 pc) is delineated in Figure. 5.3. The Uranus-like planet is detached from the star after the first pericentre passage. Although the eccentricity and inclination enhancement of the inner planets (Mercury, Venus, Earth and Mars) is more significant compare to the outer ones, however their stability lasts for ~ 10 pericentre passages corresponding to 4000 yr.

There is a small probability (~ 0.0011) for planets to gain enough speed due to the encounter with the SMBH and be triggered out of the cluster (see Figure. 5.4). In addition, there is also a very low likelihood ~ 0.0010) in early-type stars to swap their planetary systems once they get too close to each other before approaching the SMBH. Moreover, we estimate the absorption probability of planets by their host star is extremely low.

We check the variation of planet inclination respect to its host star inclination in the range $0^{\circ}-180^{\circ}$ and the survival probabilities for different planets versus inclination are presented in Figure. 5.5.

Comparing the orbital parameters of starless planets around the SMBH, we find the Jupiter-like planets consistent in semimajor axis and eccentricity with the G1 cloud, while no planet can match those of the G2 cloud. Furthermore, the semimajor axis and inclination of some Uranus-like planets can correspond to that of the G1 cloud (see Figure. 5.6).

5.3 Conclusions

We investigated the dynamics and stability of planetary systems orbiting the S-stars in the central arcsecond of the Galaxy by means of a regularized N-body code `ARGdf` taking into account post-Newtonian approximation up to order 2.5.

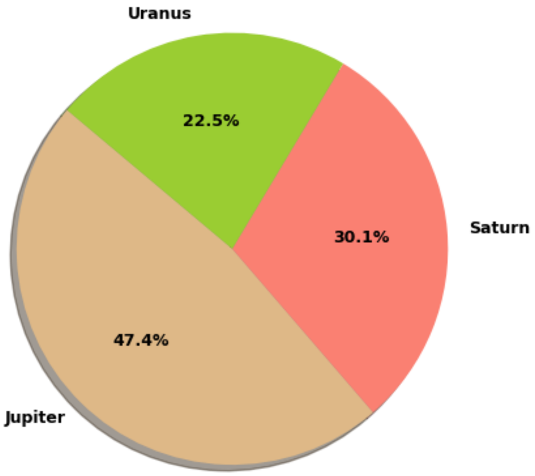

(a) early-type

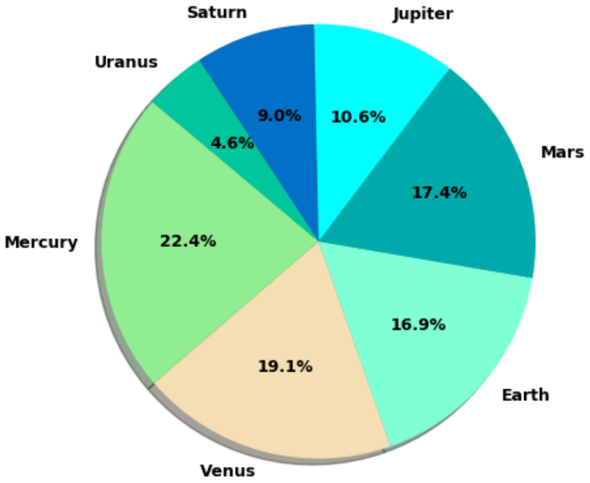

(b) late-type

Figure 5.2: Fraction of bound planets to the early-type stars (a) and to late-type stars (b).

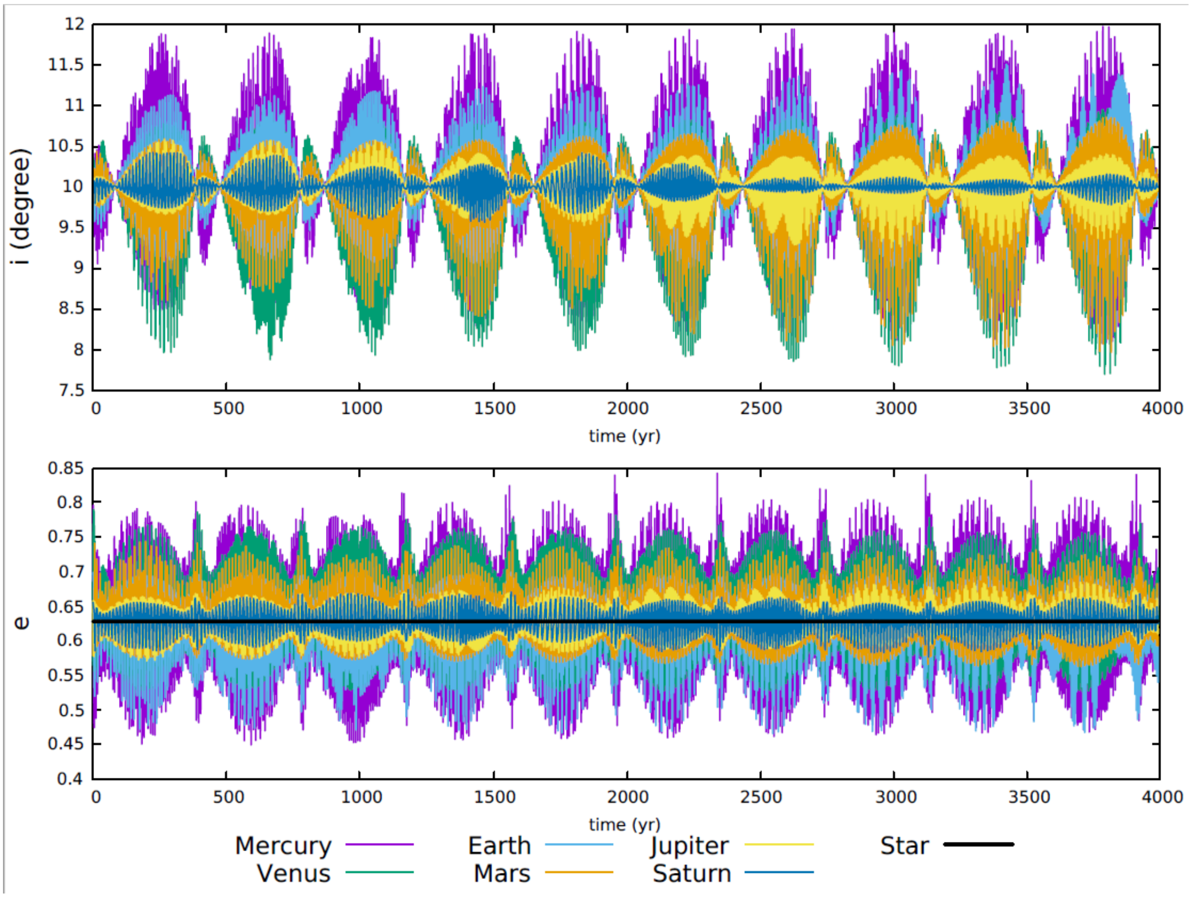

Figure 5.3: Semimajor axis and eccentricity versus time of six survived planets around the star ”S89”. The semimajor axis of the host star is $\sim$ 0.04 pc and the solid black line illustrate its eccentricity ($e = 0.639$). The eccentricity and inclination of inner planets (Mercury, Venus, Earth and Mars) fluctuate larger than the giant ones (Jupiter and Saturn).

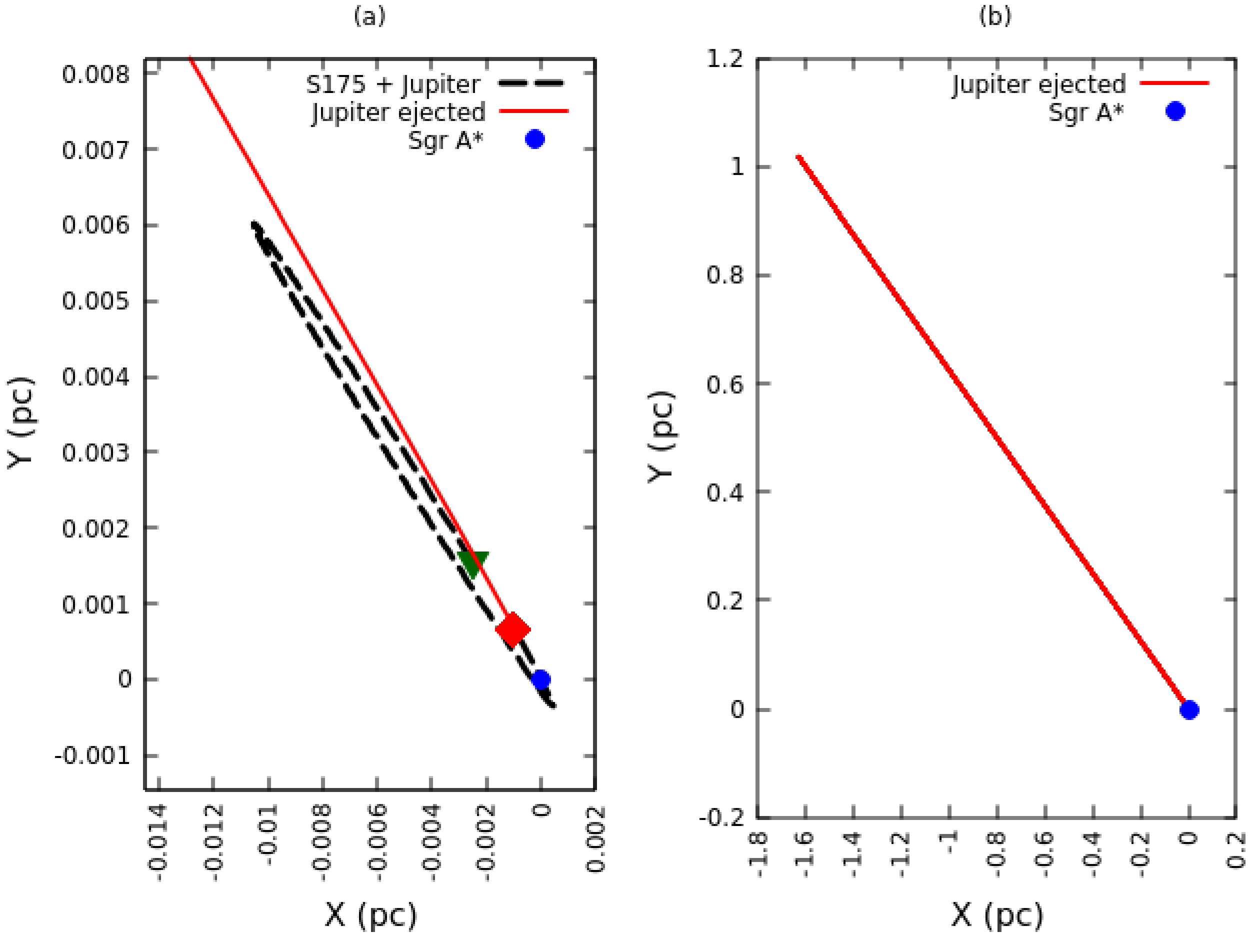

Figure 5.4: Illustration of Jupiter-like planet ejection primarily attached to the early-type star S175 ($a_\star = 0.016$ pc). The filled green triangle demonstrate the star-planetary system starting point and the filled red square is the star-planet detachment point (a). The right panel (b) shows the maximum distance where the expelled planet can reach until the termination of simulation.

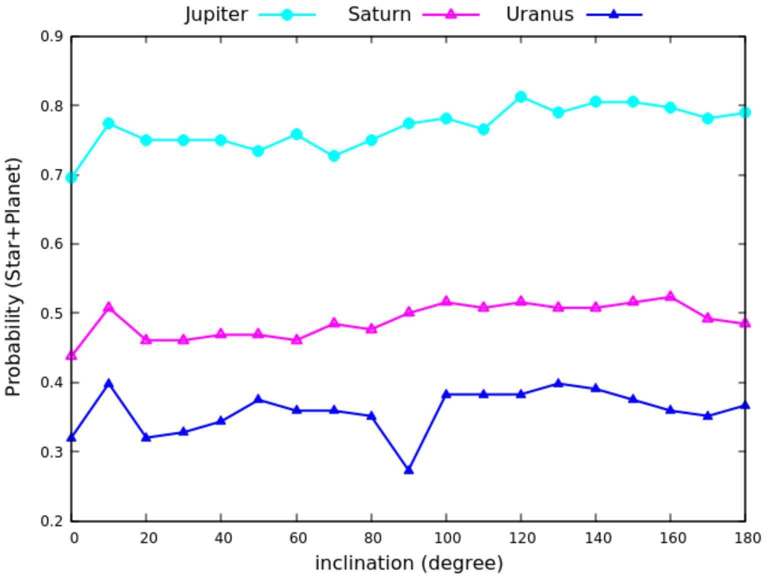

(a) early-type

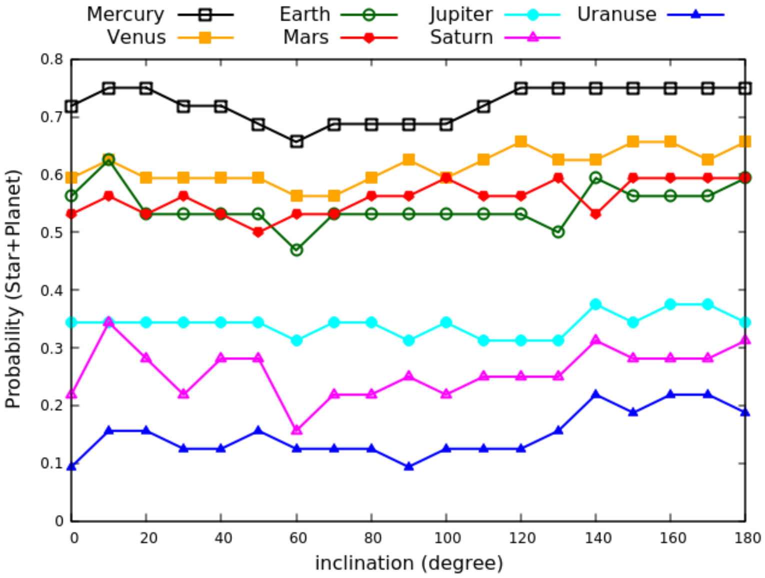

(b) late-type

Figure 5.5: Probability of bound planets to the early-type stars (a) and to late-type stars (b) versus inclination.

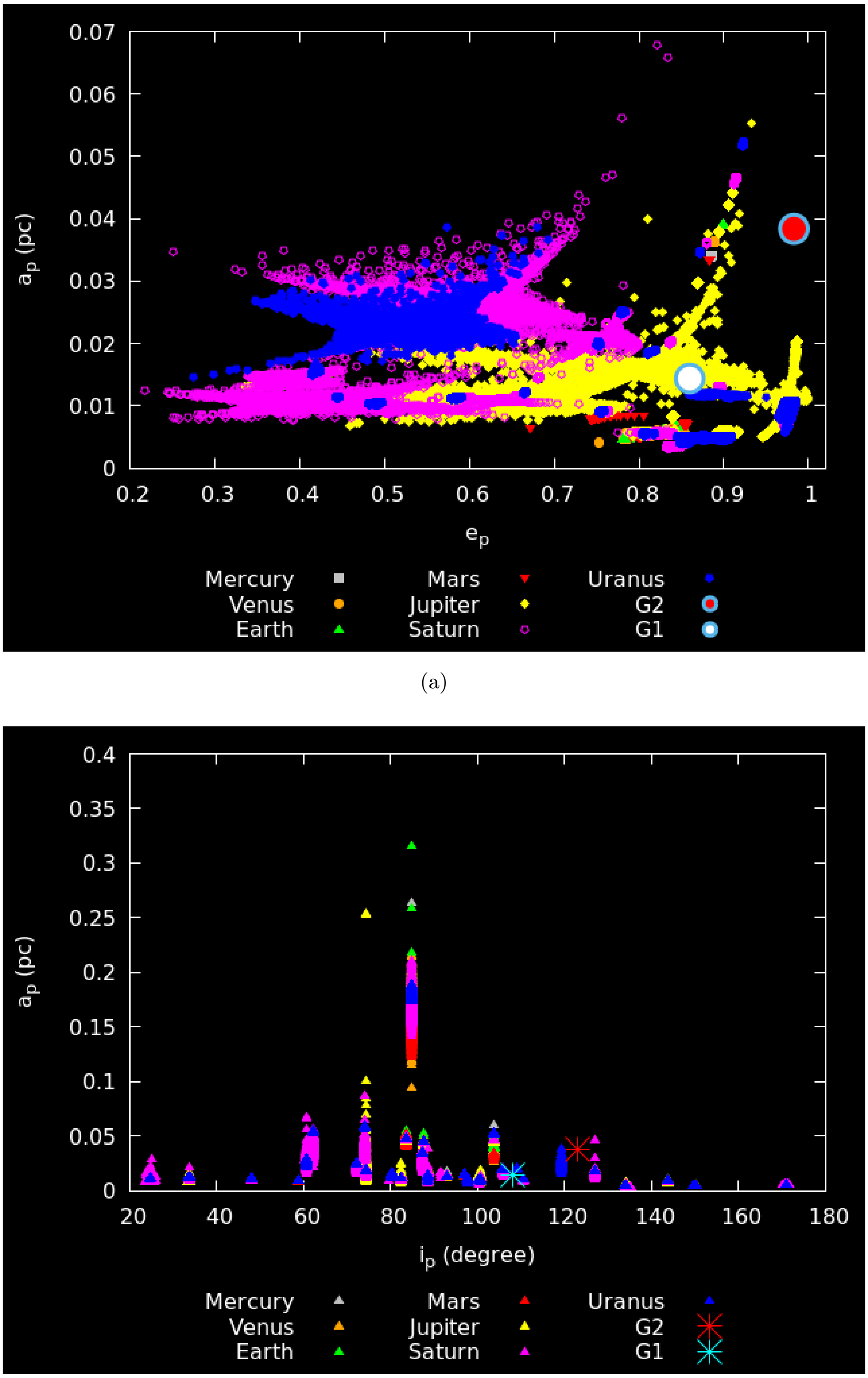

(a)

(b)

Figure 5.6: Semimajor axis (a_p) versus eccentricity (e_p) (a) and inclination (i_p) (b) of starless planets around Sgr A*. Some Jupiter-like planets are in good agreement in $a_p - e_p$ with G1 cloud (white circle) and some Uranus-like ones are consistent in $a_p - i_p$ with G1 cloud (cyan star).

We simulated 76 systems consisting of 40 S-stars and planetary systems similar to our Solar planetary system in mass, eccentricity and semi-major axis. Planetary systems assigned to late-type stars are composed of seven planets; Mercury, Venus, Earth, Mars, Jupiter, Saturn and Uranus. Planetary systems around early-type stars are made up of three giants; Jupiter, Saturn and Uranus.

We quantify the fraction of lost planets and stable star-planet systems and find that almost half of the planets ($\sim 51\%$) survive around the host and the other half are indeed captured by the SMBH ($\sim 49\%$). The innermost planets, Mercury for late-type stars and Jupiter for early-type ones, have the maximum fraction of survivability. The likelihood of ejected planets and swapped ones are estimated to be very low, ~ 0.0011 and ~ 0.0010, respectively.

We also investigated the orbital properties of starless planets around the SMBH and found consistency with the G1 cloud in semimajor axis and eccentricity for some Jupiter-like planets and in semimajor axis and inclination for some Uranus-like planets.

Chapter 6

Summary and overall conclusions

In this thesis we have investigated the existence and survivability of planets and planetary systems in their interaction with the massive object, in the Galactic Centre (GC). The main results of this study are summarized below.

By means of a high-precesion, regularized, post-Newtonian N-body code we studied the interplay of binary stars and their planetary systems with the Sgr A* black hole in the GC. We considered the contribution of an analytic external potential and the dynamical friction due to the regular distribution of stars. Our aim was to provide a reliable likelihood estimation of the fraction planets bound about high velocity stars and that of the S-stars in the GC. We found that stars and planets may get kicked out of the GC as HVSs or HVPs, respectively. They might be captured around the SMBH on high eccentric, randomely-oriented orbits with different semimajor axes similar to the observed S-stars. There is an intriguing probability of recognizing planets orbiting around HVSs as well as S-stars.

In order to have an HVS with a planet around, the initial binary separation should have been sufficiently small. This can induce the production of $\sim 1.6\%$ HVSs with planets entire simulations. In contrast, wider binary separations could bring on S-stars with orbiting planets ($\sim 1.3\%$). Our simulations show that the planets which survived around HVSs can approach closely to the tidal disruption radius of their host stars whereas those around S-stars always travel safely far from the hosting star. In addition, the most probable outcomes of our simulations are S-stars ($\sim 40\%$) also HVPs could have a large creation fraction ($\sim 27\%$). We denote that the high eccentricity ($e \sim 0.97$) of lonesome planets and preserved planets around S-stars in the GC are consistent with that of the G2 cloud observed in the GC ($e \sim 0.98$).

We underline that the discovery of a solitary, super fast and distant planet is extremely challenging at the present time. Gravitational microlensing could be a suitable technique for the detection of small exoplanets at significant distances from the Earth. Due to the continuous discovery of exoplanets, and developing the observation techniques for exploration of the GC, we hope that in the near future there would be the possibility to detect planets both in the halo and in the central part of the Galaxy to support the above scenario.

In chapter 5 of this thesis, we probe the survivability likelihood of planetary systems in the proximity of Sgr A*. Supposing the existence of planetary systems around S-stars in the central miliparsec of the Galaxy. we ran simulations to investigate the dynamics and interaction of these planets with the SMBH.

To do this, we took advantage of the high-precision `ARGdf` code including the post-Newtonian approach up to order 2.5. We simulated the innermost 40 stars of the central arcsecond of our Galaxy for which their orbital parameters are known. We assigned planetary systems similar to our Solar planetary system to each star in the S-star cluster. A seven planet–system and a three planet–system are assumed around late- and early-type host stars, respectively.

We estimated the unbound and stable star-planet systems fractions, finding that almost half of the planets ($\sim 51\%$) survive around the host and the other half are indeed captured by the SMBH ($\sim 49\%$). The innermost planets, Mercury for late- and Jupiter for early-type host stars, have the biggest fraction of survivability. For the late-type stars, the Jupiter-like planet plays an important role for keeping the inner planets stable around their host stars so that in most of the cases the inner five planets survive. There is also a low likelihood of ejection and swapping of planets, ~ 0.0011 and ~ 0.0010, respectively. The orbital properties of starless planets around the SMBH are found in good agreement with the G1 cloud in semimajor axis and eccentricity for some Jupiter-like planets and in semimajor axis and inclination for some Uranus-like planets.

The existence of planets or planetary systems in the vicinity of Sgr A* is still debated. We hope by a future enlargement of our simulations, to be able to constrain for future observations.

Bibliography

Aarseth S. J., 2003, Gravitational N-Body Simulations

Aarseth S. J., Zare K., 1974, Celestial Mechanics, 10, 185

Abadi M. G., Navarro J. F., Steinmetz M., 2009, ApJL, 691, L63

Alexander T., 2017, Annual Review of Astronomy and Astrophysics, 55, 17

Alexander R. D., Armitage P. J., Cuadra J., 2008a, Monthly Notices of the Royal Astronomical Society, 389, 1655

Alexander R. D., Armitage P. J., Cuadra J., Begelman M. C., 2008b, The Astrophysical Journal, 674, 927

Allen D. A., Hyland A. R., Hillier D. J., 1990, MNRAS, 244, 706

Amaro-Seoane P., 2018, Living Reviews in Relativity, 21, 4

Amaro-Seoane P., Chen X., 2014, ApJL, 781, L18

Antonini F., 2013, ApJ, 763, 62

Antonini F., Faber J., Gualandris A., Merritt D., 2010, ApJ, 713, 90

Antonini F., Lombardi James C. J., Merritt D., 2011, ApJ, 731, 128

Antonini F., Capuzzo-Dolcetta R., Mastrobuono-Battisti A., Merritt D., 2012, ApJ, 750, 111

Arca-Sedda M., Capuzzo-Dolcetta R., 2014a, MNRAS, 444, 3738

Arca-Sedda M., Capuzzo-Dolcetta R., 2014b, ApJ, 785, 51

Arca-Sedda M., Capuzzo-Dolcetta R., 2017, MNRAS, 471, 478

Arca-Sedda M., Capuzzo-Dolcetta R., 2019, MNRAS, 483, 152

Arca-Sedda M., Capuzzo-Dolcetta R., Spera M., 2016, MNRAS, 456, 2457

Arca Sedda M., Berczik P., Capuzzo-Dolcetta R., Fragione G., Sobolenko M., Spurzem R., 2019, MNRAS, 484, 520

Bahcall J. N., Wolf R. A., 1976, ApJ, 209, 214

Balick B., Brown R. L., 1974, ApJ, 194, 265

Bartko H., et al., 2009, ApJ, 697, 1741

Bartko H., et al., 2010, ApJ, 708, 834

Baruteau C., Cuadra J., Lin D. N. C., 2011, ApJ, 726, 28

Baumgardt H., Gualandris A., Portegies Zwart S., 2006, MNRAS, 372, 174

Baumgardt H., Amaro-Seoane P., Schödel R., 2018, A&A, 609, A28

Becklin E. E., Neugebauer G., 1968, ApJ, 151, 145

Becklin E. E., Gatley I., Werner M. W., 1982, ApJ, 258, 135

Begelman M. C., Blandford R. D., Rees M. J., 1980, Nature, 287, 307

Binney J., Tremaine S., 1987, Galactic dynamics

Blaauw A., 1961, Bull. Astron. Inst. Netherlands, 15, 265

Blanchet L., 2014, Living Reviews in Relativity, 17, 2

Blanchet L., Iyer B. R., 2003, Classical and Quantum Gravity, 20, 755–776

Blum R. D., Ramírez S. V., Sellgren K., Olsen K., 2003, ApJ, 597, 323

Böker T., 2002, in Geisler D. P., Grebel E. K., Minniti D., eds, IAU Symposium Vol. 207, Extragalactic Star Clusters. p. 706

Böker T., et al., 2004, in Lamers H. J. G. L. M., Smith L. J., Nota A., eds, Astronomical Society of the Pacific Conference Series Vol. 322, The Formation and Evolution of Massive Young Star Clusters. p. 39 (`arXiv:astro-ph/0403067`)

Bonanos A. Z., López-Morales M., Hunter I., Ryans R. S. I., 2008, ApJL, 675, L77

Bonnell I. A., Rice W. K. M., 2008, Science, 321, 1060

Boubert D., Guillochon J., Hawkins K., Ginsburg I., Evans N. W., Strader J., 2018, MNRAS, 479, 2789

Bromley B. C., Kenyon S. J., Geller M. J., Barcikowski E., Brown W. R., Kurtz M. J., 2006, ApJ, 653, 1194

Bromley B. C., Kenyon S. J., Geller M. J., Brown W. R., 2012, ApJL, 749, L42

Brown W. R., 2015, ARA&A, 53, 15

Brown W. R., Geller M. J., Kenyon S. J., Kurtz M. J., 2005, ApJL, 622, L33

Brown W. R., Geller M. J., Kenyon S. J., 2014, ApJ, 787, 89

Brown W. R., Lattanzi M. G., Kenyon S. J., Geller M. J., 2018, ApJ, 866, 39

Buchholz R. M., Schödel R., Eckart A., 2009, A&A, 499, 483

Bulirsch R., Stoer J., 1966, Numerische Mathematik, 8, 1

Burkert A., Schartmann M., Alig C., Gillessen S., Genzel R., Fritz T. K., Eisenhauer F., 2012, ApJ, 750, 58

Cai M. X., Kouwenhoven M. B. N., Portegies Zwart S. F., Spurzem R., 2017, Monthly Notices of the Royal Astronomical Society, 470, 4337–4353

Capuzzo-Dolcetta R., 1993, ApJ, 415, 616

Capuzzo-Dolcetta R., 2016, Mem. Soc. Astron. Italiana, 87, 634

Capuzzo-Dolcetta R., Fragione G., 2015, MNRAS, 454, 2677

Capuzzo-Dolcetta R., Miocchi P., 2008a, MNRAS, 388, L69

Capuzzo-Dolcetta R., Miocchi P., 2008b, ApJ, 681, 1136

Capuzzo-Dolcetta R., Tosta e Melo I., 2017, MNRAS, 472, 4013

Carollo C. M., Stiavelli M., Mack J., 1998, AJ, 116, 68

Carr J. S., Sellgren K., Balachandran S. C., 2000, ApJ, 530, 307

Chandrasekhar S., 1943, ApJ, 97, 255

Chatterjee S., et al., 2005, ApJL, 630, L61

Christopher M. H., Scoville N. Z., Stolovy S. R., Yun M. S., 2005, ApJ, 622, 346

Clénet Y., Rouan D., Gratadour D., Marco O., Léna P., Ageorges N., Gendron E., 2005, A&A, 439, L9

Côté P., et al., 2006, ApJS, 165, 57

Cuadra J., Nayakshin S., Martins F., 2008, MNRAS, 383, 458

Davies M. B., King A., 2005, ApJL, 624, L25

De Colle F., Raga A. C., Contreras-Torres F. F., Toledo-Roy J. C., 2014, ApJL, 789, L33

Dehnen W., 1993, MNRAS, 265, 250

Do T., Ghez A. M., Morris M. R., Lu J. R., Matthews K., Yelda S., Larkin J., 2009, ApJ, 703, 1323

Do T., Lu J. R., Ghez A. M., Morris M. R., Yelda S., Martinez G. D., Wright S. A., Matthews K., 2013, ApJ, 764, 154

Dormand J. R., Prince P. J., 1978, Celestial Mechanics, 18, 223

Dray L. M., King A. R., Davies M. B., 2006, MNRAS, 372, 31

Du C., Li H., Newberg H. J., Chen Y., Shi J., Wu Z., Ma J., 2018, ApJL, 869, L31

Eckart A., Genzel R., 1996, Nature, 383, 415

Eckart A., Genzel R., Hofmann R., Sams B. J., Tacconi-Garman L. E., 1993, ApJL, 407, L77

Edelmann H., Napiwotzki R., Heber U., Christlieb N., Reimers D., 2005, ApJL, 634, L181

Eisenhauer F., et al., 2005, ApJ, 628, 246

Erkal D., Boubert D., Gualandris A., Evans N. W., Antonini F., 2019, MNRAS, 483, 2007

Erwin P., Gadotti D. A., 2012, Advances in Astronomy, 2012, 946368

Falcke H., Goss W. M., Matsuo H., Teuben P., Zhao J.-H., Zylka R., 1998, The Astrophysical Journal, 499, 731

Ferrarese L., Merritt D., 2000, ApJL, 539, L9

Ferrarese L., et al., 2006, ApJL, 644, L21

Fragione G., Capuzzo-Dolcetta R., 2016, Mem. Soc. Astron. Italiana, 87, 687

Fragione G., Ginsburg I., 2017, MNRAS, 466, 1805

Fragione G., Gualandris A., 2018, MNRAS, 475, 4986

Fragione G., Loeb A., 2017, New A, 55, 32

Fragione G., Capuzzo-Dolcetta R., Kroupa P., 2017, MNRAS, 467, 451

Fregeau J. M., Cheung P., Portegies Zwart S. F., Rasio F. A., 2004, MNRAS, 352, 1

Fritz T. K., et al., 2016, ApJ, 821, 44

Fujii M., Iwasawa M., Funato Y., Makino J., 2010, ApJL, 716, L80

Gaia Collaboration et al., 2018, A&A, 616, A1

Gallego-Cano E., Schödel R., Dong H., Nogueras-Lara F., Gallego-Calvente A. T., Amaro-Seoane P., Baumgardt H., 2018, A&A, 609, A26

Galley C. R., Leibovich A. K., Rothstein I. Z., 2012, Phys. Rev. Lett., 109, 029502

Gebhardt K., et al., 2000, ApJL, 539, L13

Genzel R., Hollenbach D., Townes C. H., 1994, Reports on Progress in Physics, 57, 417

Genzel R., Thatte N., Krabbe A., Kroker H., Tacconi-Garman L. E., 1996, ApJ, 472, 153

Genzel R., Pichon C., Eckart A., Gerhard O. E., Ott T., 2000, MNRAS, 317, 348

Genzel R., et al., 2003, ApJ, 594, 812

Genzel R., Eisenhauer F., Gillessen S., 2010, Reviews of Modern Physics, 82, 3121

Georgiev I. Y., Böker T., Leigh N., Lützgendorf N., Neumayer N., 2016, MNRAS, 457, 2122

Ghez A. M., et al., 2003, ApJL, 586, L127

Ghez A. M., et al., 2005, ApJ, 635, 1087

Gies D. R., Bolton C. T., 1986, ApJS, 61, 419

Gillessen S., Eisenhauer F., Trippe S., Alexander T., Genzel R., Martins F., Ott T., 2009, ApJ, 692, 1075

Gillessen S., et al., 2012, Nature, 481, 51

Gillessen S., et al., 2013a, ApJ, 763, 78

Gillessen S., et al., 2013b, ApJ, 774, 44

Gillessen S., et al., 2014, in Sjouwerman L. O., Lang C. C., Ott J., eds, IAU Symposium Vol. 303, The Galactic Center: Feeding and Feedback in a Normal Galactic Nucleus. pp 254–263, doi:10.1017/S1743921314000702

Gillessen S., et al., 2017, ApJ, 837, 30

Ginsburg I., Loeb A., 2006, MNRAS, 368, 221

Ginsburg I., Loeb A., 2007, MNRAS, 376, 492

Ginsburg I., Loeb A., Wegner G. A., 2012, MNRAS, 423, 948

Gnedin O. Y., Gould A., Miralda-Escudé J., Zentner A. R., 2005, ApJ, 634, 344

Gould A., Quillen A. C., 2003, ApJ, 592, 935

Gragg W. B., 1964, PhD thesis, -

Gragg W. B., 1965, SIAM Journal on Numerical Analysis, 2, 384

Graham A. W., 2012, Monthly Notices of the Royal Astronomical Society, 422, 1586

Gravity Collaboration et al., 2018, A&A, 615, L15

Greenstein J. L., Schmidt M., 1964, ApJ, 140, 1

Gualandris A., Portegies Zwart S., 2007, MNRAS, 376, L29

Guillochon J., Loeb A., MacLeod M., Ramirez-Ruiz E., 2014, ApJL, 786, L12

Gvaramadze V. V., Gualandris A., 2011, MNRAS, 410, 304

Gvaramadze V. V., Gualandris A., Portegies Zwart S., 2009, MNRAS, 396, 570

Haas J., Šubr L., 2016, Mem. Soc. Astron. Italiana, 87, 689

Habibi M., et al., 2017, ApJ, 847, 120

Habibi M., et al., 2019, ApJL, 872, L15

Haggard D., 2014, in 15 Years of Science with Chandra. p. 17

Hansen B. M. S., 2007, ApJL, 671, L133

Hansen B. M. S., Milosavljević M., 2003, ApJL, 593, L77

Harfst S., Gualandris A., Merritt D., Mikkola S., 2008, MNRAS, 389, 2

Häring N., Rix H.-W., 2004, ApJL, 604, L89

Hattori K., Valluri M., 2019, arXiv e-prints, p. arXiv:1909.03321

Hayden M. R., et al., 2014, AJ, 147, 116

Heggie D. C., 1974, Celestial Mechanics, 10, 217

Hellström C., Mikkola S., 2010, Celestial Mechanics and Dynamical Astronomy, 106, 143

Henon M., 1969, A&A, 2, 151

Hills J. G., 1988, Nature, 331, 687

Hirsch H. A., Heber U., O'Toole S. J., Bresolin F., 2005, A&A, 444, L61

Hobbs G., Lorimer D. R., Lyne A. G., Kramer M., 2005, MNRAS, 360, 974

Hoogerwerf R., de Bruijne J. H. J., de Zeeuw P. T., 2001, A&A, 365, 49

Humason M. L., Zwicky F., 1947, ApJ, 105, 85

Jackson J. M., Geis N., Genzel R., Harris A. I., Madden S., Poglitsch A., Stacey G. J., Townes C. H., 1993, ApJ, 402, 173

Jaranowski P., Schäfer G., 1998, Phys. Rev. D, 57, 7274

Jia S., et al., 2019, ApJ, 873, 9

Kauffmann G., et al., 2003, MNRAS, 346, 1055

Kenyon S. J., Bromley B. C., Geller M. J., Brown W. R., 2008, ApJ, 680, 312

Kenyon S. J., Bromley B. C., Brown W. R., Geller M. J., 2014, The Astrophysical Journal, 793, 122

Kerr R., 1963, Physical Review Letters - PHYS REV LETT, 11, 237

Kidder L. E., 1995, Phys. Rev. D, 52, 821

King A., Pounds K., 2015, ARA&A, 53, 115

Kobulnicky H. A., Fryer C. L., 2007, ApJ, 670, 747

Kollmeier J. A., Gould A., Knapp G., Beers T. C., 2009, ApJ, 697, 1543

Kollmeier J. A., et al., 2010, ApJ, 723, 812

Kormendy J., Bender R., 2009, ApJL, 691, L142

Kormendy J., Ho L. C., 2013, ARA&A, 51, 511

Kormendy J., Kennicutt Robert C. J., 2004, ARA&A, 42, 603

Koyama K., Maeda Y., Sonobe T., Takeshima T., Tanaka Y., Yamauchi S., 1996, PASJ, 48, 249

Kozai Y., 1962, AJ, 67, 591

Kroupa P., 1995, MNRAS, 277, 1507

Kupi G., Amaro-Seoane P., Spurzem R., 2006, Monthly Notices of the Royal Astronomical Society: Letters, 371, L45–L49

Kustaanheimo P., 1964, Spinor Regularization of the Kepler Motion. Turun Yliopisto

Kustaanheimo P., Stiefel E., 1965, J. Reine Angew. Math., 218, 204

Lacy J. H., Townes C. H., Geballe T. R., Hollenbach D. J., 1980, ApJ, 241, 132

Lacy J. H., Townes C. H., Hollenbach D. J., 1982, ApJ, 262, 120

Lauer T. R., et al., 1995, AJ, 110, 2622

Launhardt R., Zylka R., Mezger P. G., 2002, A&A, 384, 112

Leigh N., Böker T., Knigge C., 2012, MNRAS, 424, 2130

Leonard P. J. T., Duncan M. J., 1990, AJ, 99, 608

Levi-Civita T., 1920, Acta Math., 42, 99

Levin Y., 2006a, Monthly Notices of the Royal Astronomical Society, 374, 515

Levin Y., 2006b, ApJ, 653, 1203

Levin Y., Beloborodov A. M., 2003, ApJL, 590, L33

Li Y., Luo A., Zhao G., Lu Y., Ren J., Zuo F., 2012, ApJL, 744, L24

Li D., Mustill A. J., Davies M. B., 2019, Monthly Notices of the Royal Astronomical Society, 488, 1366–1376

Lidov M. L., 1962, Planet. Space Sci., 9, 719

Lin D. N. C., Tremaine S., 1980, ApJ, 242, 789

Löckmann U., Baumgardt H., 2008, MNRAS, 384, 323

Löckmann U., Baumgardt H., Kroupa P., 2009, MNRAS, 398, 429

López-Morales M., Bonanos A. Z., 2008, ApJL, 685, L47

Lu Y., Yu Q., Lin D. N. C., 2007, ApJL, 666, L89

Lu J. R., Ghez A. M., Hornstein S. D., Morris M. R., Becklin E. E., Matthews K., 2009, ApJ, 690, 1463

Lu J. R., Do T., Ghez A. M., Morris M. R., Yelda S., Matthews K., 2013, ApJ, 764, 155

Lynden-Bell D., 1969, Nature, 223, 690

Lynden-Bell D., Rees M. J., 1971, MNRAS, 152, 461

Lyne A. G., Lorimer D. R., 1994, Nature, 369, 127

Madigan A.-M., Levin Y., Hopman C., 2009, ApJL, 697, L44

Magorrian J., et al., 1998, AJ, 115, 2285

Mapelli M., Gualandris A., 2016, in Haardt F., Gorini V., Moschella U., Treves A., Colpi M., eds, Lecture Notes in Physics, Berlin Springer Verlag Vol. 905, Lecture Notes in Physics, Berlin Springer Verlag. p. 205 (`arXiv:1505.05473`), doi:10.1007/978-3-319-19416-5˙6

Mapelli M., Ripamonti E., 2015, ApJ, 806, 197

Marchetti T., Rossi E. M., Brown A. G. A., 2019, MNRAS, 490, 157

Marrone D. P., Moran J. M., Zhao J.-H., Rao R., 2006, The Astrophysical Journal, 640, 308

Martins F., et al., 2006, ApJL, 649, L103

McConnachie A. W., 2012, AJ, 144, 4

McGinn M. T., Sellgren K., Becklin E. E., Hall D. N. B., 1989, ApJ, 338, 824

Merritt D., 2013

Merritt D., Gualandris A., Mikkola S., 2009, ApJL, 693, L35

Merritt D., Alexander T., Mikkola S., Will C. M., 2010, Physical Review D, 81

Mikkola S., 2008a, in Vesperini E., Giersz M., Sills A., eds, IAU Symposium Vol. 246, Dynamical Evolution of Dense Stellar Systems. pp 218–227, doi:10.1017/S1743921308015639

Mikkola S., 2008b, Regular Algorithms for the Few-Body Problem. p. 31, doi:10.1007/978-1-4020-8431-7˙2

Mikkola S., Aarseth S. J., 1989, Celestial Mechanics and Dynamical Astronomy, 47, 375

Mikkola S., Aarseth S. J., 1990, Celestial Mechanics and Dynamical Astronomy, 47, 375

Mikkola S., Aarseth S. J., 1993, Celestial Mechanics and Dynamical Astronomy, 57, 439

Mikkola S., Aarseth S., 2002, Celestial Mechanics and Dynamical Astronomy, 84, 343

Mikkola S., Merritt D., 2006, MNRAS, 372, 219

Mikkola S., Merritt D., 2008a, AJ, 135, 2398

Mikkola S., Merritt D., 2008b, AJ, 135, 2398

Mikkola S., Tanikawa K., 1999a, Celestial Mechanics and Dynamical Astronomy, 74, 287

Mikkola S., Tanikawa K., 1999b, MNRAS, 310, 745

Mikkola S., Tanikawa K., 1999c, MNRAS, 310, 745

Milosavljevic M., Merritt D., 2001, in APS April Meeting Abstracts. p. B14.003

Milosavljević M., Merritt D., 2003, ApJ, 596, 860

Milosavljević M., Merritt D., Rest A., van den Bosch F. C., 2002, MNRAS, 331, L51

Miralda-Escudé J., Gould A., 2000, ApJ, 545, 847

Miyazaki A., Tsutsumi T., Tsuboi M., 2004, ApJL, 611, L97

Montero-Castaño M., Herrnstein R. M., Ho P. T. P., 2009, The Astrophysical Journal, 695, 1477

Mora T., Will C. M., 2004, Phys. Rev. D, 69, 104021

Morris M., 1993, ApJ, 408, 496

Mortlock D. J., et al., 2011, Nature, 474, 616

Munn J. A., et al., 2004, AJ, 127, 3034

Muno M. P., Baganoff F. K., Brandt W. N., Park S., Morris M. R., 2007, ApJL, 656, L69

Murray-Clay R. A., Loeb A., 2012, Nature Communications, 3, 1049

Nayakshin S., 2005, Monthly Notices of the Royal Astronomical Society, 359, 545

Nayakshin S., Dehnen W., Cuadra J., Genzel R., 2006, Monthly Notices of the Royal Astronomical Society, 366, 1410

Nayakshin S., Wilkinson M. I., King A., 2009, MNRAS, 398, L54

Nayakshin S., Power C., King A. R., 2012, ApJ, 753, 15

Németh P., Ziegerer E., Irrgang A., Geier S., Fürst F., Kupfer T., Heber U., 2016, ApJL, 821, L13

Neumayer N., 2012, arXiv e-prints, p. arXiv:1211.1795

Neumayer N., Walcher C. J., Andersen D., Sánchez S. F., Böker T., Rix H.-W., 2011, MNRAS, 413, 1875

Nieva M. F., Przybilla N., 2012, A&A, 539, A143

O'Leary R. M., Loeb A., 2008, MNRAS, 383, 86

Ott T., Eckart A., Genzel R., 1999, ApJ, 523, 248

Pati M. E., Will C. M., 2002, Phys. Rev. D, 65, 104008

Paumard T., et al., 2006, ApJ, 643, 1011

Pavan L., et al., 2014, A&A, 562, A122

Perets H. B., 2009a, ApJ, 690, 795

Perets H. B., 2009b, ApJ, 690, 795

Perets H. B., Šubr L., 2012, ApJ, 751, 133

Perets H. B., Hopman C., Alexander T., 2007, ApJ, 656, 709

Perets H. B., Gualandris A., Kupi G., Merritt D., Alexander T., 2009, ApJ, 702, 884

Pesce E., Capuzzo-Dolcetta R., Vietri M., 1992, MNRAS, 254, 466

Pfuhl O., et al., 2011, ApJ, 741, 108

Pfuhl O., Alexander T., Gillessen S., Martins F., Genzel R., Eisenhauer F., Fritz T. K., Ott T., 2014, ApJ, 782, 101

Pfuhl O., et al., 2015, ApJ, 798, 111

Phifer K., et al., 2013, ApJL, 773, L13

Plewa P. M., et al., 2017, ApJ, 840, 50

Plummer H. C., 1911, MNRAS, 71, 460

Ponti G., Terrier R., Goldwurm A., Belanger G., Trap G., 2010, ApJ, 714, 732

Portegies Zwart S. F., 2000, ApJ, 544, 437

Poveda A., Ruiz J., Allen C., 1967, Boletin de los Observatorios Tonantzintla y Tacubaya, 4, 86

Preto M., Tremaine S., 1999, AJ, 118, 2532

Przybilla N., Nieva M. F., Heber U., Firnstein M., Butler K., Napiwotzki R., Edelmann H., 2008a, A&A, 480, L37

Przybilla N., Nieva M. F., Tillich A., Heber U., Butler K., Brown W. R., 2008b, A&A, 488, L51

Quinlan G. D., Hernquist L., 1997, New A, 2, 533

Rafelski M., Ghez A. M., Hornstein S. D., Lu J. R., Morris M., 2007, ApJ, 659, 1241

Ramírez S. V., Sellgren K., Carr J. S., Balachandran S. C., Blum R., Terndrup D. M., Steed A., 2000, ApJ, 537, 205

Rasskazov A., Fragione G., Leigh N. W. C., Tagawa H., Sesana A., Price-Whelan A., Rossi E. M., 2019, ApJ, 878, 17

Rea N., et al., 2013, ApJL, 775, L34

Read J. I., Goerdt T., Moore B., Pontzen A. P., Stadel J., Lake G., 2006, Monthly Notices of the Royal Astronomical Society, 373, 1451–1460

Rees M. J., 1984, ARA&A, 22, 471

Reynolds C. S., 2014, Space Sci. Rev., 183, 277

Rieke G. H., Rieke M. J., 1989, ApJL, 344, L5

Rossa J., van der Marel R. P., Böker T., Gerssen J., Ho L. C., Rix H.-W., Shields J. C., Walcher C.-J., 2006, AJ, 132, 1074

Salpeter E. E., 1964, ApJ, 140, 796

Sandage A. R., 1953, AJ, 58, 61

Sanders R. H., Lowinger T., 1972, AJ, 77, 292

Schmidt M., 1963, Nature, 197, 1040

Schödel R., 2011, in Morris M. R., Wang Q. D., Yuan F., eds, Astronomical Society of the Pacific Conference Series Vol. 439, The Galactic Center: a Window to the Nuclear Environment of Disk Galaxies. p. 222 (`arXiv:1001.4238`)

Schödel R., et al., 2002, Nature, 419, 694

Schödel R., Ott T., Genzel R., Eckart A., Mouawad N., Alexander T., 2003, ApJ, 596, 1015

Schödel R., et al., 2007, A&A, 469, 125

Schödel R., Merritt D., Eckart A., 2009, A&A, 502, 91

Schödel R., Najarro F., Muzic K., Eckart A., 2010, A&A, 511, A18

Schödel R., Feldmeier A., Kunneriath D., Stolovy S., Neumayer N., Amaro-Seoane P., Nishiyama S., 2014, A&A, 566, A47

Schödel R., Gallego Cano E., Nogueras Lara F., Dong H., Gallego Calvente T., 2017, in Arribas S., Alonso-Herrero A., Figueras F., Hernández-Monteagudo C., Sánchez-Lavega A., Pérez-Hoyos S., eds, Highlights on Spanish Astrophysics IX. pp 308–315 (`arXiv:1702.00219`)

Schödel R., Gallego-Cano E., Dong H., Nogueras-Lara F., Gallego-Calvente A. T., Amaro-Seoane P., Baumgardt H., 2018, A&A, 609, A27

Scott N., Graham A. W., 2013, ApJ, 763, 76

Scoville N., Burkert A., 2013, ApJ, 768, 108

Sellgren K., McGinn M. T., Becklin E. E., Hall D. N., 1990, ApJ, 359, 112

Sesana A., Haardt F., Madau P., 2006, The Astrophysical Journal, 651, 392–400

Sesana A., Haardt F., Madau P., 2007, MNRAS, 379, L45

Sesana A., Haardt F., Madau P., 2008, ApJ, 686, 432

Seth A., Blum R., Olsen K., Stephens A., Jensen J., Davidge T., Neumayer N., 2008, Surveying Nearby Nuclear Star Clusters, NOAO Proposal

Soffel M. H., 1989, Relativity in Astrometry, Celestial Mechanics and Geodesy

Spurzem R., Giersz M., Heggie D. C., Lin D. N. C., 2009, The Astrophysical Journal, 697, 458–482

Stiefel E. L., Scheifele G., 1971, JRASC, 65, 304

Sundman K., 1907, Recherches sur le problème des trois corps. Acta societatis scientiarum Fennicae. 34,6, Ex Officina Typographica Societatis Litterariae Fennicae

Sunyaev R. A., Markevitch M., Pavlinsky M., 1993, ApJ, 407, 606

Tanner A., et al., 2006, The Astrophysical Journal, 641, 891

Tauris T. M., 2015, MNRAS, 448, L6

Tauris T. M., Takens R. J., 1998, A&A, 330, 1047

Tokovinin A., 2014, AJ, 147, 87

Tomsick J. A., Bodaghee A., Rodriguez J., Chaty S., Camilo F., Fornasini F., Rahoui F., 2012, ApJL, 750, L39

Trani A. A., Mapelli M., Spera M., Bressan A., 2016, ApJ, 831, 61

Trani A. A., Fujii M. S., Spera M., 2019, ApJ, 875, 42

Tremaine S. D., Ostriker J. P., Spitzer L. J., 1975, ApJ, 196, 407

Tremaine S., et al., 2002, ApJ, 574, 740

Trippe S., et al., 2008, A&A, 492, 419

Waldvogel J., 2008, Celestial Mechanics and Dynamical Astronomy, 102, 149

Webb J. J., Leigh N. W. C., Serrano R., Bellovary J., Ford K. E. S., McKernan B., Spera M., Trani A. A., 2019, Monthly Notices of the Royal Astronomical Society, 488, 3055–3066

Wehner E. H., Harris W. E., 2006, ApJL, 644, L17

Wilkinson M. I., Evans N. W., 1999, MNRAS, 310, 645

Witzel G., et al., 2014, ApJL, 796, L8

Wollman E. R., Geballe T. R., Lacy J. H., Townes C. H., Rank D. M., 1977, ApJL, 218, L103

Yelda S., Ghez A. M., Lu J. R., Do T., Meyer L., Morris M. R., 2012, in Proc. SPIE. p. 84470A (`arXiv:1208.3466`), doi:10.1117/12.927217

Yelda S., Ghez A. M., Lu J. R., Do T., Meyer L., Morris M. R., Matthews K., 2014, ApJ, 783, 131

Yu Q., 2002, MNRAS, 331, 935

Yu Q., Madau P., 2007, MNRAS, 379, 1293

Yu Q., Tremaine S., 2003, ApJ, 599, 1129

Yu Y.-W., Cheng K. S., Chernyshov D. O., Dogiel V. A., 2011, MNRAS, 411, 2002

Yusef-Zadeh F., et al., 2006, The Astrophysical Journal, 644, 198

Yusef-Zadeh F., Roberts D. A., Wardle M., Cotton W., Schödel R., Royster M. J., 2015a, ApJL, 801, L26

Yusef-Zadeh F., et al., 2015b, ApJ, 808, 97

Yusef-Zadeh F., et al., 2017, MNRAS, 470, 4209

Zare K., 1974, Celestial Mechanics, 10, 207

Zhang F., Lu Y., Yu Q., 2010, ApJ, 722, 1744

Zubovas K., Wynn G. A., Gualandris A., 2013, ApJ, 771, 118